MICROCOPY RESOLUTION TEST CHART

NATIONAL BUREAU OF STANDARDS-1963-A

Space Shuttle Windward Streamline Laminar Viscous Shock-Layer Flows At Angle Of Attack— Comparison Of Theory And Experiment

Alvin L. Murray, John D. Waskiewicz and Clark H. Lewis
Aerospace and Ocean Engineering Department

D D C

AUG 11 1977

C

College of Engineering,
Virginia Polytechnic Institute
and State University
Blacksburg, Virginia

⑥ SPACE SHUTTLE WINDWARD

STREAMLINE LAMINAR VISCOUS SHOCK-LAYER FLOWS

AT ANGLE OF ATTACK--COMPARISON OF THEORY AND EXPERIMENT

by

⑩ Alvin L. Murray, John D. Waskiewicz and Clark H. Lewis

⑭ VPI-AERO-044

Aerospace and Ocean Engineering Department

Virginia Polytechnic Institute and State University

Blacksburg, Virginia 24061

⑫ 93p.

⑪ May 1976

406 922

ABSTRACT

Comparisons have been made between a perfect gas laminar viscous shock layer method and experimental data from the AEDC/vKF Hypersonic Tunnels. The test model was the Rockwell International 139 Shuttle Orbiter, and the data taken included wall pressure distributions, heat-transfer distributions, stagnation temperature and pitot pressure profiles through the shock layer. Comparisons were made at Mach numbers of 8, 11 and 14, with Reynolds numbers ranging from 0.52 x 10⁶ to 1.0 x 10⁷ per foot and angles of attack from 0 to 45 degrees. Comparisons showed good to excellent agreement except at very low angles of attack where the axisymmetric solution did not model well the flat bottom of the orbiter.

iii

TABLE OF CONTENTS

LIST OF FIGURES

NOMENCLATURE

A_n coefficients of a partial differential equation

C_f skin-friction coefficient

C_p specific heat at constant pressure

FVSL   denotes fully viscous shock layer

H heat-transfer coefficient, $q_w/(T_0 - T_w)$

$\overline{H}$ stagnation enthalpy

H_{ref} reference heat-transfer coefficient

j $j = 0$ for two-dimensional flow
           $j = 1$ for axisymmetric flow

k thermal conductivity

L length of body

M Mach number

$\overline{M}$ molecular weight of mixture of gases

P pressure

Pr Prandtl number, $C_p \mu/k$

q heat transfer

R universal gas constant

Re Reynolds number

r body radius

St Stanton number, $q/\rho_\infty U_\infty (\overline{H}_0 - \overline{H}_w)$

s coordinate measured along body surface

T temperature

TVSL   denotes thin viscous shock layer

U, u tangential component of velocity

v normal component of velocity

W	dependent variable
x	coordinate measured along body axis
y	coordinate measured normal to body
α	angle of attack
β	$\pi/2 - \phi$
γ	ratio of specific heats
ϵ	Reynolds number parameter, $(\mu_{ref}/\rho_\infty U_\infty R_n)^{1/2}$
κ	surface curvature
μ	coefficient of viscosity
ρ	density
ϕ	angle between body tangent and axis

Subscripts

sh	value behind the shock
w	wall value
∞	freestream value
0	stagnation point value
1	conditions before the shock
2	conditions after the shock

I. INTRODUCTION

One of the most critical parts of any space mission involving a return to
earth is the reentry into the earth's atmosphere. Development of reusable
spacecraft, such as the shuttle, requires even more knowledge of this important
phase of space flight. Reentry conditions include laminar hypersonic flows
which may be simulated by various types of models. In the approach most com-
monly used, the flowfield is divided into two parts, an inviscid outer region
and a viscous boundary-layer region. Many methods are available for solving
both flow regions. Examples of inviscid techniques are the methods of Inouye,
Rakich and Lomax (Ref. 1), Rizzi and Inouye (Ref. 2) and Kutler, Reinhardt and
Warming (Ref. 3). For viscous boundary-layer solutions, methods such as that
of Blottner (Ref. 4) may be used. This approach is most appropriate for super-
sonic, high Reynolds number conditions and encounters some problems when applied
to low Reynolds number flows. These problems include displacement-thickness in-
teraction and specification of the boundary-layer edge conditions. Problems
such as the displacement-thickness interaction may be approximately treated by
using second-order boundary-layer theory such as the work of Lewis (Ref. 5).
Specification of the boundary-layer edge conditions is more difficult. For
supersonic, high Reynolds number flows the boundary layer is thin compared to
the shock-layer thickness, and the boundary-layer edge conditions are considered
to be the same as the surface conditions of the inviscid solution. For hyper-
sonic, low Reynolds number flows, the boundary layer is not thin and the edge
conditions must be determined by another method such as streamline tracking or
entropy-layer swallowing.

Another approach to solving hypersonic blunt body flows has been the use of the full Navier-Stokes equations. The elliptic nature of these equations increases the complexity of the solution procedures and restricts their application in the downstream direction. Most of the current methods have been used to solve the stagnation region and have only been applied downstream a distance of about one nose radius.

A third approach to the reentry problem is viscous shock-layer flow in which the entire flowfield from the body to the shock is treated in a uniform manner. Use of a viscous shock-layer approach avoids problems such as streamline tracking and displacement-thickness interaction. The equations are parabolic in the streamwise direction so there are no restrictions on obtaining solutions in the downstream direction, and at high Reynolds numbers the equations tend to the first-order boundary-layer equations.

The purpose of this work has been to validate a viscous shock-layer method developed by Miner and Lewis (Ref. 6) by comparing solutions using that method with experimental data. Miner and Lewis followed the formulation of Davis (Refs. 7 and 8) and Moss (Ref. 9) to develop a system of governing equations for viscous shock-layer flows of reacting gases. A similar code was developed which used a perfect gas model and eliminated the complicated chemical reactions and species conservation equation. The perfect gas model was used in the present work because it required much less computing time than did the reacting-gas code and modeled well the wind-tunnel conditions. A large set of experimental data was made available by the Arnold Engineering Development Center (AEDC) where tests had been conducted on models of the shuttle orbiter (Refs. 10-13). These tests were conducted in two of the tunnels at the von Karman Gas Dynamics Facility (vKF) which could simulate conditions similar to those encountered during reentry.

Tunnel B is a continuous, closed-circuit, variable density tunnel which can be operated at stagnation pressures from 20 to 300 psia for a nominal Mach number of 6 and from 50 to 900 psia for Mach 8. The Reynolds number range was 0.52×10^6 to 3.8×10^6 per foot. The model was injected into the tunnel for tests and then retracted for cooling or changes. Data measured in Tunnel B at M = 7.9 included wall pressure distributions, pitot pressure and temperature profiles (Ref. 10) and heat-transfer distributions (Ref. 11) at angles of attack from 0 to 45 degrees. The second tunnel used was the vKF Hypervelocity Wind Tunnel (F) which is an arc-driven hotshot wind tunnel. This tunnel is capable of Mach numbers from 7.5 to 20 and Reynolds numbers per foot from 0.75×10^6 to 1.0×10^7. The tests were conducted using the nozzle for $M_\infty = 10.1$ to 16.2 and nitrogen as the test gas. Useful test times for Tunnel F were approximately 100 msec. Data taken in this tunnel were heat-transfer distributions along the body of the model at various angles of attack (Ref. 12). Calculations were made using the perfect gas method, and the computed results were compared with experimental data from these two tunnels.

II. ANALYSIS

In the present work, the governing equations for the viscous shock-layer flows follow the formulation of Davis (Refs. 7 and 8). The equations were first nondimensionalized by variables of order one at the body surface (corresponding to high Reynolds number, boundary-layer flows). The equations were also non-dimensionalized by variables of order one in the outer inviscid flow (corres-ponding to the shock region). A single set of equations was then obtained by retaining terms from the equations in each set to second order. The resulting set of shock-layer equations was uniformly second-order accurate in the inverse Reynolds number parameter ε from the body to the shock. Both longitudinal and transverse curvature were included. As given by Davis, the governing vis-cous shock-layer equations were specialized for a perfect gas (Ref. 7) or a binary, reacting mixture of oxygen atoms and molecules (Ref. 8). Miner and Lewis (Ref. 6) gave the shock-layer equations for a multicomponent mixture of reacting gas.

Governing Equations

The equations for shock-layer flows of perfect gases are given below.

Continuity Equation:

$$\frac{\partial}{\partial s}\left[(r + y\cos\phi)^j \rho u\right] + \frac{\partial}{\partial y}\left[(1 + \kappa y)(r + y\cos\phi)^j \rho v\right] = 0 \qquad (1)$$

s-Momentum Equation:

$$\frac{1}{1+\kappa y}\rho u\frac{\partial u}{\partial s} + \rho v\frac{\partial u}{\partial y} + \rho uv\frac{\kappa}{1+\kappa y} + \frac{1}{1+\kappa y}\frac{\partial P}{\partial s} = \varepsilon^2\frac{\partial}{\partial y}\left[\mu\left(\frac{\partial u}{\partial y} - \frac{\kappa u}{1+\kappa y}\right)\right]$$

$$+ \varepsilon^2\mu\left(\frac{2\kappa}{1+\kappa y} + \frac{j\cos\phi}{r + y\cos\phi}\right)\left(\frac{\partial u}{\partial y} - \frac{\kappa u}{1+\kappa y}\right) \qquad (2)$$

-4-

y-Momentum Equation:

$$\frac{\partial P}{\partial y} = \frac{\kappa}{1+\kappa y} \rho u^2 - \frac{1}{1+\kappa y} \rho u \frac{\partial v}{\partial s} - \rho v \frac{\partial v}{\partial y} \quad \text{(FVSL)} \tag{3a}$$

which becomes

$$\frac{\partial P}{\partial y} = \frac{\kappa}{1+\kappa y} \rho u^2 \quad \text{(TVSL)} \tag{3b}$$

if the thin shock-layer approximation is made.

Energy Equation:

$$\frac{1}{1+\kappa y} \rho u \, C_p \frac{\partial T}{\partial s} + \rho v \, C_p \frac{\partial T}{\partial y} - \frac{1}{1+\kappa y} u \frac{\partial P}{\partial s} - v \frac{\partial P}{\partial y} = \varepsilon^2 \frac{\partial}{\partial y} \left(k \frac{\partial T}{\partial y} \right)$$

$$+ \, \varepsilon^2 \left(\frac{\kappa}{1+\kappa y} + \frac{j \cos \phi}{r + y \cos \phi} \right) \, k \frac{\partial T}{\partial y} + \varepsilon^2 \mu \left(\frac{\partial u}{\partial y} - \frac{\kappa u}{1+\kappa y} \right)^2 \tag{4}$$

Equation of State:

$$P = \frac{\rho \, RT}{\bar{M} \, C_{p_\infty}{}^*} \tag{5}$$

These equations are in nondimensional variables which are defined by the following relations:

$$u = u^*/U_\infty^*$$

$$v = v^*/U_\infty^*$$

$$T = T^* C_{p_\infty}{}^*/U_\infty^{*2}$$

$$P = P^*/\rho_\infty^* \, U_\infty^*$$

$$\rho = \rho^*/\rho_\infty^*$$

-5-

$$\mu = \mu^*/\mu^*_{ref}$$

$$k = k^*/\mu^*_{ref} C_{p_\infty}^*$$

$$C_p = C_p^*/C_{p_\infty}^*$$

$$s = s^*/r_n^*$$

$$y = y^*/r_n^*$$

$$\kappa = \kappa^* r_n^*$$

$$r = r^*/r_n^*$$

and

$$\varepsilon = (\mu^*_{ref}/\rho^*_\infty U^*_\infty r_n^*)^{1/2}$$

For the finite-difference solution procedure, it was helpful to transform the shock-layer equations. The variables were normalized by the local shock values as follows:

$$n = y/y_{sh}$$

$$\xi = s$$

$$\bar{u} = u/u_{sh}$$

$$\bar{v} = v/v_{sh}$$

$$\bar{P} = P/P_{sh}$$

$$\bar{\rho} = \rho/\rho_{sh}$$

$$\bar{T} = T/T_{sh}$$

$$\bar{\mu} = \mu/\mu_{sh}$$

$$\bar{k} = k/k_{sh}$$

and

$$\bar{C}_p = C_p/C_{p_{sh}}$$

When written in the transformed ξ, η coordinates, the s-momentum and energy equations could be expressed in the standard form for a parabolic partial differential equation.

$$\frac{\partial^2 W}{\partial \eta^2} + A_1 \frac{\partial W}{\partial \eta} + A_2 W + A_3 + A_4 \frac{\partial W}{\partial \xi} = 0 \tag{6}$$

where W represents the dependent variable. The coefficients A_i were functions of the independent and dependent variables and are given in Ref. 6 for reacting gas mixtures and in Ref. 7 for perfect gases.

Boundary Conditions

At the body surface, the no-slip boundary conditions were imposed, thus for $\eta = 0$

$$\bar{u} = 0$$
$$\bar{v} = 0$$

and

$$\bar{T} = T_w \tag{7}$$

where T_w was either a specified constant or distribution.

-7-

At the shock, the velocity components tangent and normal to the shock are not the same as the components tangent and normal to the body. The transformations relating the shock components with the body components were

$$u_{sh} = \hat{u}_{sh} \sin(\alpha + \beta) + \hat{v}_{sh} \cos(\alpha + \beta) \tag{8}$$

and

$$v_{sh} = -\hat{u}_{sh} \cos(\alpha + \beta) + \hat{v}_{sh} \sin(\alpha + \beta) \tag{9}$$

where $\hat{u}_{sh}$ and $\hat{v}_{sh}$ are the shock oriented components and $\beta = \pi/2 - \phi$. The boundary conditions at the shock were determined by the modified Rankine-Hugoniot relations.

$$\hat{u}_{sh} = \sin \alpha \; \cos \alpha \left/ \left[\sin \alpha + \epsilon^2 \mu_{sh} (\partial \hat{\bar{u}}/\partial n)_{sh} \right] \right. \tag{10}$$

$$T_{sh} = \left\{ (\hat{u}_{sh} - \cos \alpha)^2 + 4\gamma \sin^2\alpha/(\gamma+1)^2 + \left[2/\gamma-1 - 4(\gamma-1)/(\gamma+1)^2 \right] \right/$$

$$M_\infty^2 - 4/(\gamma+1)^2 \, M_\infty^4 \sin^2\alpha \right\} \; \sin \alpha / 2 \left[\epsilon^2 \mu_{sh}(\partial \bar{T}/\partial n)_{sh}/Pr + \sin \alpha \right] \tag{11}$$

$$P_{sh} = \left[2 \sin^2\alpha - (\gamma-1)/\gamma M_\infty^2 \right] /(\gamma+1) \tag{12}$$

$$\rho_{sh} = \gamma P_{sh}/(\gamma-1) \, T_{sh} \tag{13}$$

$$\hat{v}_{sh} = -\sin \alpha/\rho_{sh} \tag{14}$$

The shock boundary conditions for the normalized dependent variables at $\eta = 1$ were $\bar{u} = \bar{v} = \bar{\rho} = \bar{p} = \bar{T} = 1$.

Perfect Gas Property Model

The thermodynamic and transport properties for the perfect gas were calculated using standard relations. The temperature was computed by the energy conservation equation. The density was then calculated from the equation of state and the viscosity from

$$\mu = (1 + C') (T)^{1.5}/(T + C') \tag{15}$$

where

$$C' = 198.6 \,^{\circ}R/(\gamma - 1) \, M_\infty^2 \, T_\infty$$

The transport properties were specified by setting the Prandtl number and Lewis number to 0.7 and 1.0, respectively.

Surface Conditions

The surface skin-friction and heat-transfer rates were given by the skin-friction coefficient and Stanton number. The skin-friction coefficient in the nondimensional variables was defined as:

$$C_f = 2\epsilon^2 \left[\mu \, \partial u/\partial y \right]_w \tag{16}$$

The Stanton number in the nondimensional variables was

$$St = q_w/(\overline{H}_0 - \overline{H}_w) \tag{17}$$

where

$$q_w = -\epsilon^2 \left[k \, \partial T/\partial y \right]_w$$

Method of Solution

The s-momentum and energy equations were expressed in the standard form for a parabolic partial differential equation.

$$\frac{\partial^2 W}{\partial \eta^2} + A_1 \frac{\partial W}{\partial \eta} + A_2 W + A_3 + A_4 \frac{\partial W}{\partial \xi} = 0 \qquad (18)$$

These equations were solved using the algorithm described by Davis (Ref. 7) and Miner and Lewis (Ref. 6). The algorithm assumes

$$W^n = E_n W^{n+1} + F_n \qquad (19)$$

is valid through the shock layer where

$$E_n = \frac{-C_n}{B_n + A_n E_{n-1}}$$

and

$$F_n = \frac{D_n - A_n F_{n-1}}{B_n + A_n E_{n-1}}$$

where A_n, B_n, C_n and D_n are as defined in Ref. 6.

The boundary conditions at the wall were specified by defining F_1 and E_1 such as

$$F_1 = W_w \text{ and } E_1 = 0 \text{ if } W_1 = W_w$$

or

$$F_1 = 0 \text{ and } E_1 = 1 \text{ if } \left(\frac{\partial W}{\partial \eta}\right)_1 = 0$$

At the shock, the value of W is set equal to the shock value. Thus the solution of the differential equation is obtained by evaluating E_n and F_n from $\eta = 0$ to $\eta = \eta_{sh}$ as in Ref. 6, and then using Eq. 19 to evaluate the dependent variable with η decreasing from η_{sh} to 0.

Solutions for the continuity and η-momentum equations were obtained by integration with the trapezoidal rule. The normal momentum equation is rewritten in the transformed coordinates so that $\partial \overline{P}/\partial \eta$ may be evaluated directly

-10-

as

$$\frac{\partial \bar{p}}{\partial \eta} = \frac{k \, y_{sh} \, \rho_{sh} \, u_{sh}^2}{p_{sh} \, (1 + k \, y_{sh} \, \eta)} \; \bar{\rho} \, \bar{u}^2 - \frac{\rho_{sh} \, v_{sh}^2}{p_{sh}} \; \bar{\rho} \, \bar{v} \, \frac{\partial \bar{v}}{\partial \eta}$$

$$- \frac{y_{sh} \, \rho_{sh} \, u_{sh} \, v_{sh}}{p_{sh} \, (1 + k \, y_{sh} \, \eta)} \; \bar{\rho} \, \bar{u} \left(\frac{\partial \bar{v}}{\partial \xi} + \frac{\bar{v}}{v_{sh}} \frac{\partial v_{sh}}{\partial \xi} - \frac{y_{sh}'}{y_{sh}} \, \eta \, \frac{\partial \bar{v}}{\partial \eta} \right)$$

(20)

The pressure derivative with respect to η is calculated and then integrated to provide the solution of the normal momentum equation. The continuity equation was integrated as in Ref. 6 to yield the normal velocity profile and the shock-layer thickness.

Solution Procedure

At each s location the shock-layer equations were solved in the following order: energy, s-momentum, continuity and n-momentum. The solution was iterated until the temperature and tangential velocity converged at each point in the finite-difference grid. After a converged solution was reached, the profiles were used as initial profiles for the next s location.

Since the equations depend upon $dy_{sh}/d\xi$ and $\partial \bar{v}/\partial \xi$, they possess an elliptic nature and require global iterations to obtain an accurate solution. The elliptic effect in the n-momentum equation is resolved by considering TVSL flows for the first global iteration and using the calculated $\bar{v}$ profiles for subsequent FVSL iterations. The elliptic effect due to $dy_{sh}/d\xi$ is resolved by making a suitable approximation for $dy_{sh}/d\xi$ for the first iteration. If the geometry was such that Newtonian flow was appropriate, the first iteration assumed $dy_{sh}/d\xi = 0$ and used the calculated distribution in the following

-11-

iterations. If the hypersonic flow was non-Newtonian, an initial shock shape was determined from a blunt body, method of characteristics procedure such as that of Inouye, Rakich and Lomax (Ref. 1), and the calculated $dy_{sh}/d\xi$ distribution was used in subsequent global iterations.

III. RESULTS AND DISCUSSION

Solutions from the perfect gas, viscous shock-layer program described
briefly in the preceding section were compared with experimental data from the
AEDC tests. Tables I-IV list the conditions for each of the experimental tests
used for comparison with this numerical method. The data consist of heat-
transfer distributions, wall pressure distributions and flowfield surveys.
Adams et al. (Ref. 13) describe the shuttle orbiter windward streamline at
30-deg angle of attack as a 31-deg hyperboloid. Figure 1 compares the actual
shuttle orbiter geometry at α = 30-deg with the 31-deg hyperboloid geometry.
The analytical approximation models the geometry very well to a distance of
x/L = 0.8 where the orbiter begins to curve upward. Since this 31-deg hyper-
boloid was the only geometry available, it was used as the input geometry for
the shock-layer program. Beyond x/L = 0.8, the geometries were not similar;
therefore, comparisons were not made with experimental data in this region.
To calculate the geometry of the shuttle at different angles of attack, the
31-deg hyperboloid was rotated about the center of a unit sphere located at the
nose. A fifth-deg polynomial curve-fit was used to insure the proper bluntness
and curvature of the nose of the rotated body.

The first data used for comparison was the Tunnel B body pressure distri-
butions as given by Carter and Martindale (Ref. 10). Figure 2 shows the pres-
sure distributions at various angles of attack and a unit Reynolds number of
2.3 x 10^4/cm. The agreement between the numerical prediction and the experi-
mental data was excellent. At the lower angles of attack, especially α = 15-deg,
there was an overexpansion around the nose of the shuttle and subsequent re-
compression on the body. This could not be modeled with the assumption of a

-13-

Newtonian pressure distribution, thus the numerical procedure predicted an expansion around the nose and a constant pressure along the body. Figure 3 shows the pressure distribution for α = 30-deg but at a higher unit Reynolds number of 3.6 x 10^4/cm. Again the agreement with experimental data was excellent.

Comparisons with the total temperature profile data of Martindale (Ref. 10) are shown in Figs. 4-8. These profiles were taken at angles of attack ranging from 15- to 35-deg and a nominal unit Reynolds number of 2 x 10^4/cm. In the experiment, the temperature probe began its survey at some distance away from the body and traversed the shock layer by moving inward. During the run, the orbiter model was heated considerably, especially near the nose, so when the probe neared the body, the constant wall temperature assumption was no longer valid. Since only three wall temperature measurements were taken along the body, it was difficult to determine the proper wall temperature to be used in these temperature profile comparisons. With this consideration the calculated temperature profiles are in reasonable agreement with the experimental data. Figures 4-8 consist of two parts and show the development of the profiles from x/L = 0.1 to x/L = 0.8. Figure 4 presents the profiles at α = 15-deg and shows a remarkable difference between the experimental profiles at x/L = 0.7 and at x/L = 0.8. The numerical predictions did not show this large difference. This may be due to an experimental problem or the effects of the orbiter curvature which begins around x/L = 0.8. A higher unit Reynolds number solution is shown in Fig. 7 with α = 30-deg and unit Re = 3.7 x 10^4/cm. The agreement for these cases was as good as those at the lower Reynolds numbers.

Calculations were made for comparison with the pitot pressure profiles of Ref. 10. Figures 9-13 show the pressure profiles for the same cases that

were used with the temperature profile comparisons. Figure 9 presents the profiles at α = 15-deg for x/L from 0.1 to 0.8. The prediction of the shock location was considerably low, and the higher pressures were predicted in the range of x/L = 0.3 to x/L = 0.7. This may be caused by the Newtonian pressure distribution used in the first iteration. At low angles of attack the flow is non-Newtonian and an overexpansion and recompression occur as seen in the body pressure distribution.

Another cause of the poor agreement at the low angles of attack is at these conditions the axisymmetric hyperboloid does not model the shuttle orbiter geometry very well. Figure 14 compares two cross-sections of the orbiter with the present model at various angles of attack. Figure 14 shows the orbiter at 30-deg and 0-deg angles of attack. At 30-deg the axisymmetric hyperboloid is a good model of the orbiter's flat bottom. At 0-deg the radius is much smaller and does not model the flat bottom well. Figures 15 and 16 show similar schematics at α = 15-, 25- and 45-deg. The profiles at α = 25-deg shown in Fig. 10 are in much better agreement with the experimental data than were the profiles at α = 15-deg. At the higher angles of attack, the numerical procedure begins to overpredict the shock location downstream of the blunt nose. This may be due to crossflow terms which have not been considered in this analysis. Crossflow would cause a thinner shock layer and thus a lower experimental shock location than that predicted by the present viscous shock-layer model.

A number of calculations were done using a two-dimensional model to see if the two-dimensional solution would give a better prediction of the shock location at low angles of attack. Flowfield profiles were taken from the shock-layer solutions and compared with inviscid solutions using the method of Black and Lewis (Ref. 14) and with available experimental data. The profiles

-15-

calculated were pitot pressure, total temperature, static temperature, tangential velocity, density, static pressure and Mach number. Figures 17-30 show the results of both axisymmetric and two-dimensional solutions at α = 15-deg. The agreement between the viscous and inviscid solutions was better with the 2-D model than with the axisymmetric model. The shock-layer thickness predicted by the 2-D solutions was much greater than the experimental data. Even though the axisymmetric solution did not model the bottom of the orbiter at low angles of attack, it still gave much better predictions than the two-dimensional model. Figures 31-37 compare the axisymmetric viscous and inviscid solutions for α = 30-deg. The two-dimensional model would not produce a converged solution at the higher angles of attack. The viscous solution is again in reasonable agreement with the inviscid method of Black and Lewis.

Figures 38-45 show heat-transfer results from the present method and the experimental data of the Tunnel B convective heat-transfer tests. Figure 38 shows the nondimensional heat transfer at α = 0-deg. The predicted values are much higher than the experimental data since the present method predicted a thinner shock layer at the lower angles of attack. Figures 39-44 compare the heat-transfer distributions at various angles of attack and Reynolds numbers/cm ranging from 1.64×10^4 to 9.84 to 10^4. The agreement with the experimental data was good. At the higher angles of attack, i.e. 35- and 45-deg, the predicted values were slightly lower since the present method could not model the crossflow. As the Reynolds number increased, the transition moved upstream toward the nose. In Figs. 43 and 44, the large increase in the heat-transfer distribution is caused by the transition to turbulent flow. Since the present model was for laminar flows only, it could not accurately predict the heat-transfer coefficient in the transitional or turbulent region. Figure 45 shows the upstream movement of the transition regime with increasing Reynolds number at α = 30-deg.

Comparisons with the data of Tunnel F are shown in Figs. 46-51. The agreement with Tunnel F data was good. The present method underpredicted the heat-transfer distribution along the body because Tunnel F used a nitrogen test gas which could not be accurately modeled with the perfect gas, viscous shock-layer program. Figures 46-51 show the predictions of the present method at various angles of attack and Reynolds number/cm ranging from 1.97×10^4 to 1.57×10^5. Again the movement of the transition regime upstream with increasing Reynolds number is apparent in these figures.

Some of the computing times required for these tests are given in Table V. These times were obtained on the IBM 370/158 system at the Virginia Polytechnic Institute and State University. The times are for the perfect gas viscous shock-layer program used in the present work with a convergence test of one percent on the velocity and temperature profiles, an initial step size of $\Delta s = 0.2$ and a maximum step size of $\Delta s_{max} = 1.0$.

IV. CONCLUSIONS

The results of the present work have shown that the perfect gas viscous shock-layer method may be used to obtain accurate predictions of the blunt-body reentry vehicle in relatively short computing times. Comparisons with data from the AEDC/vKF Wind Tunnel tests show that the present method makes good predictions of the wall pressure distribution, stagnation temperature profile, pitot pressure profile and the heat-transfer distribution. Comparisons at the low angles of attack show that the axisymmetric hyperboloid does not model well the flattened bottom of the orbiter which causes a smaller shock-layer thickness and higher heat-transfer distribution. At low angles of attack the axisymmetric solution still gave better predictions of the shock layer than a two-dimensional solution. Finally, at the high angles of attack, solutions using the present method predicted thicker shock-layer thicknesses and lower heat-transfer distributions possibly because of the neglected crossflow terms. More work is needed to see if the addition of the crossflow effects will improve the solution at high angles of attack.

REFERENCES

1. Inouye, M., Rakich, J., and Lomax, H., "A Description of Numerical Methods and Computer Programs for Two-Dimensional and Axisymmetric Supersonic Flow over Blunt Nosed and Flared Bodies," NASA TN D-2970, August 1965.

2. Rizzi, A. W. and Inouye, M., "A Time-Split Finite-Volume Technique for Three-Dimensional Blunt-Body Flow," AIAA Paper 73-133, January 1973.

3. Kutler, P., Reinhardt, W. A., and Warming, R. F., "Multishocked, Three-Dimensional Supersonic Flowfields with Real Gas Effects," AIAA Journal, Vol. 11, No. 5, May 1973, pp. 657-664.

4. Blottner, F. G., "Finite-Difference Methods of Solution of the Boundary-Layer Equations," AIAA Journal, Vol. 8, No. 2, February 1970, pp. 193-206.

5. Lewis, Clark H., "First Order Treatment of Higher-Order Boundary-Layer Effects," The Physics of Fluids, Vol. 13, No. 12, December 1970, pp. 2939-2949.

6. Miner, E. W. and Lewis, Clark H., "Hypersonic Ionizing Air Viscous Shock-Layer Flows Over Nonanalytic Blunt Bodies," NASA CR-2550, May 1975.

7. Davis, R. T., "Numerical Solution of the Hypersonic Viscous Shock-Layer Equations," AIAA Journal, Vol. 8, No. 5, May 1970, pp. 843-851.

8. Davis, R. T., "Hypersonic Flow of a Chemically Reacting Binary Mixture Past a Blunt Body," AIAA Paper No. 70-805, July 1970.

9. Moss, J. N., "Solution for Reacting and Nonreacting Viscous Shock Layers with Multicomponent Diffusion and Mass Injection," PhD Dissertation, Virginia Polytechnic Institute and State University, Blacksburg, Virginia, October 1971.

10. Carter, L. D. and Martindale, W. R., "Test Results From the NASA/Rockwell International Space Shuttle Test (OH9) Conducted in the AEDC-VKF Tunnel B," AEDC-DR-74-9, January 1974.

11. Martindale, W. R., "Test Results From the NASA/Rockwell International Space Shuttle Test (OH4B) Conducted in the AEDC-VKF Tunnel B," AEDC-DR-74-8, January 1974.

12. Boudreau, A. H., "Test Results From the NASA/RI Shuttle Heating Test OH-11 in the AEDC-VKF Tunnel F," AEDC-DR-74-16, February 1974.

13. Adams, J. C., Martindale, W. R., Mayne, A. W., Jr., and Marchand, E. O., "Real Gas Scale Effects on Laminar Boundary-Layer Parameters Including Effects of Entropy-Layer Swallowing," AEDC-DR-74-59, July 1974.

14. Black, R. R. and Lewis, C. H., "Inviscid Supersonic Nonuniform Flows over Sharp and Spherically Blunted Cones at Angle of Attack," ARL 73-0124, August 1973.

TABLE I

AEDC TUNNEL B HEAT TRANSFER TESTS

GROUP NO.	$\rho_\infty \times 10^{-5}$ (slugs/ft³)	T_∞ (°R)	M_∞	α (DEG)	Re/ft $\times 10^6$ (ft⁻¹)	T_B (°R)	$H_{Bref} \times 10^{-2}$ (BTU/ft²-sec-°R)
58	1.3875	93.0	7.92	0	0.693	528.0	2.007
64	1.0770	92.8	7.92	30	0.539	537.0	1.765
67	1.0640	94.6	7.92	35	0.527	540.0	1.778
73	2.029	94.1	7.92	30	1.010	539.0	2.447
76	2.054	93.9	7.92	35	1.020	544.0	2.459
82	3.911	96.5	7.96	30	1.930	544.0	3.479
112	3.910	96.1	7.96	35	1.930	555.0	3.467
134	1.086	93.3	7.92	25	0.542	534.0	1.779
171	3.960	95.2	7.96	25	1.970	547.0	3.467
177	2.040	93.6	7.93	30	1.020	545.0	2.448
181	2.033	93.3	7.93	45	1.020	541.0	2.439
187	3.077	94.8	7.94	30	1.530	550.0	3.039
189	3.069	95.0	7.94	35	1.520	550.0	3.038
199	3.955	95.0	7.96	45	1.970	555.0	3.461
205	4.994	95.8	7.97	30	2.480	547.0	3.917
207	5.021	95.3	7.97	35	2.500	556.0	3.914
213	6.009	97.7	7.98	30	2.950	559.0	4.361
215	6.106	96.1	7.98	35	3.030	560.0	4.348

TABLE II

AEDC TUNNEL B WALL PRESSURE TESTS

GROUP NO.	$\rho_\infty \times 10^{-5}$ (slugs/ft^3)	T_∞ ($^\circ$R)	M_∞	α (DEG)	Re/ft $\times 10^6$ (ft^{-1})	T_B ($^\circ$R)
30	2.272	98.2	7.95	30	1.110	600.0
31	1.378	98.9	7.92	30	0.669	565.0
32	1.380	99.1	7.92	35	0.669	545.0
33	1.383	98.8	7.92	25	0.672	545.0
34	1.387	98.3	7.92	15	0.675	555.0

TABLE III

AEDC TUNNEL B FLOWFIELD SURVEYS

GROUP NO.	$\rho_\infty \times 10^{-5}$ (slugs/ft^3)	T_∞ ($^\circ$R)	M_∞	α (DEG)	Re/ft $\times 10^6$ (ft^{-1})	T_B ($^\circ$R)
8	1.377	99.4	7.92	30	0.685	605.0
18	1.392	98.8	7.92	35	0.676	590.0
46	1.386	98.0	7.92	25	0.675	585.0
50	1.368	99.0	7.92	15	0.672	575.0
60	2.256	97.7	7.95	30	1.110	600.0

TABLE IV

AEDC TUNNEL F HEAT TRANSFER TESTS

RUN NO.	$\rho_\infty \times 10^{-5}$ (slugs/ft^3)	T_∞ (°R)	M_∞	α (DEG)	Re/ft $\times 10^6$ (ft^{-1})	T_B (°R)	$H_{Bref} \times 10^{-2}$ (BTU/ft^2-sec-°R)
4504	3.2386	109.5	10.34	25	1.999	540.0	4.97
4510	5.8432	90.8	10.74	30	4.1152	540.0	6.39
4512	6.2721	94.6	11.92	30	4.8053	540.0	8.05
4521	1.1189	155.4	11.18	25	0.6267	540.0	4.26
4523	3.1671	123.3	11.42	45	2.0352	540.0	6.26
4524	5.4858	93.6	11.58	30	4.1031	540.0	7.09
4526	2.2223	173.8	14.35	35	2.3182	540.0	5.12
4527	1.6380	90.2	14.1	35	1.5201	540.0	4.93

-22-

TABLE V. COMPUTING TIMES

CONDITIONS	NO. OF STATIONS	NO. OF GLOBAL ITERATIONS	TOTAL NO. OF ITERATIONS	EXECUTION TIME MIN:SEC
TUNNEL B	180	4	427	4:30
TUNNEL F	178	4	426	4:09

139 Orbiter, $\alpha = 30$ deg
31-deg Hyperboloid
$r_n/L = 0.02635$
Equation of Hyperbola

$$\frac{y'^2}{2x'} = \frac{x'\tan^2 31°}{2} = r_n$$

U_∞

y'/L

x'/L

x/L
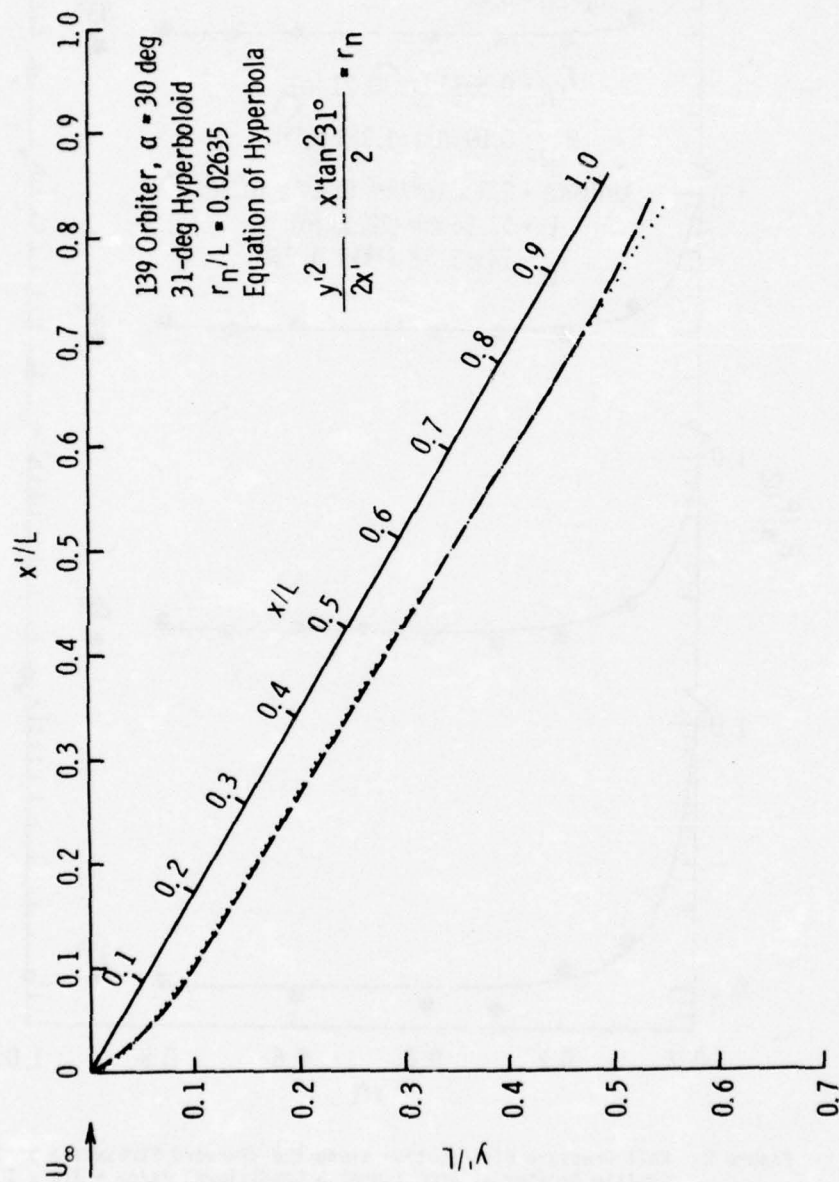
Figure 1: Comparison of the 31-deg Half Angle Hyperboloid Geometry with the Windward Streamline of the Shuttle Orbiter.
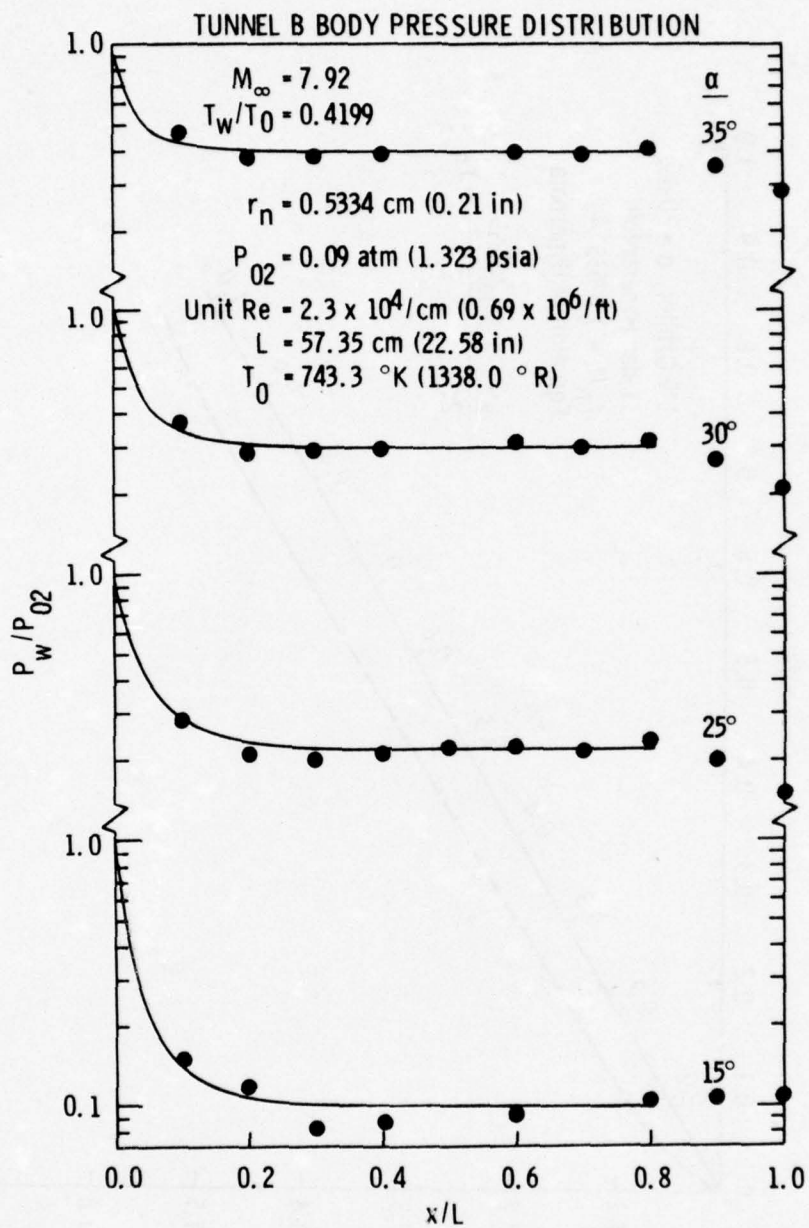
Figure 2: Wall Pressure Distribution along the Windward Streamline of the Shuttle Orbiter at AEDC Tunnel B Conditions, Re/cm = 2.3×10^4.
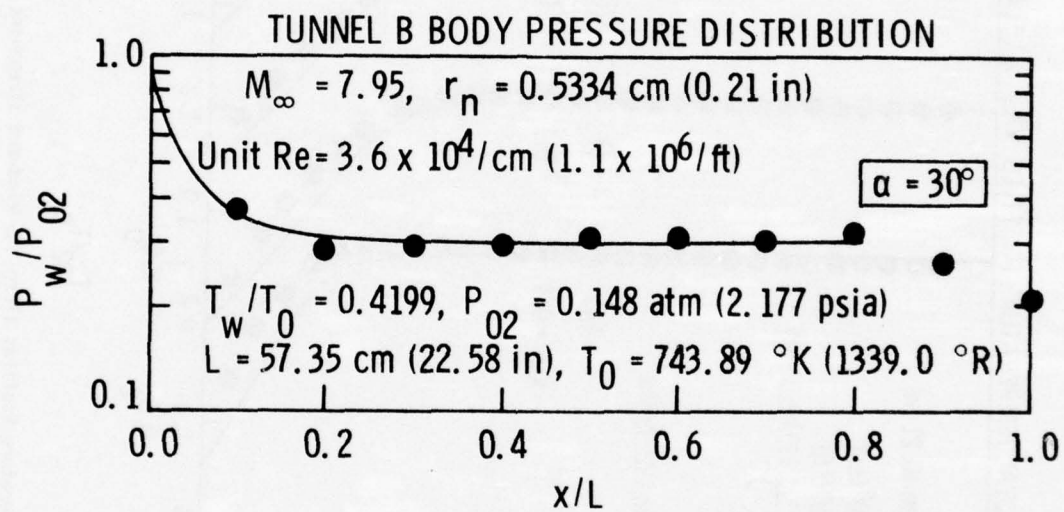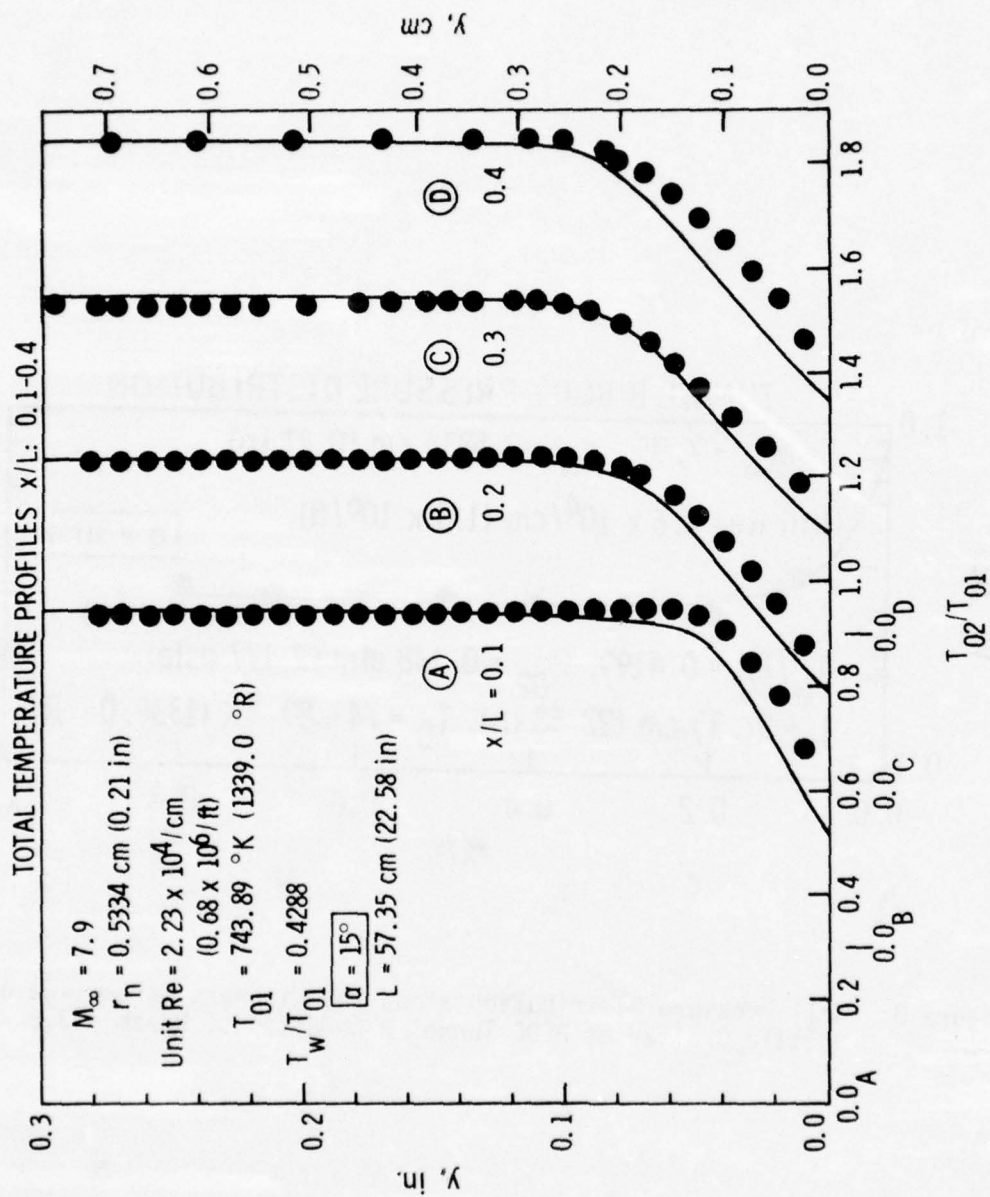
TUNNEL B BODY PRESSURE DISTRIBUTION

$M_\infty = 7.95$, $r_n = 0.5334$ cm (0.21 in)

Unit Re = 3.6×10^4/cm (1.1×10^6/ft)

$\alpha = 30°$

$T_w/T_0 = 0.4199$, $P_{02} = 0.148$ atm (2.177 psia)

$L = 57.35$ cm (22.58 in), $T_0 = 743.89$ °K (1339.0 °R)

Figure 3: Wall Pressure Distribution along the Windward Streamline of the Shuttle Orbiter at AEDC Tunnel B Conditions, Re/cm = 3.6×10^4.

26

Figure 4: Total Temperature Profiles along the Windward Streamline of the Shuttle Orbiter at AEDC Tunnel B Conditions, α = 15-deg.
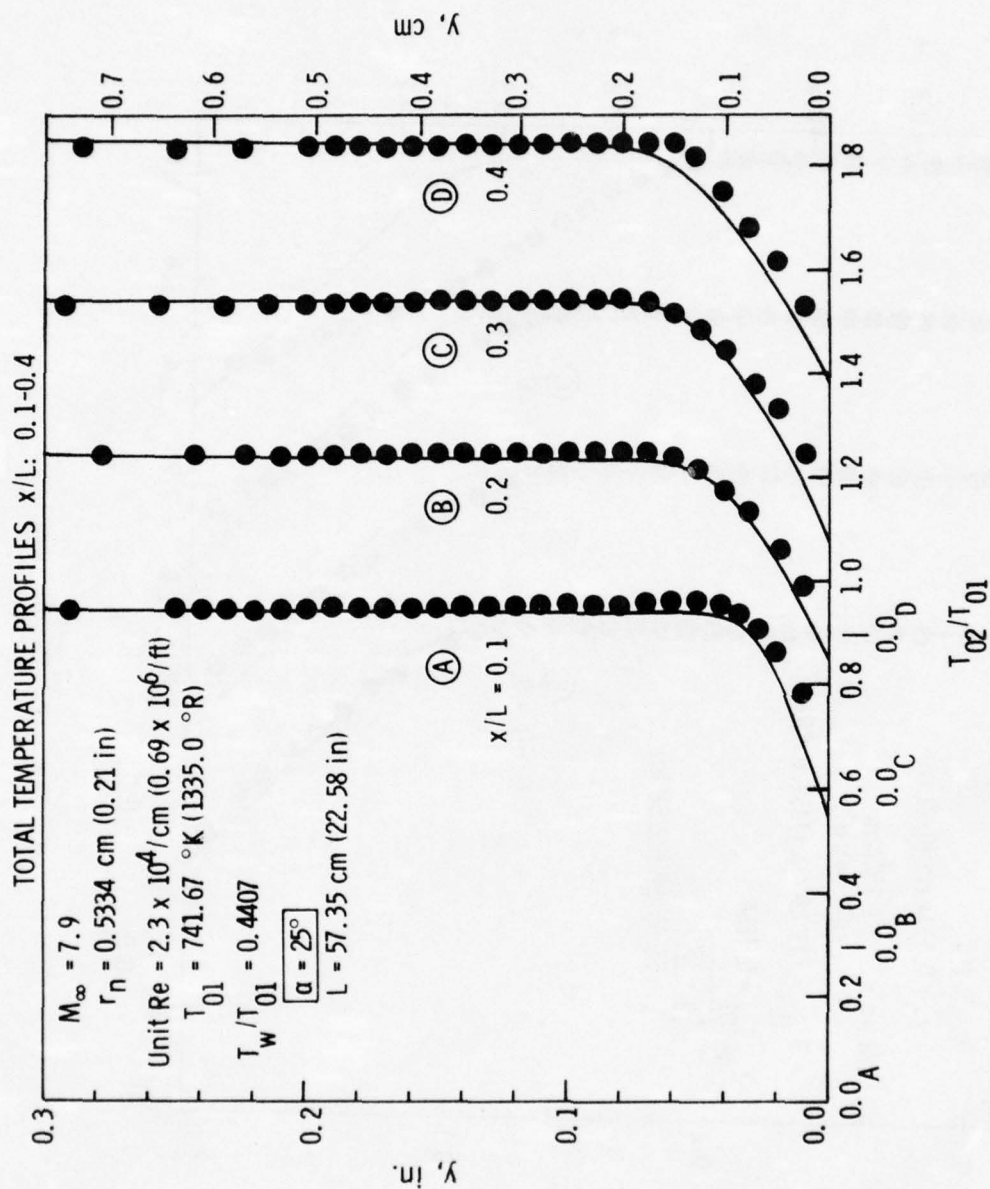
TOTAL TEMPERATURE PROFILES x/L: 0.5-0.8

$M_\infty = 7.9$

$r_n = 0.5334$ cm (0.21 in)

Unit Re = 2.23×10^4/cm
(0.68×10^6/ft)

$T_{01} = 743.89$ °K (1339.0 °R)

$T_w/T_{01} = 0.4288$

$\alpha = 15°$

$L = 57.35$ cm (22.58 in)

T_{02}/T_{01}

y, cm

y, in.

Figure 4: Continued.

28

TOTAL TEMPERATURE PROFILES x/L: 0.1-0.4

y, cm

$M_\infty = 7.9$

$r_n = 0.5334$ cm (0.21 in)

Unit Re = 2.3×10^4/cm (0.69×10^6/ft)

$T_{01} = 741.67 \,^\circ K$ (1335.0 $^\circ R$)

$T_w/T_{01} = 0.4407$

$\alpha = 25^\circ$

L = 57.35 cm (22.58 in)

Ⓐ x/L = 0.1

Ⓑ 0.2

Ⓒ 0.3

Ⓓ 0.4

T_{02}/T_{01}

y, in.
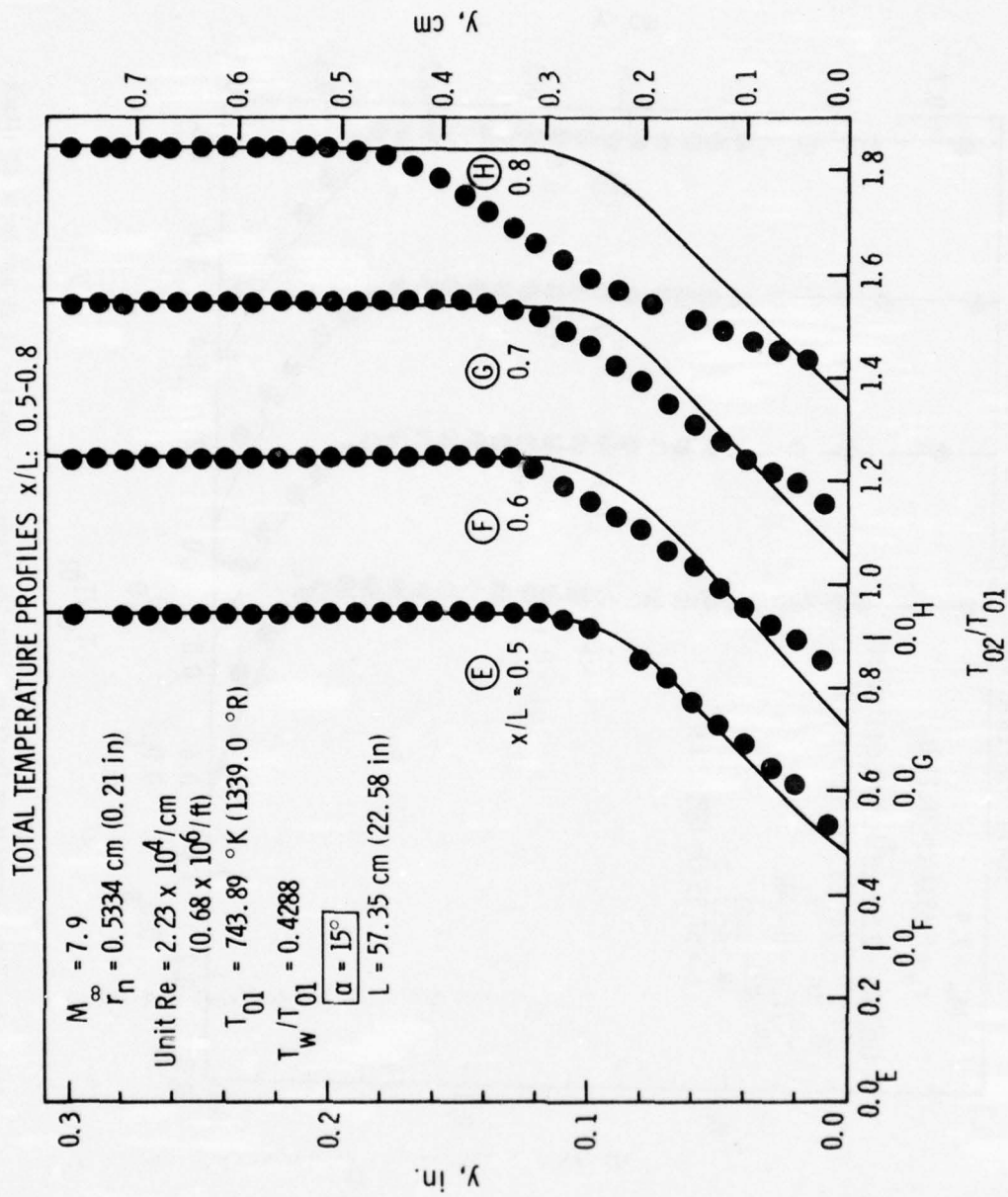
Figure 5: Total Temperature Profiles along the Windward Streamline at 25-deg Angle of Attack.

29

Figure 5: Continued.

TOTAL TEMPERATURE PROFILES x/L: 0.5-0.8

$M_\infty = 7.9$
$r_n = 0.5334$ cm (0.21 in)
Unit Re = 2.3×10^4/cm (0.69×10^6/ft)
$T_{01} = 741.67$ °K (1335.0 °R)
$T_w/T_{01} = 0.4407$
$\alpha = 25°$
$L = 57.35$ cm (22.58 in)

x/L = 0.5

y, cm

y, in.

T_{02}/T_{01}
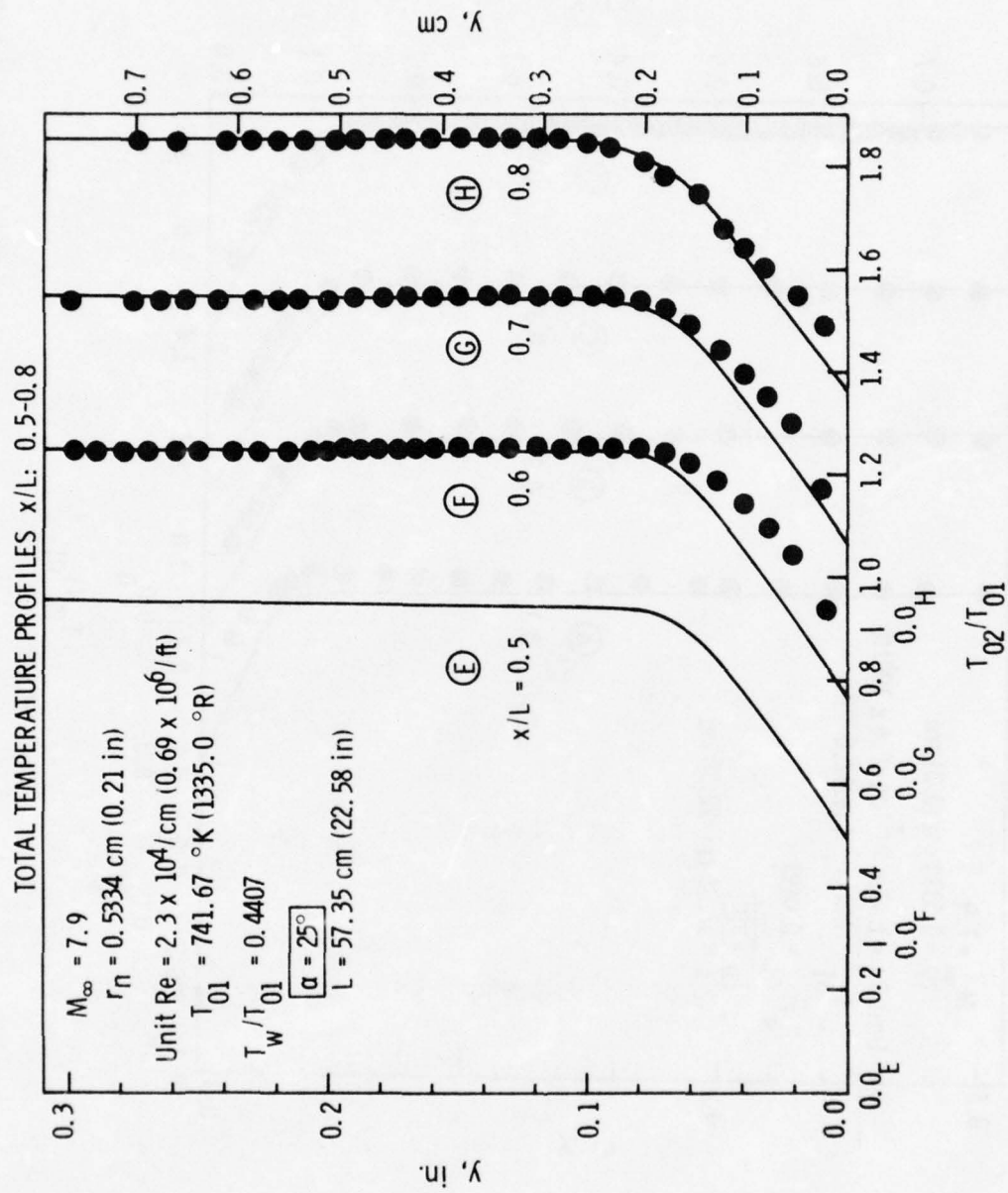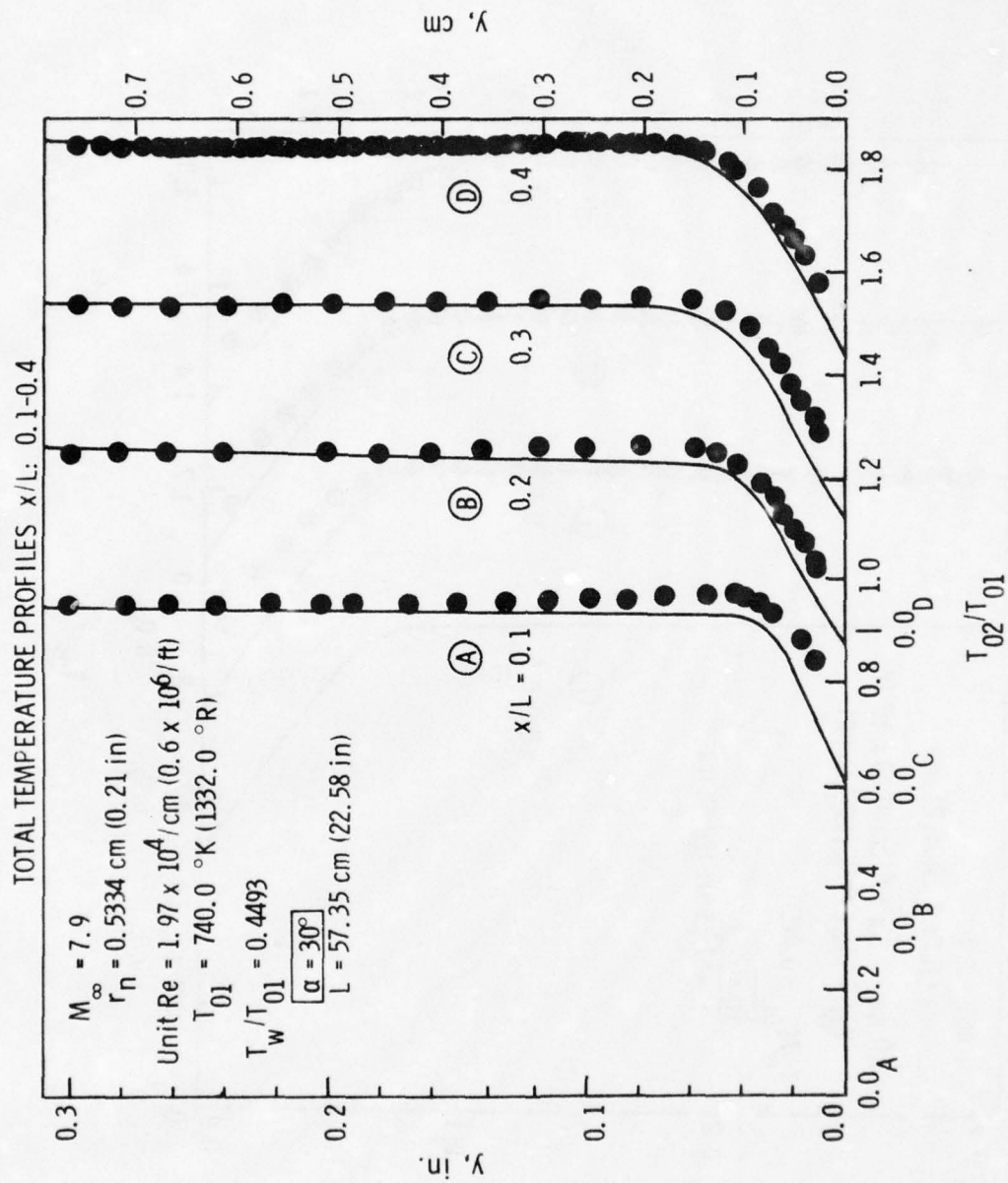
Figure 6: Total Temperature Profiles along the Windward Streamline at 30-deg Angle of Attack, Re/cm = 1.97 x 10⁴.
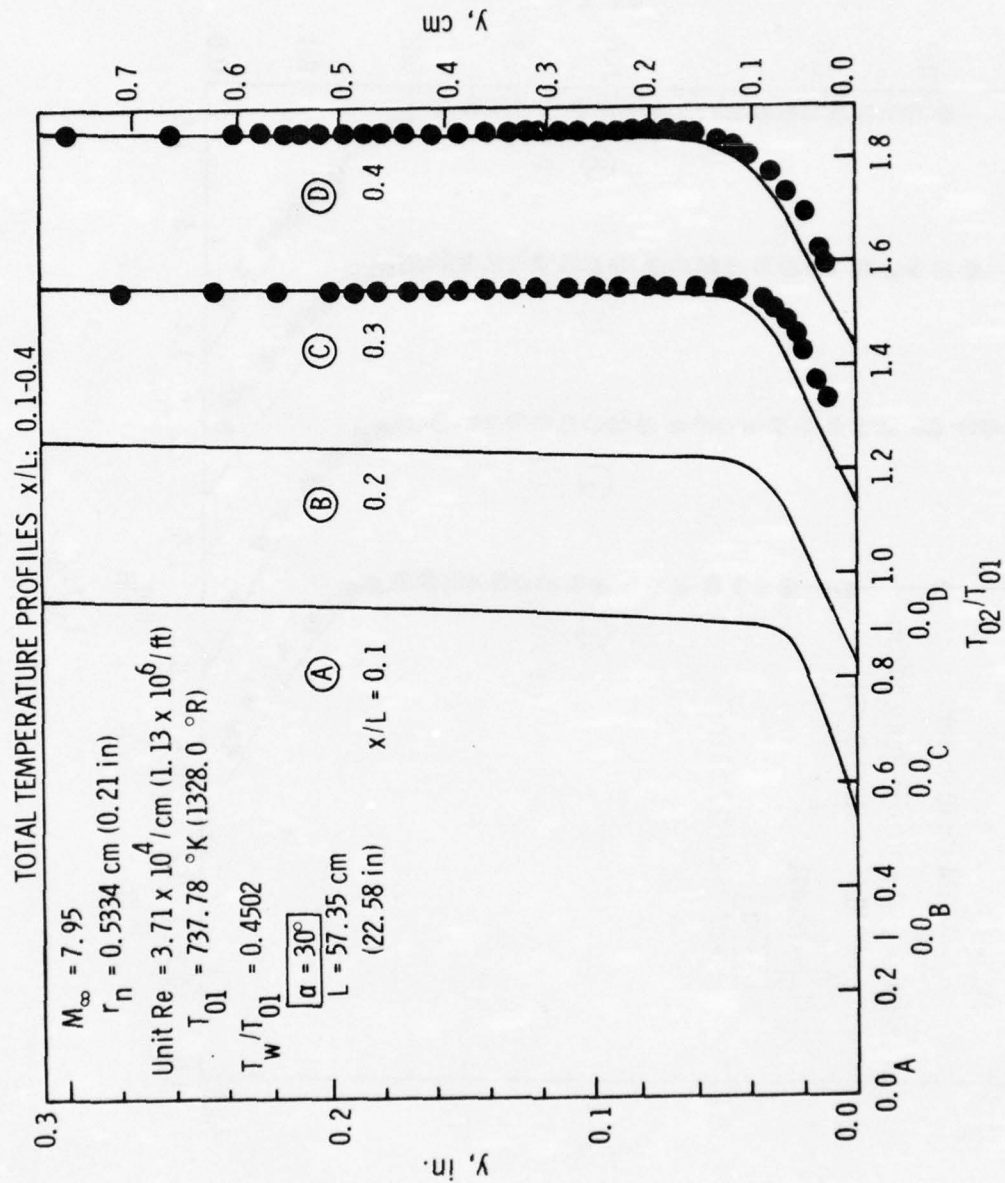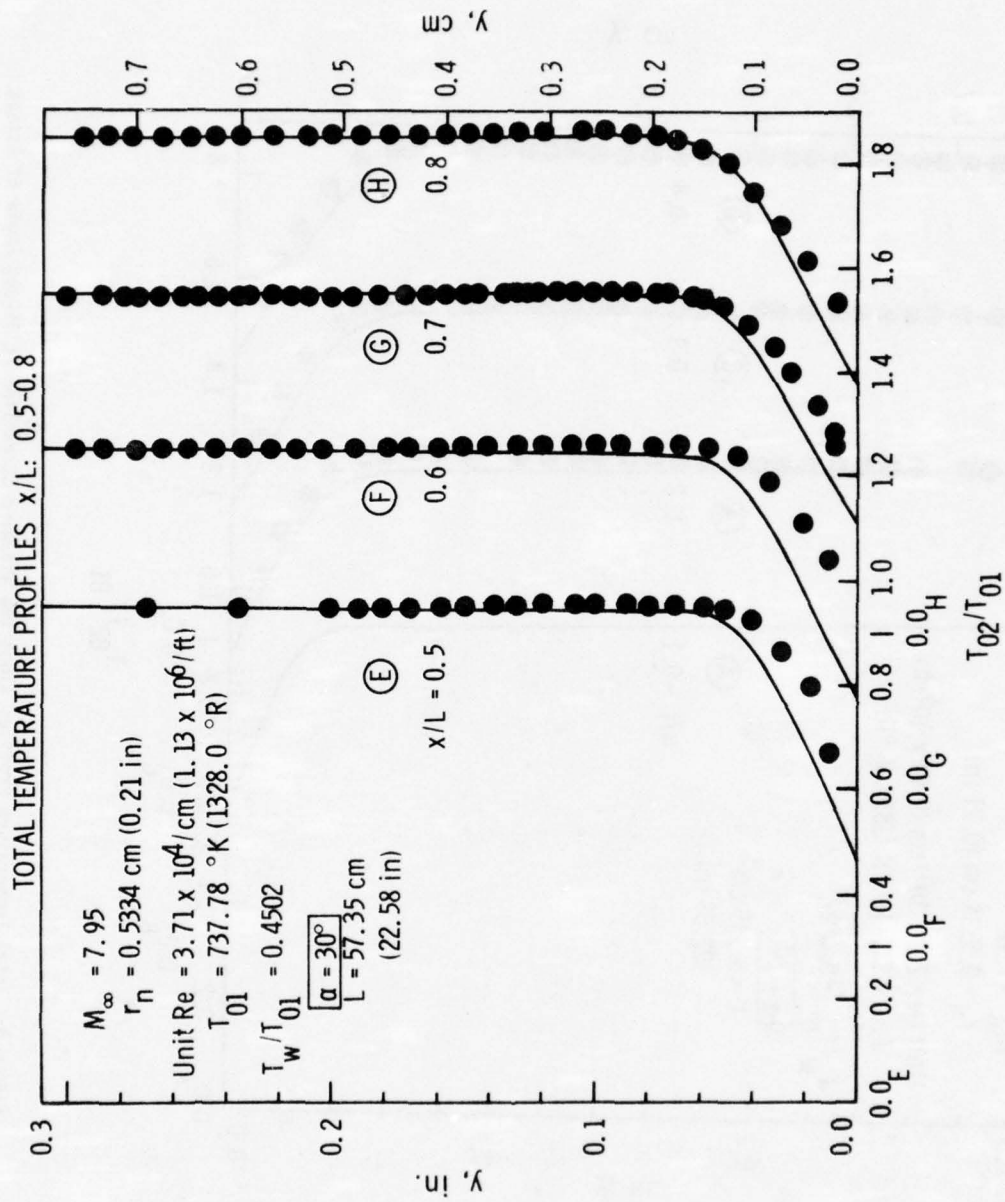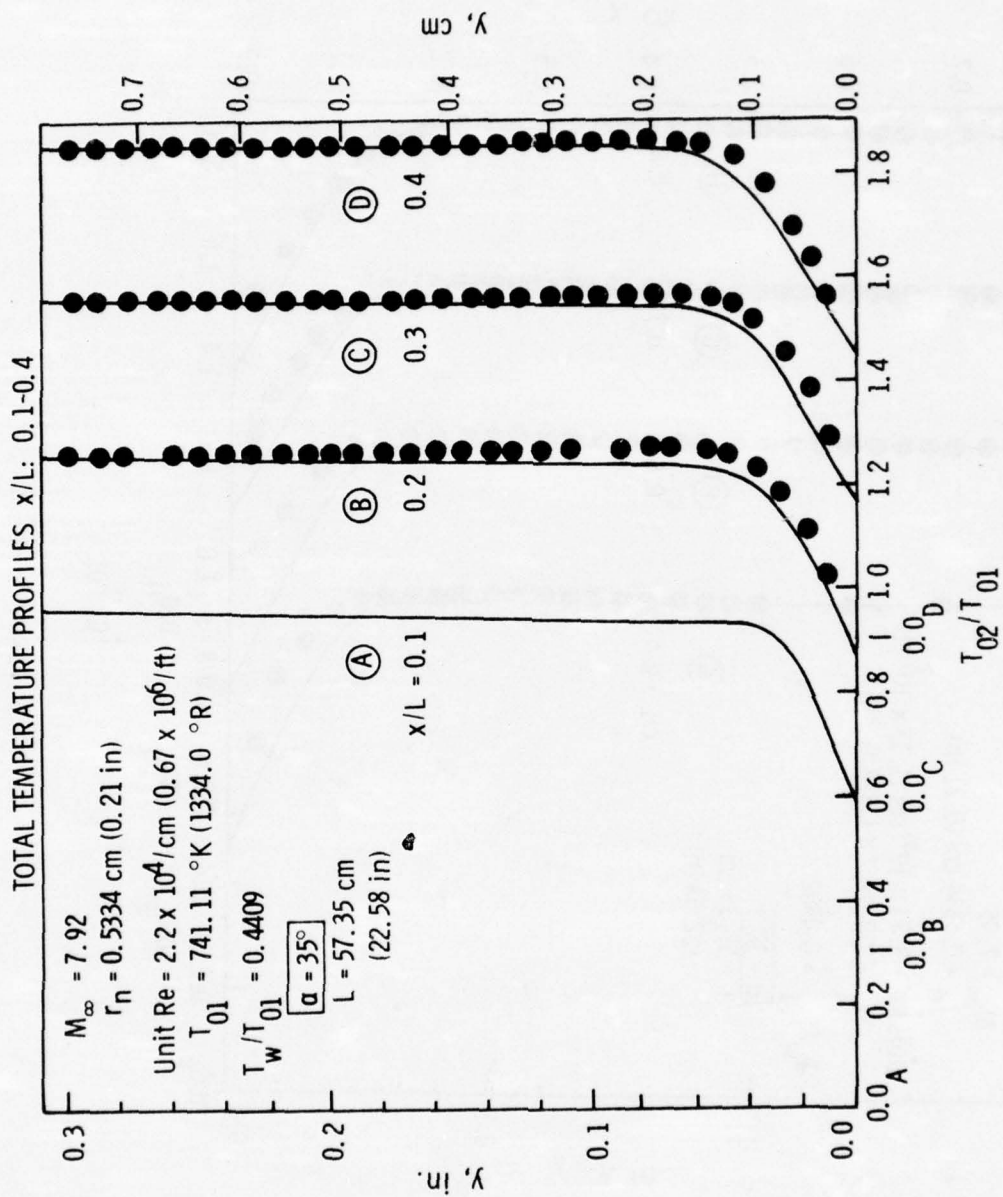
31

Figure 6: Continued.

32

TOTAL TEMPERATURE PROFILES x/L: 0.1-0.4

y, cm

0.7 0.6 0.5 0.4 0.3 0.2 0.1 0.0

1.8 1.6 1.4 1.2 1.0 0.8 0.6 0.4 0.2

T_{02}/T_{01}

Ⓐ x/L = 0.1   Ⓑ 0.2   Ⓒ 0.3   Ⓓ 0.4

0.0_A 0.0_B 0.0_C 0.0_D

$M_\infty = 7.95$
$r_n = 0.5334$ cm (0.21 in)
Unit Re $= 3.71 \times 10^4$/cm (1.13×10^6/ft)
$T_{01} = 737.78$ °K (1328.0 °R)
$T_w/T_{01} = 0.4502$
$\alpha = 30°$
$L = 57.35$ cm
(22.58 in)

0.3 0.2 0.1 0.0

y, in.
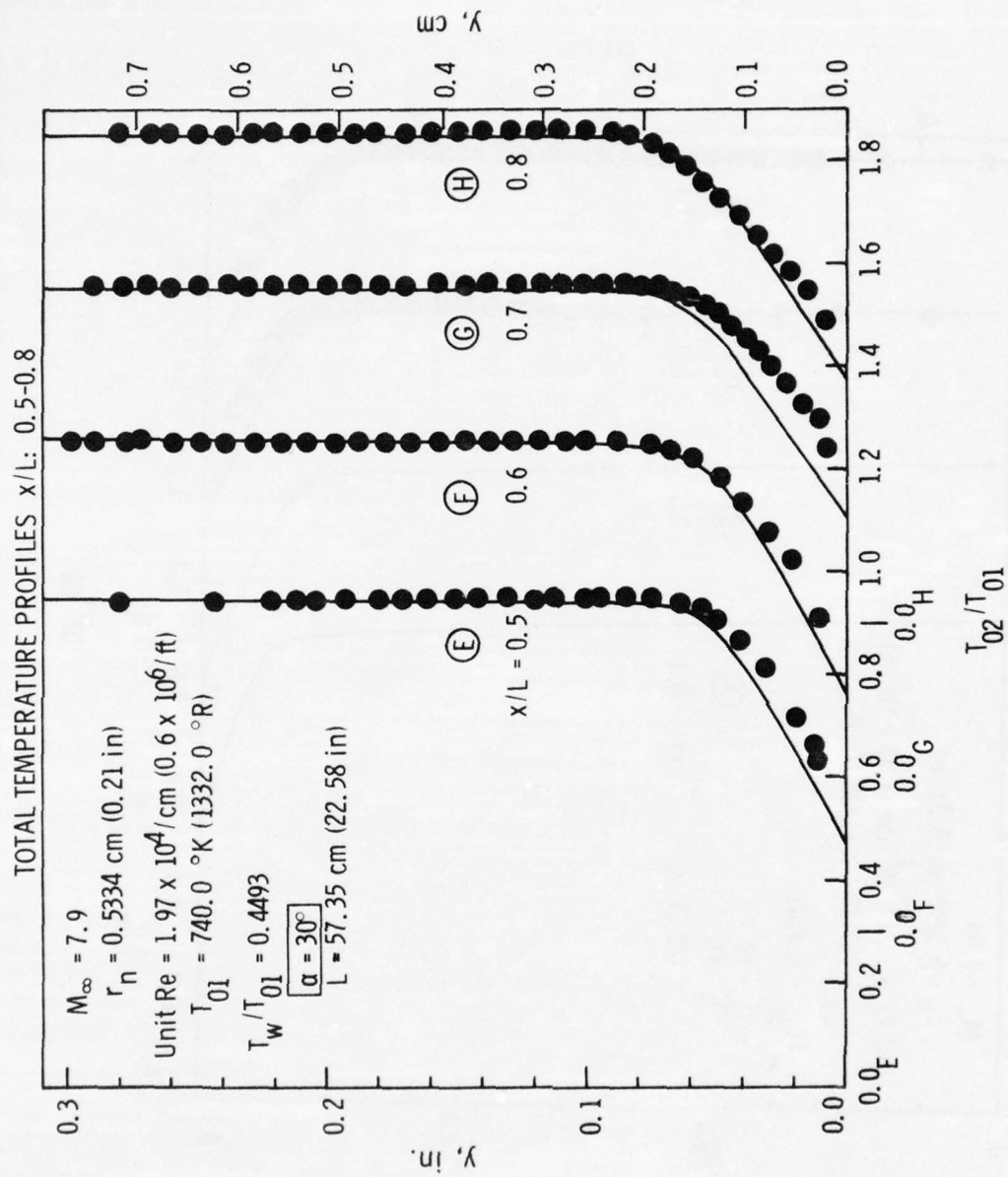
Figure 7: Total Temperature Profiles along the Windward Streamline at 30-deg Angle of Attack, Re/cm = 3.71×10^4.

33

TOTAL TEMPERATURE PROFILES x/L: 0.5-0.8

y, cm

0.7 0.6 0.5 0.4 0.3 0.2 0.1 0.0

$M_\infty = 7.95$
$r_n = 0.5334$ cm (0.21 in)
Unit Re $= 3.71 \times 10^4$/cm (1.13×10^6/ft)
$T_{01} = 737.78$ °K (1328.0 °R)
$T_w/T_{01} = 0.4502$
$\alpha = 30°$
$L = 57.35$ cm (22.58 in)

Ⓗ 0.8

Ⓖ 0.7

Ⓕ 0.6

Ⓔ x/L = 0.5

0.0_H

T_{02}/T_{01}

0.0_G

0.0_F

0.0_E

1.8 1.6 1.4 1.2 1.0 0.8 0.6 0.4 0.2 0.0

y, in.

0.3 0.2 0.1 0.0

Figure 7: Continued.

34

TOTAL TEMPERATURE PROFILES x/L: 0.1-0.4

y, cm

y, in.

$M_\infty = 7.92$

$r_n = 0.5334$ cm (0.21 in)

Unit Re = 2.2×10^4/cm (0.67×10^6/ft)

$T_{01} = 741.11$ °K (1334.0 °R)

$T_w/T_{01} = 0.4409$

$\alpha = 35°$

L = 57.35 cm (22.58 in)

Ⓐ x/L = 0.1

Ⓑ 0.2

Ⓒ 0.3

Ⓓ 0.4

T_{02}/T_{01}

Figure 8: Total Temperature Profiles along the Windward Streamline at 35-deg Angle of Attack.

35
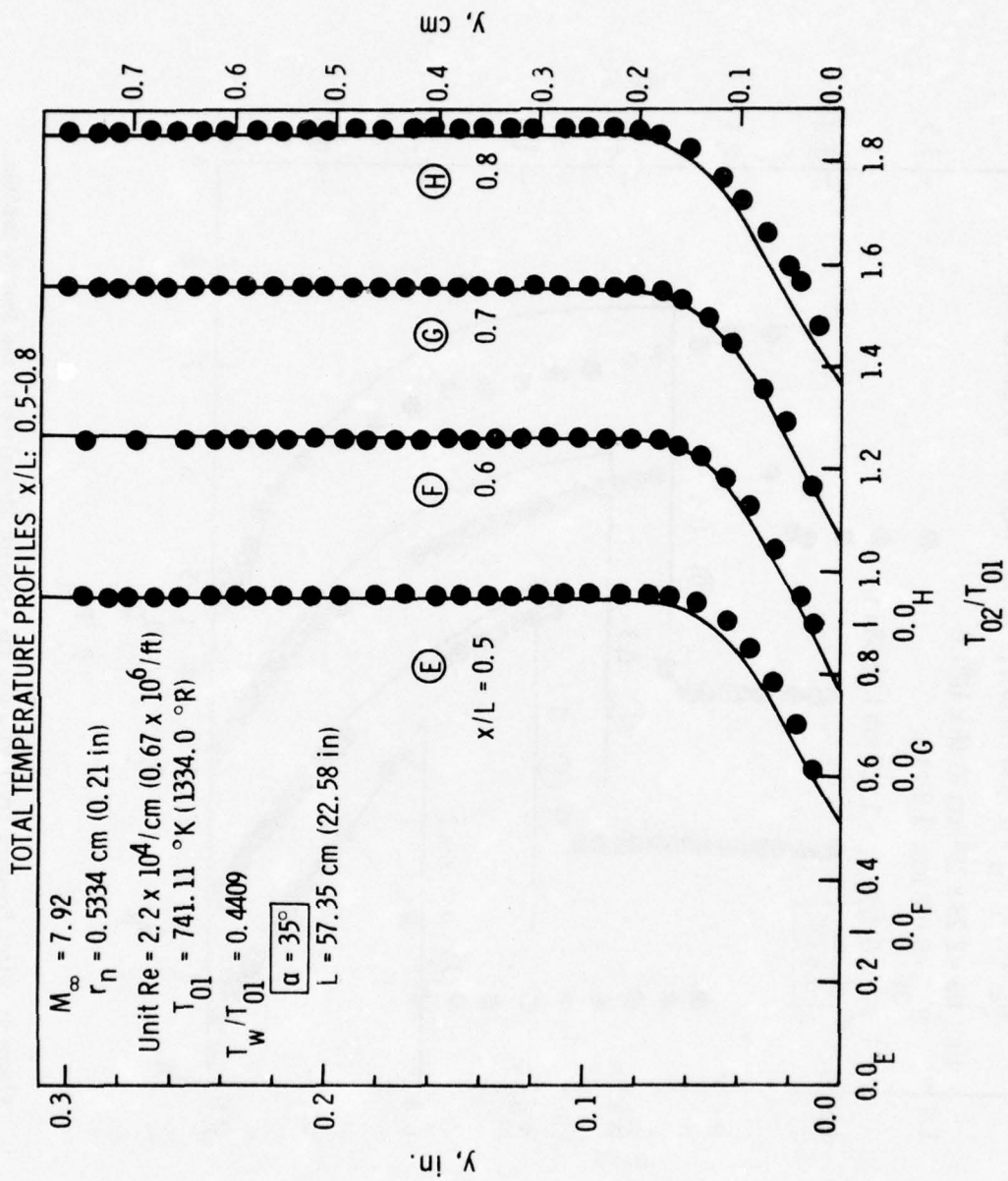
Figure 8: Continued.
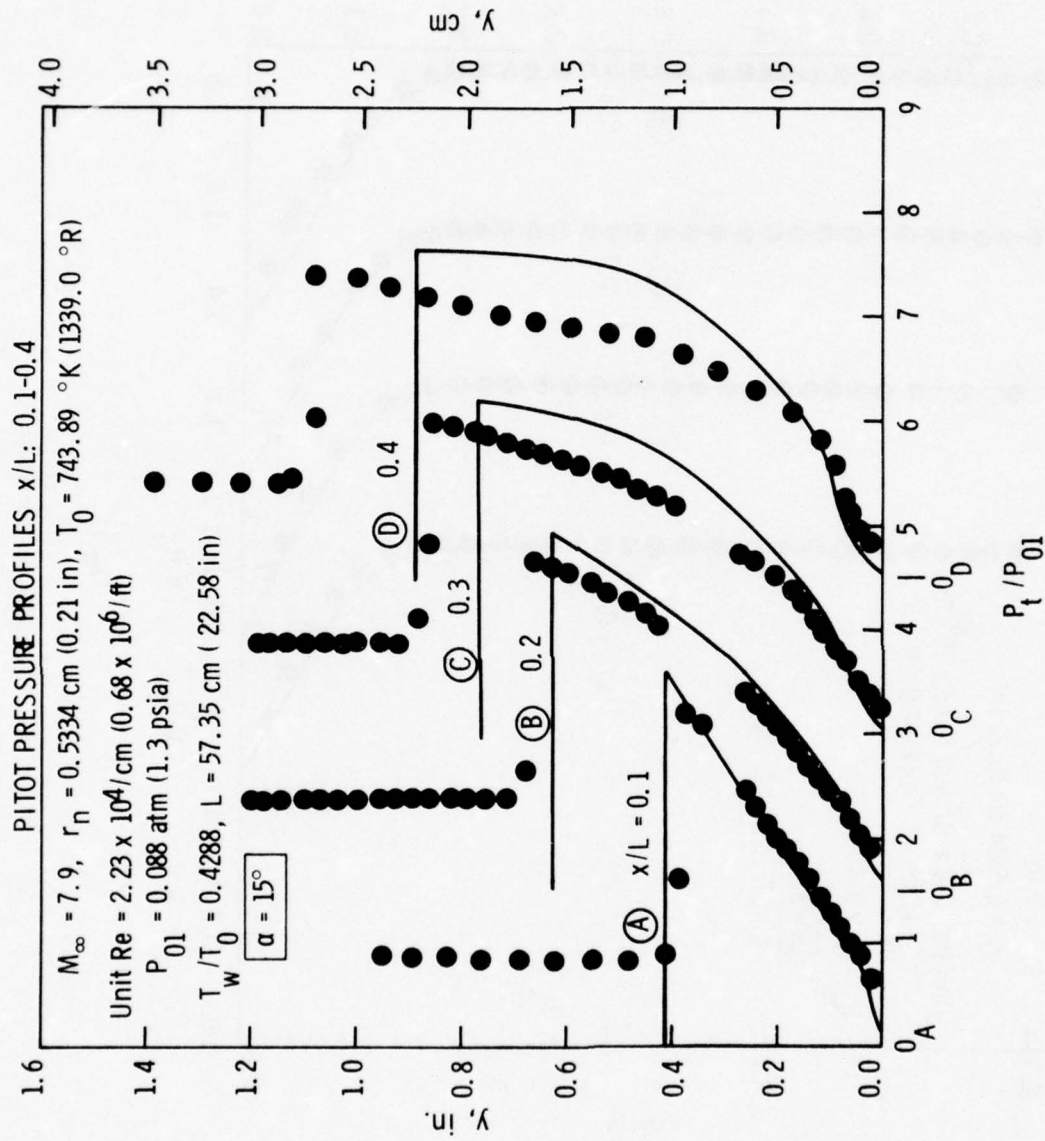
Figure 9: Pitot Pressure Profiles along the Windward Streamline of the Shuttle Orbiter, α = 15-deg.

37

PITOT PRESSURE PROFILES x/L: 0.5-0.8

$M_\infty = 7.9$, $r_n = 0.5334$ cm (0.21 in)   L = 57.35 cm (22.58 in)

Unit Re = 2.23×10^4/cm (0.68×10^6/ft)
$T_0 = 743.89$ °K (1339.0 °R)

x/L = 0.5

$P_{01} = 0.088$ atm
(1.3 psia)
$T_w/T_0 = 0.4288$
$\alpha = 15°$

y, cm

y, in.

P_t/P_{01}

Figure 9: Continued.

38

PITOT PRESSURE PROFILES x/L: 0.1-0.4

$M_\infty = 7.9$, $r_n = 0.5334$ cm (0.21 in), $L = 57.35$ cm (22.58 in)

Unit Re = 2.3×10^4/cm (0.69×10^6/ft)

$P_{01} = 0.088$ atm (1.3 psia)

$T_w/T_0 = 0.4407$

$T_0 = 741.67$ °K
(1335.0 °R)

$\alpha = 25°$
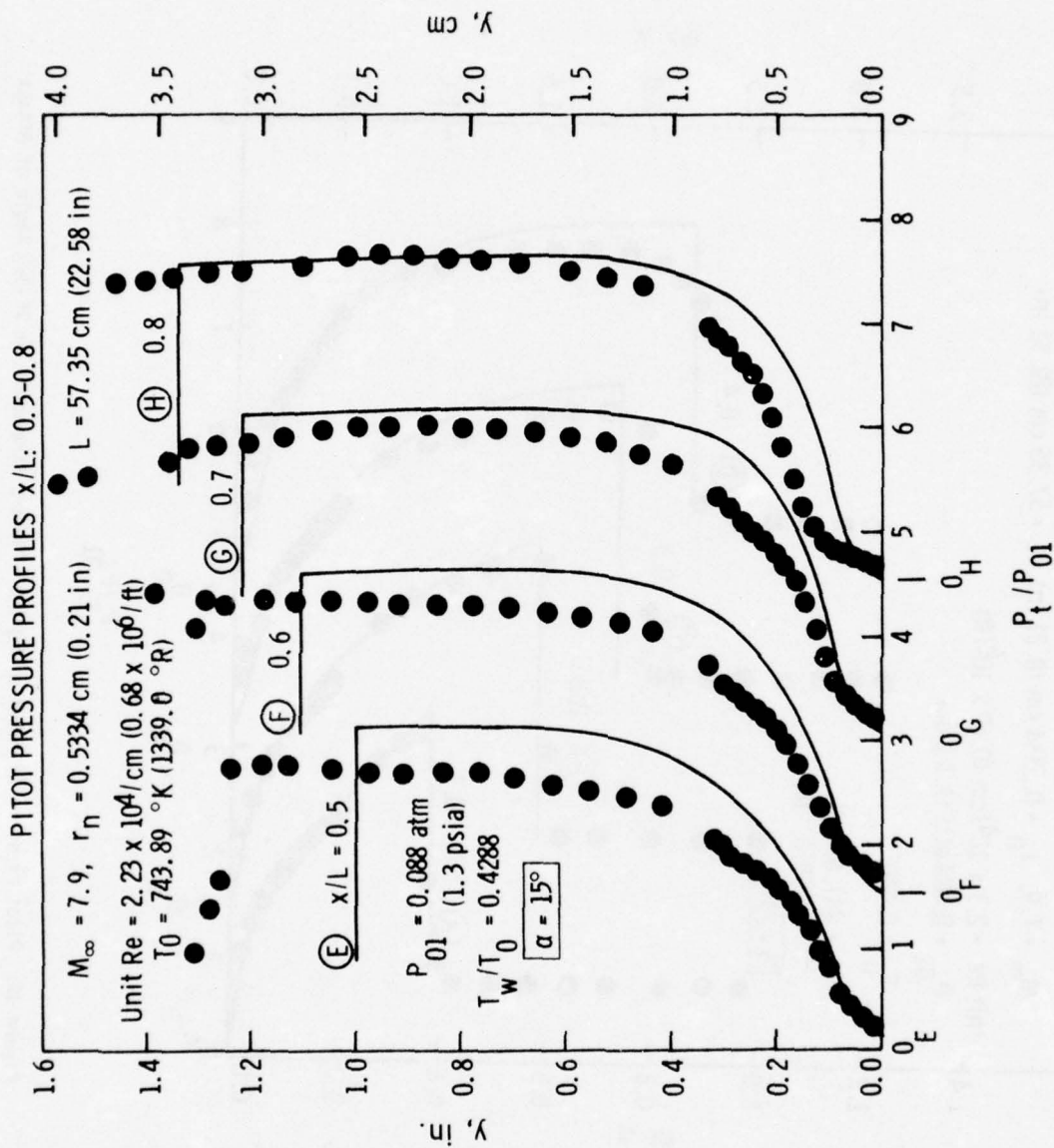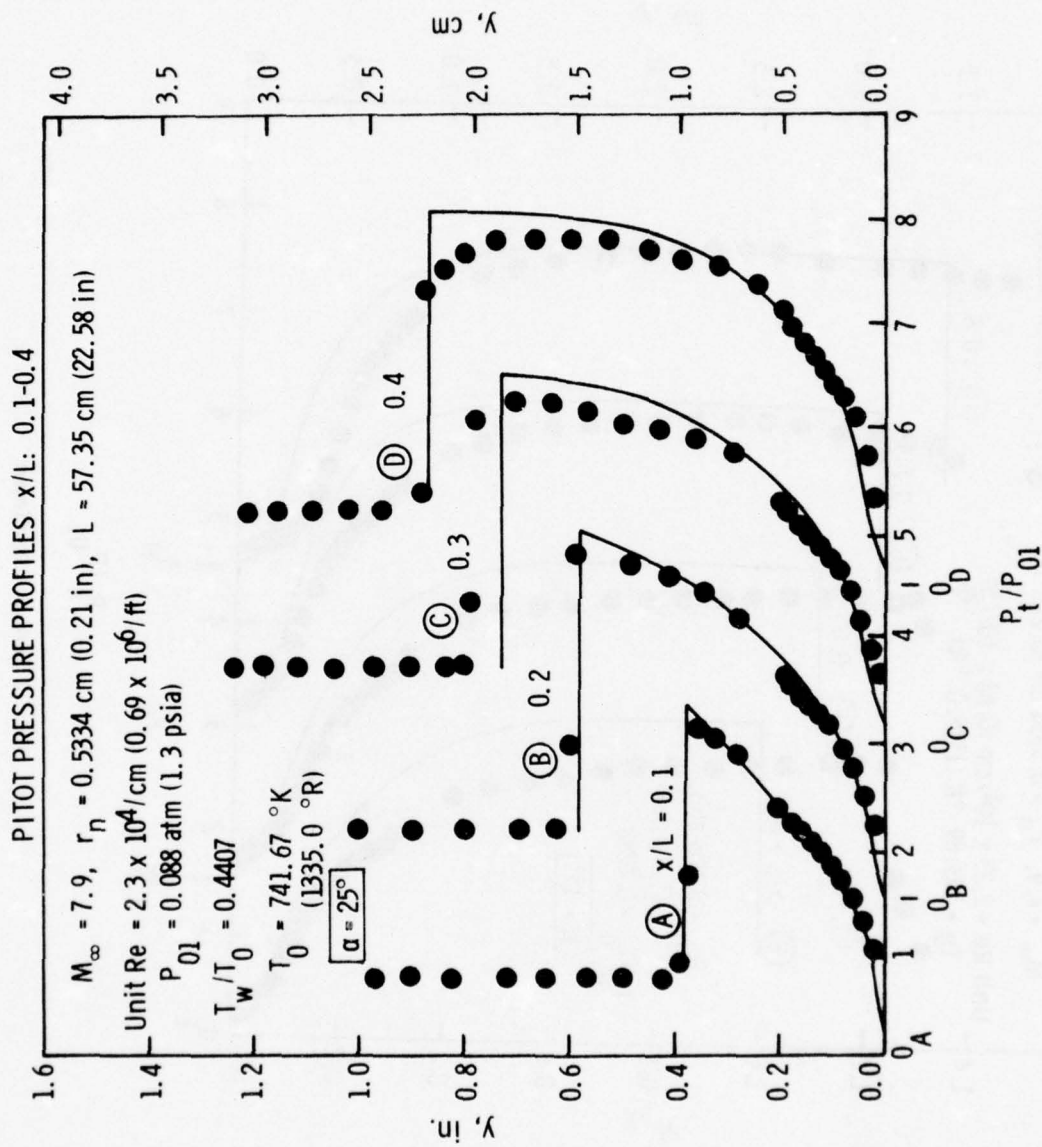
Figure 10: Pitot Pressure Profiles along the Windward Streamline at 25-deg Angle of Attack.

39

Figure 10: Continued.

PITOT PRESSURE PROFILES x/L: 0.5-0.8

$M_\infty = 7.9$, $r_n = 0.5334$ cm (0.21 in)

Unit Re = 2.3×10^4/cm (0.69×10^6/ft)

$P_{01} = 0.088$ atm (1.3 psia)

$T_w/T_0 = 0.4407$

$T_0 = 741.67$ °K (1335.0 °R)

$\alpha = 25°$

$L = 57.35$ cm (22.58 in)

40
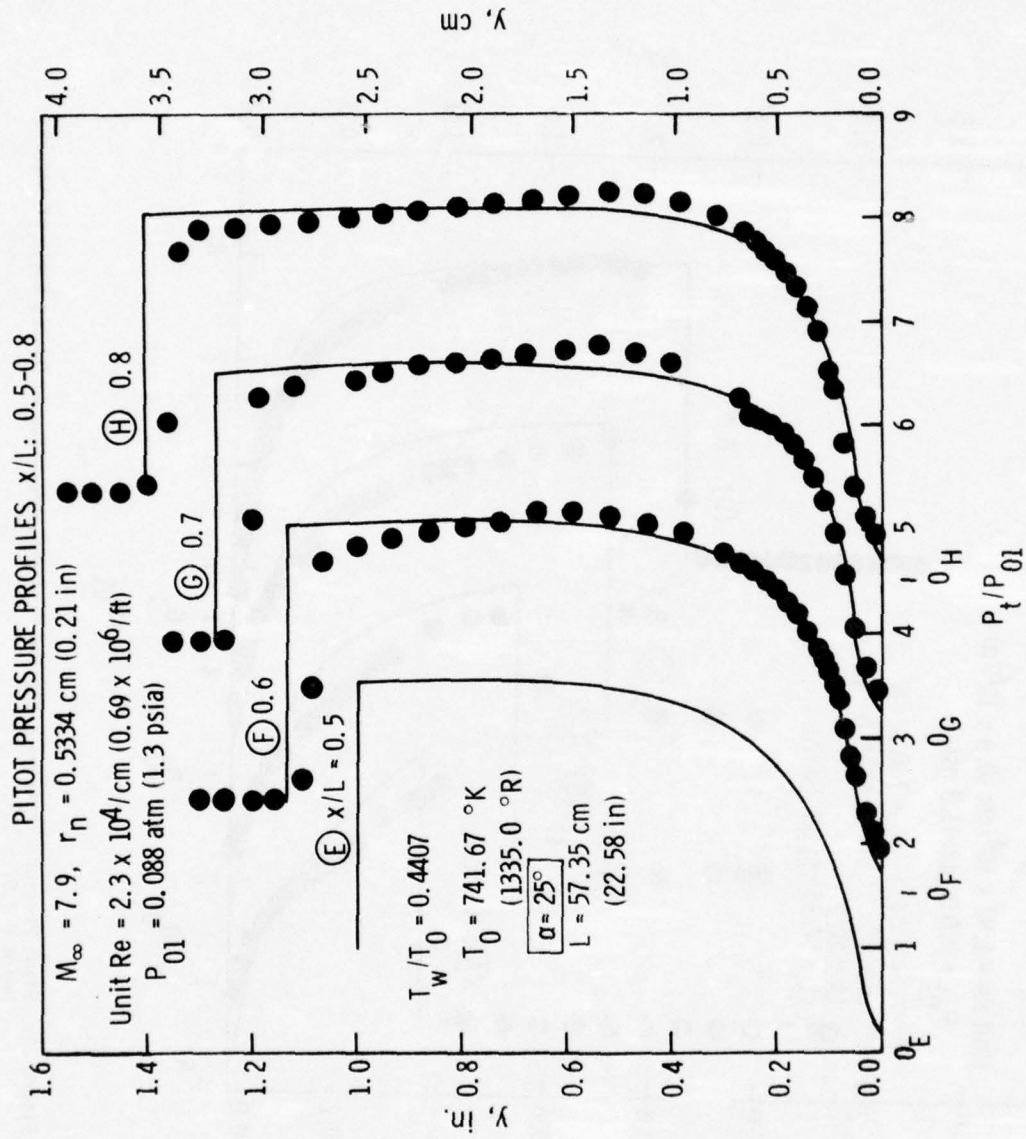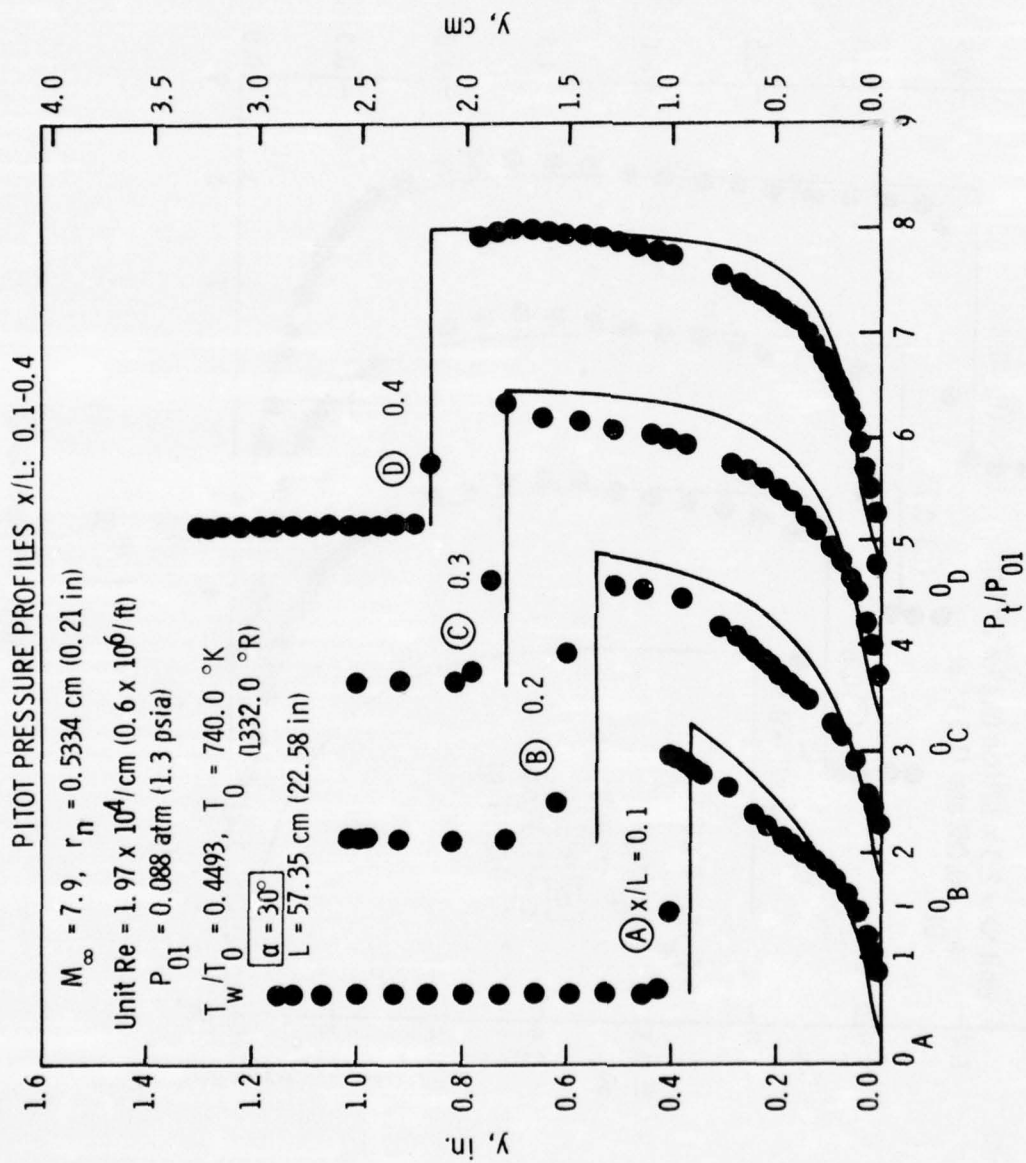
Figure 11: Pitot Pressure Profiles along the Windward Streamline at 30-deg Angle of Attack, Re/cm = 1.97 x 10⁴.

41

PITOT PRESSURE PROFILES x/L: 0.5-0.8

$M_\infty = 7.9$, $r_n = 0.5334$ cm (0.21 in)

Unit Re = 1.97×10^4/cm
(0.6×10^6/ft)

$P_{01} = 0.088$ atm
(1.3 psia)

$T_w/T_0 = 0.4493$

$T_0 = 740.0$ °K
(1332.0 °R)

$\alpha = 30°$

L = 57.35 cm
(22.58 in)

Figure 11: Continued.

42

PITOT PRESSURE PROFILES x/L: 0.1-0.4

$M_\infty = 7.95$, $r_n = 0.5334$ cm (0.21 in)

Unit Re = 3.71×10^4/cm (0.113×10^7/ft)

$P_{01} = 0.15$ atm (2.193 psia)

$T_w/T_0 = 0.4502$

$T_0 = 737.78$ °K (1328.0 °R)

$\boxed{a = 30°}$

L = 57.35 cm (22.58 in)
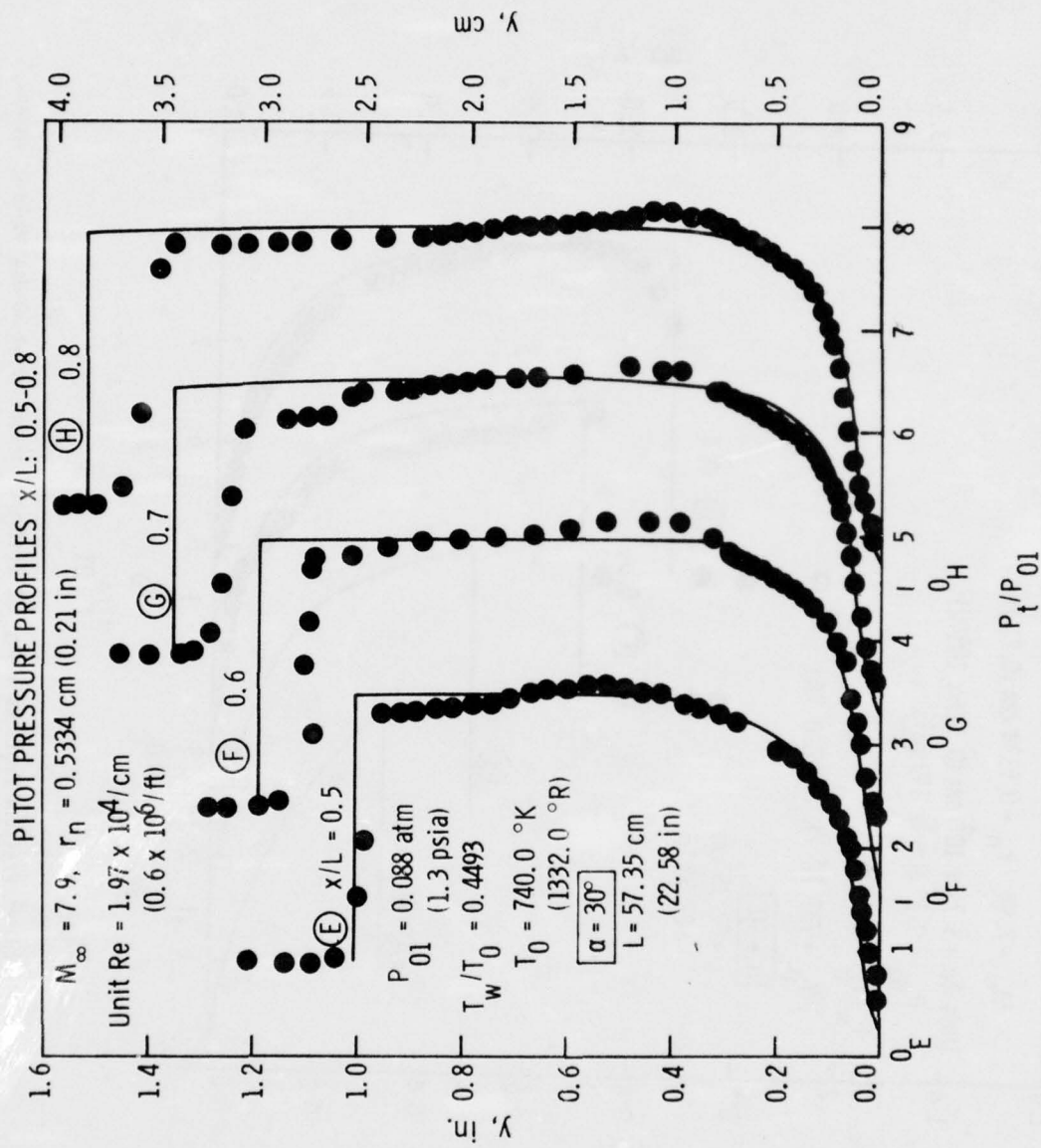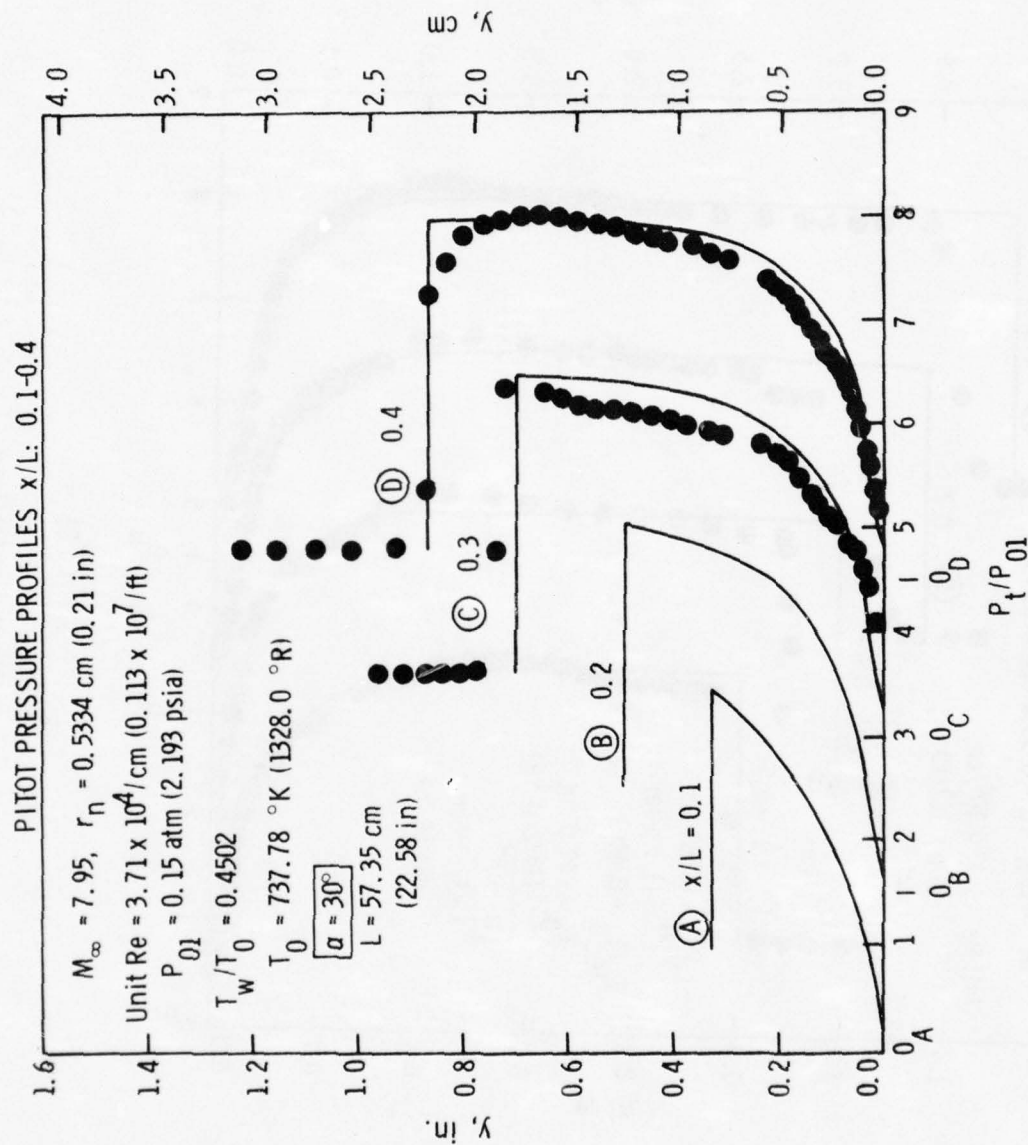
Figure 12: Pitot Pressure Profiles along the Windward Streamline at 30-deg Angle of Attack, Re/cm = 3.71×10^4.

43

PITOT PRESSURE PROFILES x/L: 0.5-0.8

y, cm

$M_\infty = 7.95$, $r_n = 0.5334$ cm (0.21 in)

Unit Re = 3.71×10^4/cm (0.113×10^7/ft)

$P_{01} = 0.15$ atm (2.193 psia)

(H) 0.8

(G) 0.7

(F) 0.6

(E) x/L = 0.5

$T_w/T_0 = 0.4502$

$T_0 = 737.78$ °K
(1328.0 °R)

$\alpha = 30°$

$L = 57.35$ cm
(22.58 in)

P_t/P_{01}

0_E 0_F 0_G 0_H

y, in.
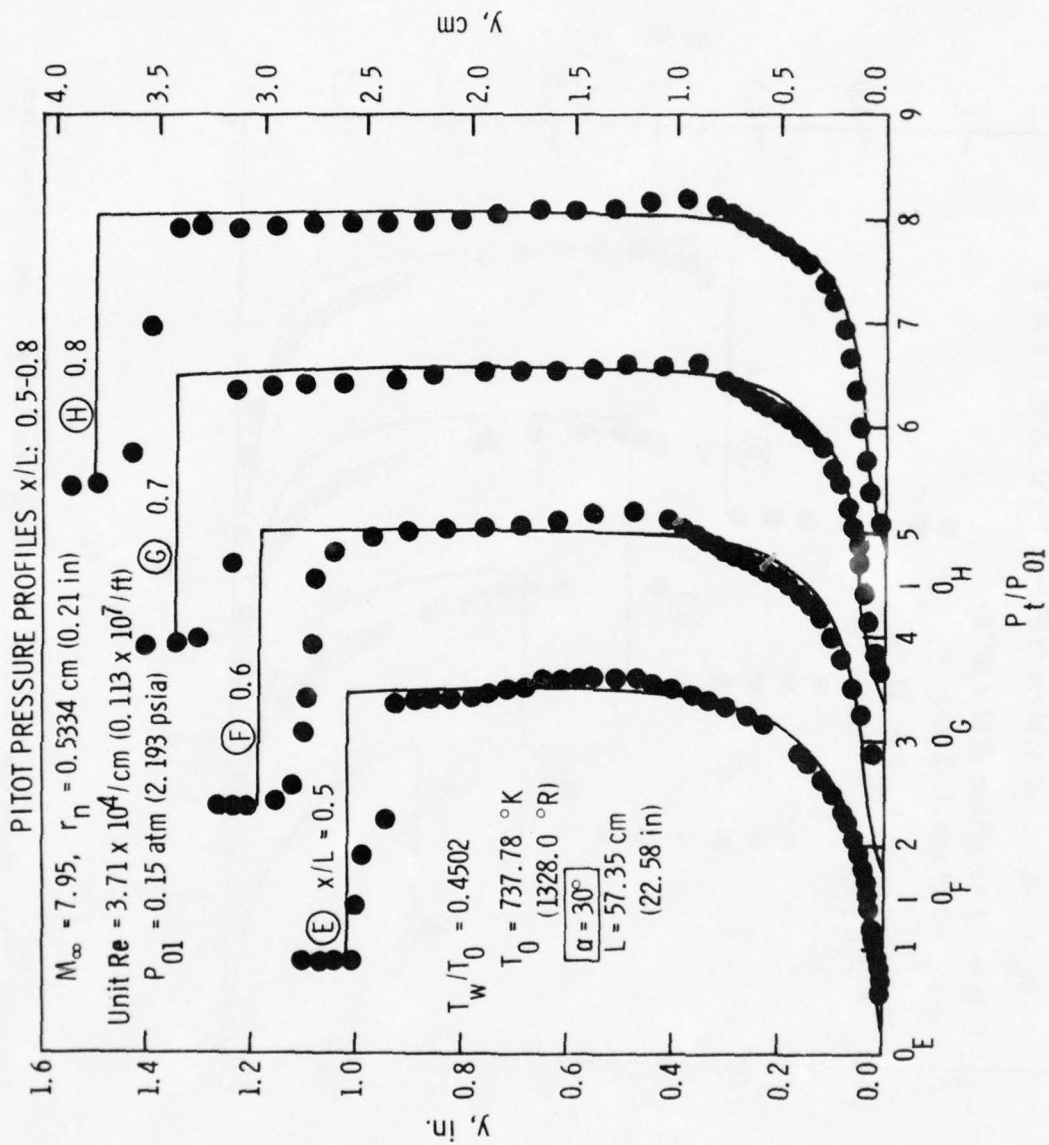
Figure 12: Continued.

44
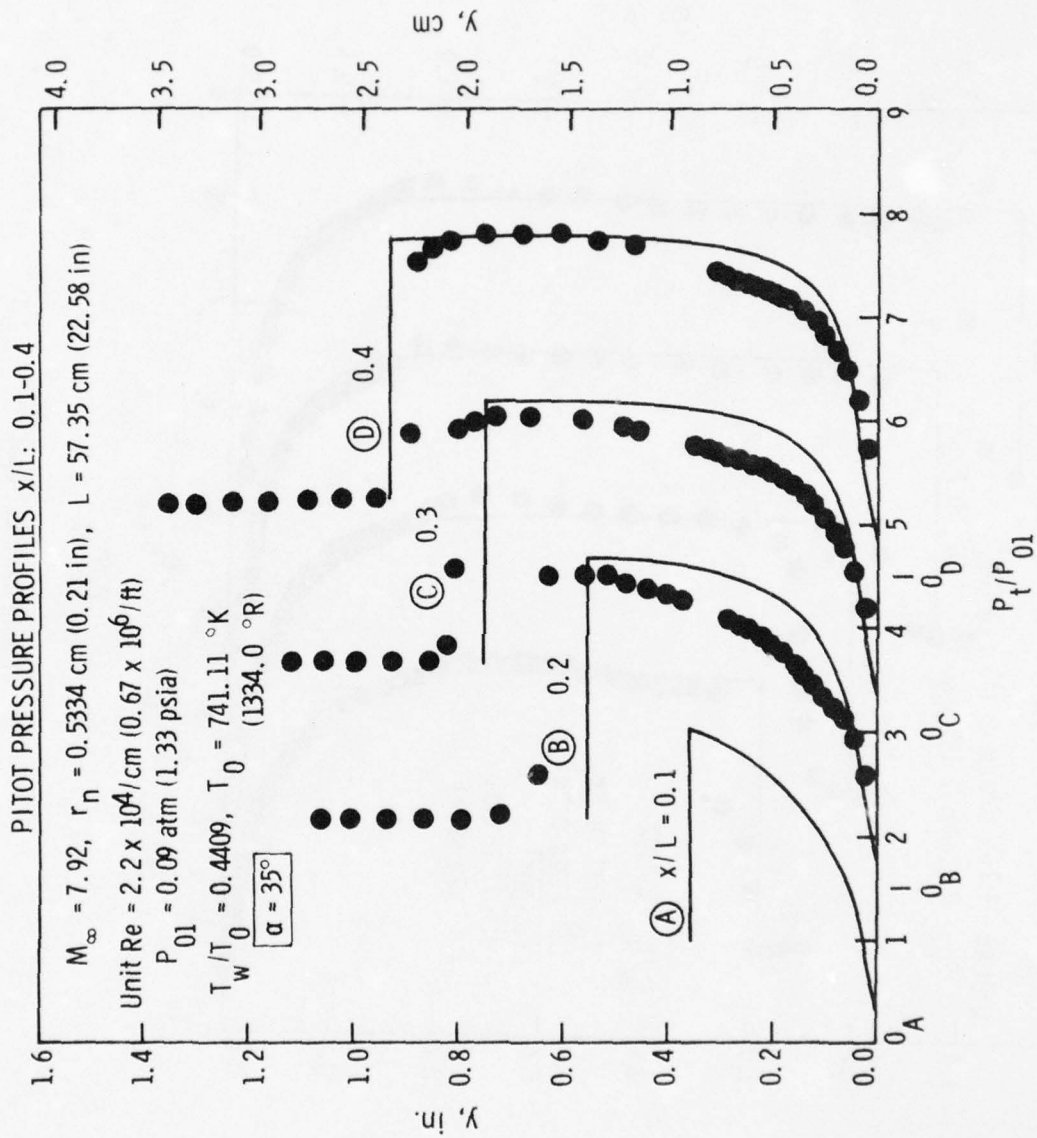
Figure 13: Pitot Pressure Profiles along the Windward Streamline at 35-deg Angle of Attack.

45

PITOT PRESSURE PROFILES x/L: 0.5-0.8

y, cm

y, in.

$M_\infty = 7.92$
$r_n = 0.5334$ cm
      (0.21 in)
Unit Re = 2.2×10^4/cm
      (0.67×10^6/ft)
$P_{01} = 0.09$ atm
      (1.33 psia)
$T_w/T_0 = 0.4409$
$T_0 = 741.11$ °K
      (1334.0 °R)
$\boxed{\alpha = 35^\circ}$
$L = 57.35$ cm
      (22.58 in)

P_t/P_{01}
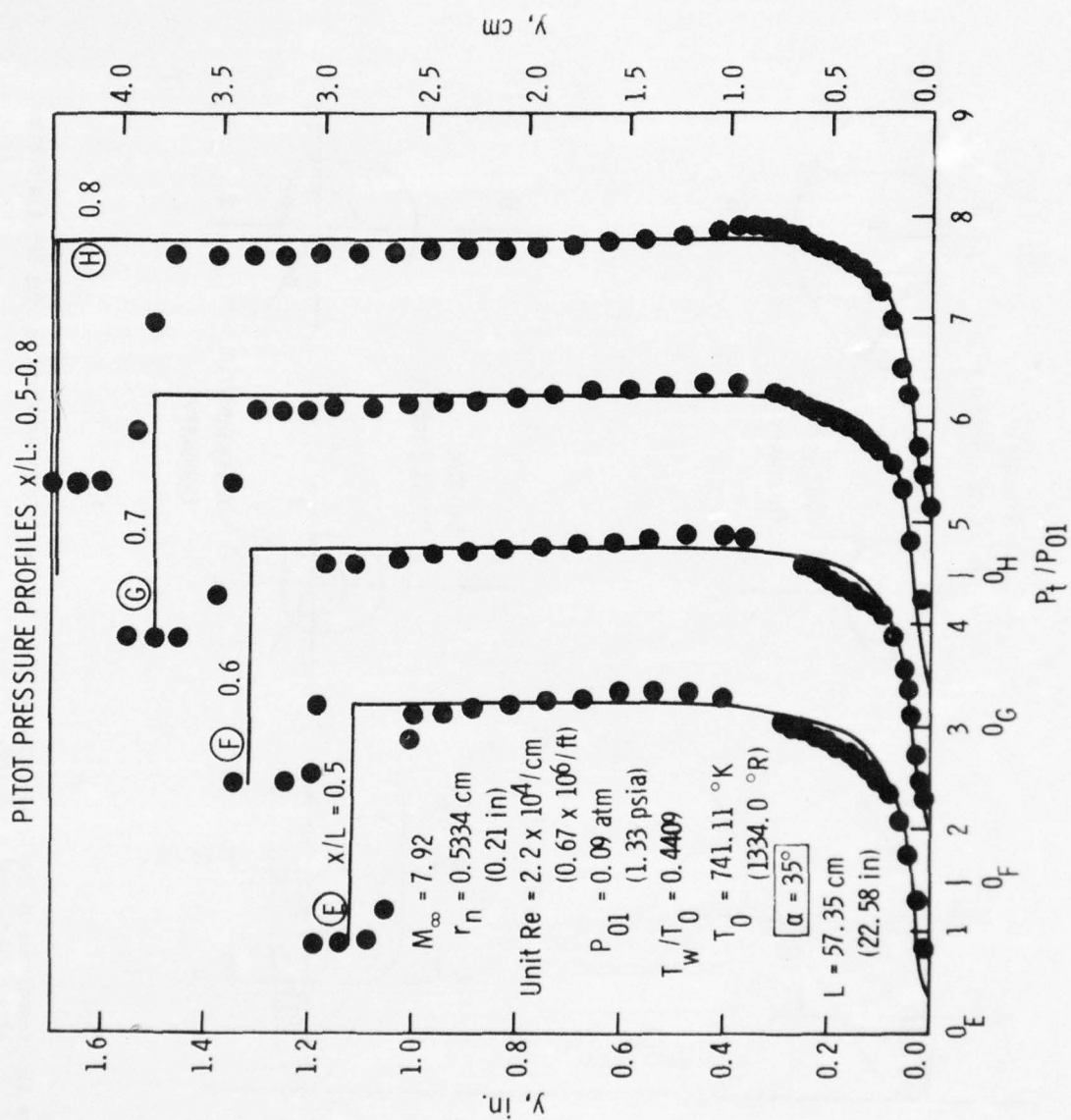
Figure 13: Continued.

46
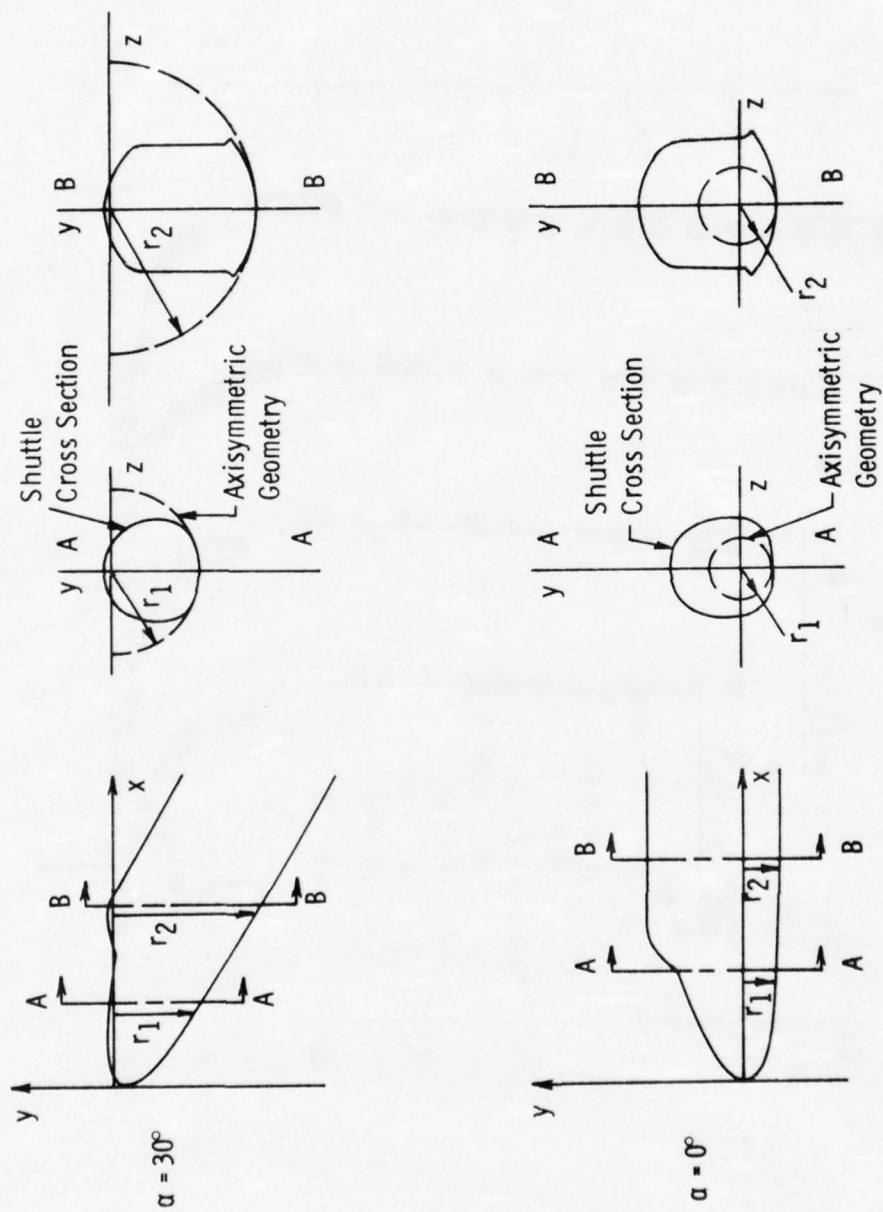
Figure 14: Comparison of the Cross Sections of an Axisymmetric Hyperboloid and the Shuttle Orbiter at α = 30-deg and α = 0-deg.

47
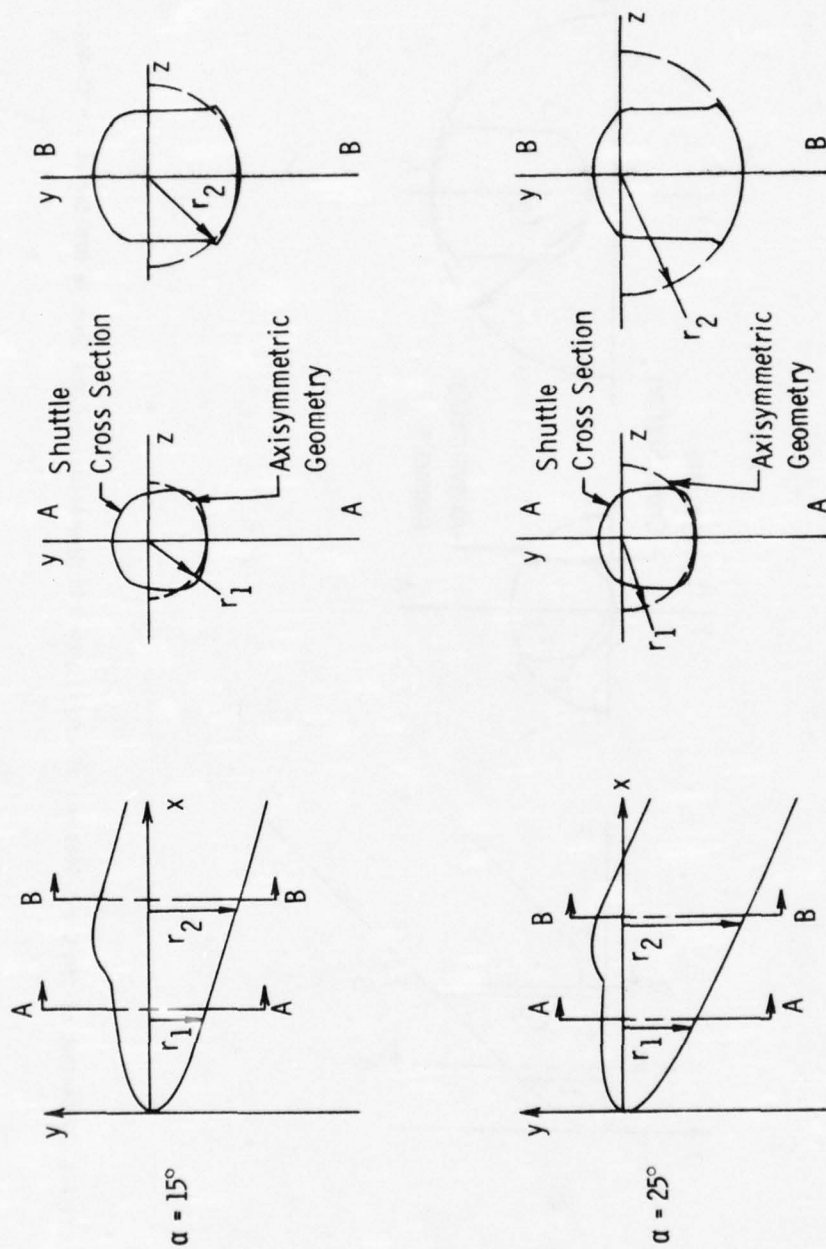
Figure 15: Comparison of the Cross Sections of an Axisymmetric Hyperboloid and the Shuttle Orbiter at α = 15-deg and α = 25-deg.

48
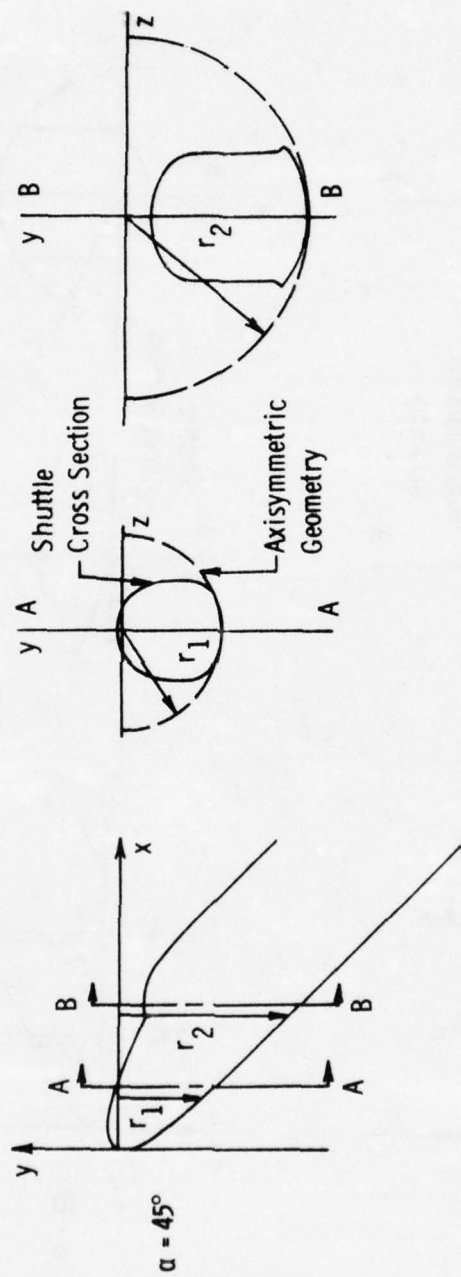
Figure 16: Comparison of the Cross Sections of an Axisymmetric Hyperboloid and the Shuttle Orbiter at α = 45-deg.

49
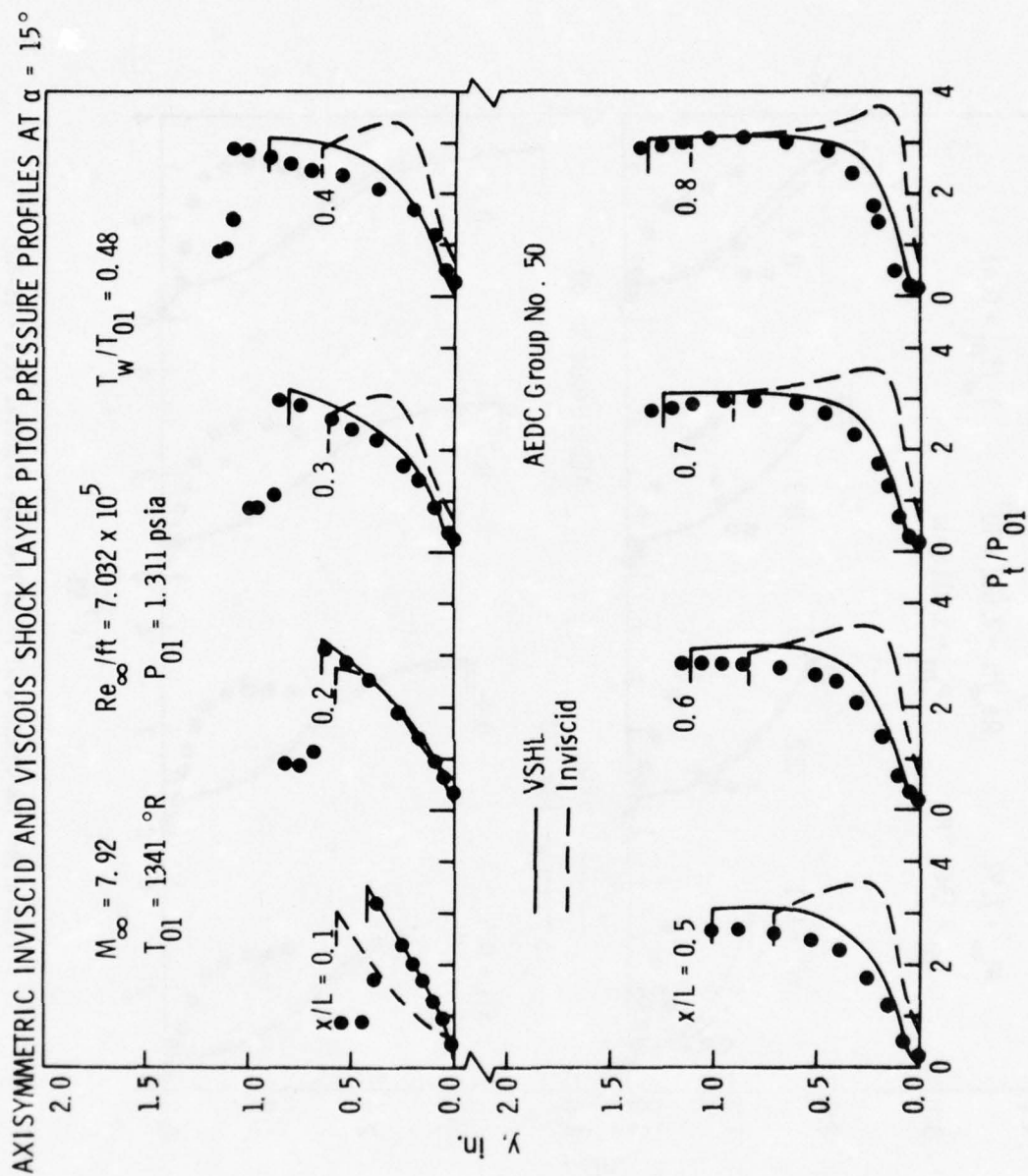
Figure 17: Axisymmetric Pitot Pressure Profiles at α = 15-deg.
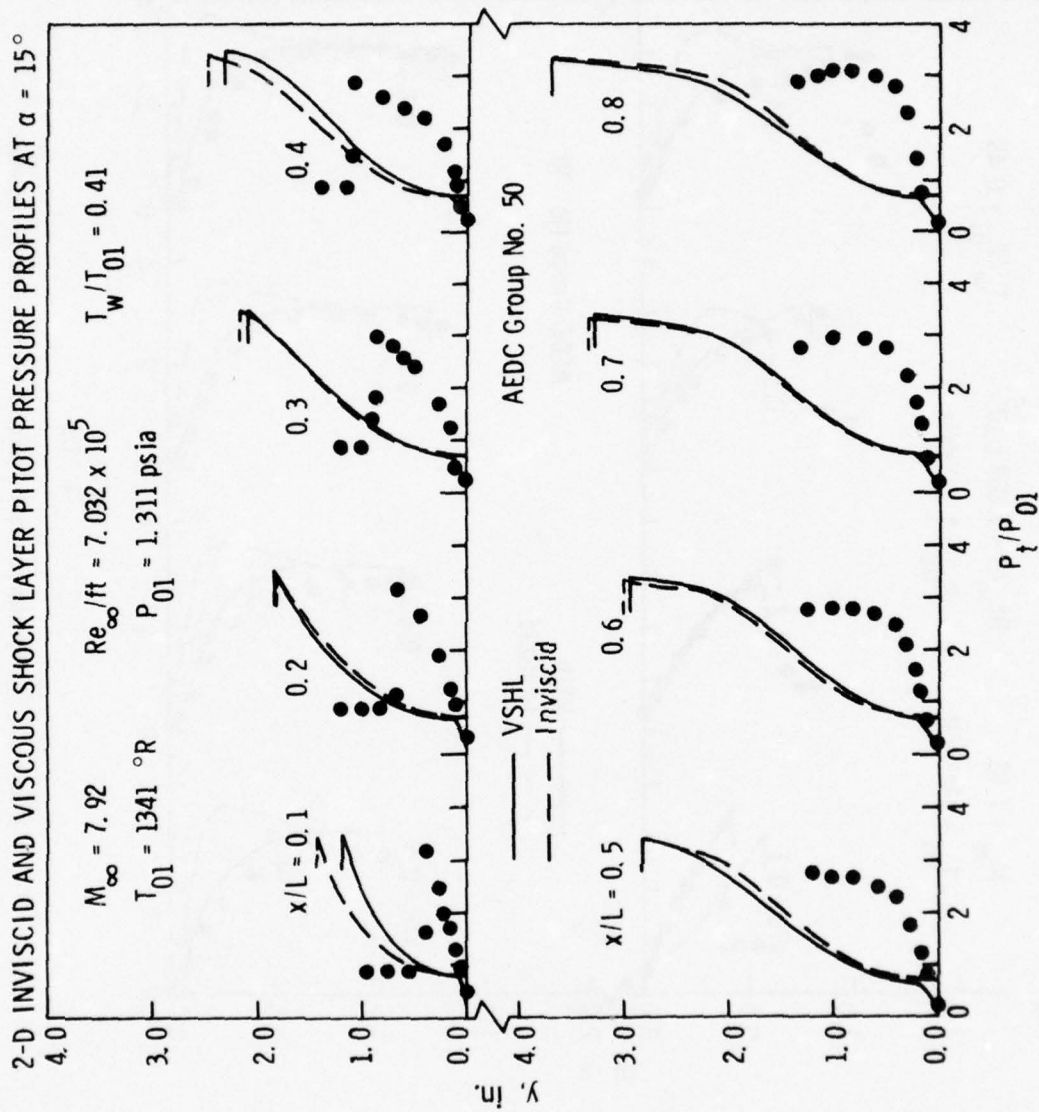
Figure 18: Two-dimensional Pitot Pressure Profiles at α = 15-deg.

51
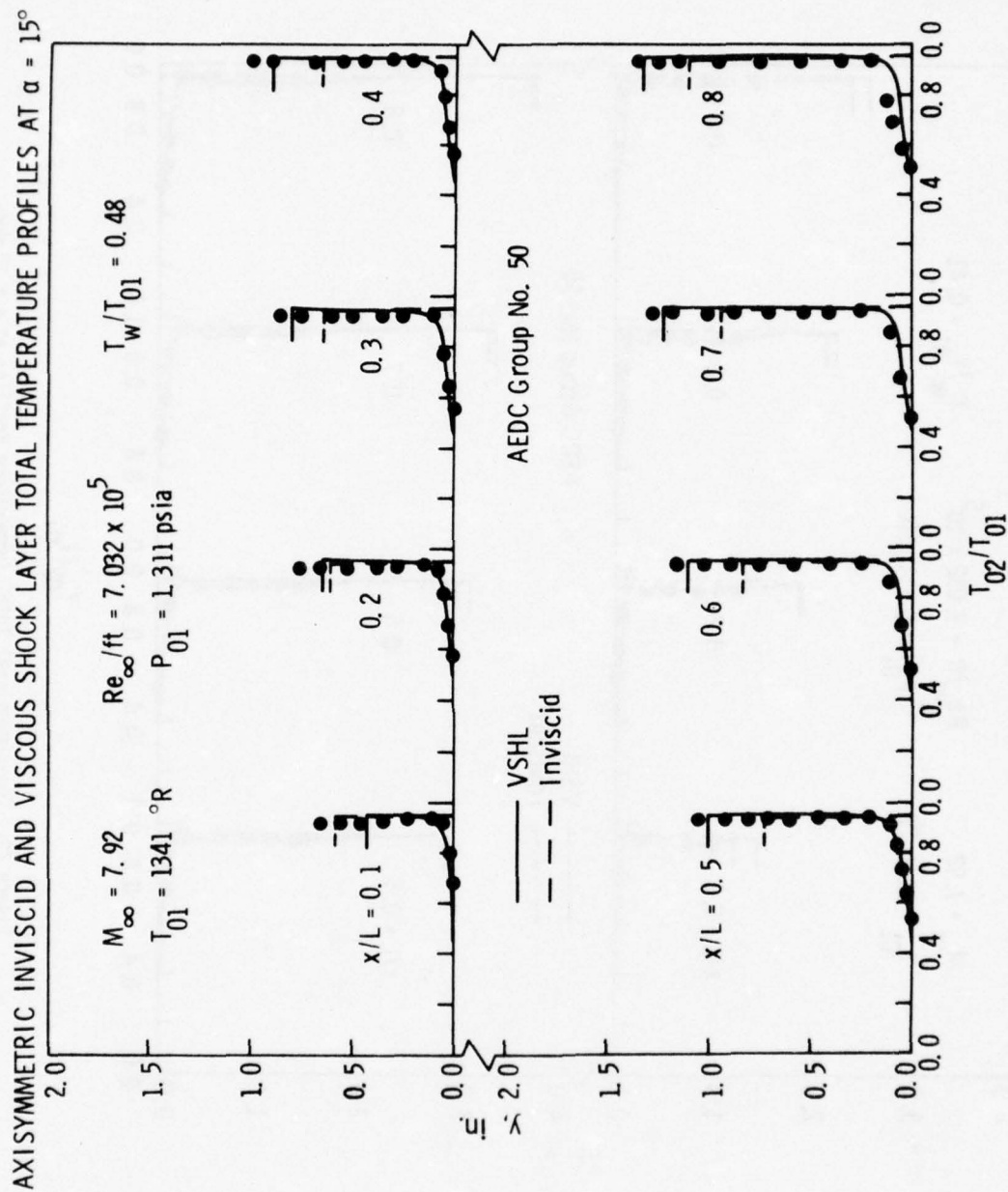
Figure 19: Axisymmetric Total Temperature Profiles at α = 15-deg.

2-D INVISCID AND VISCOUS SHOCK LAYER TOTAL TEMPERATURE PROFILES AT $\alpha = 15°$

$M_\infty = 7.92$ $Re_\infty/ft = 7.032 \times 10^5$ $T_W/T_{01} = 0.41$

$T_{01} = 1341 °R$ $P_{01} = 1.311$ psia

—— VSHL
– – – Inviscid

AEDC Group No. 50
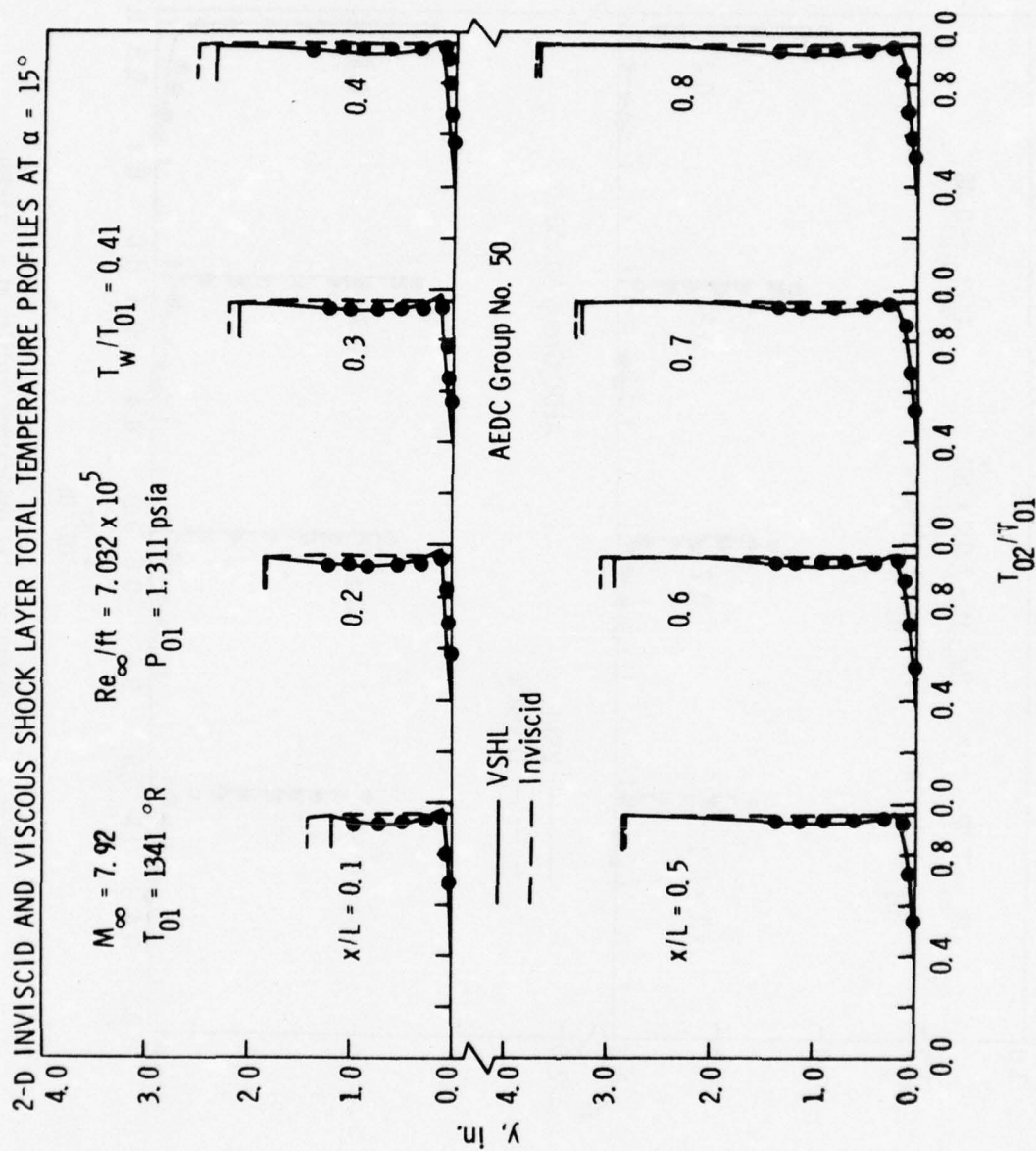
Figure 20: Two-dimensional Total Temperature Profiles at $\alpha = 15$-deg.

53
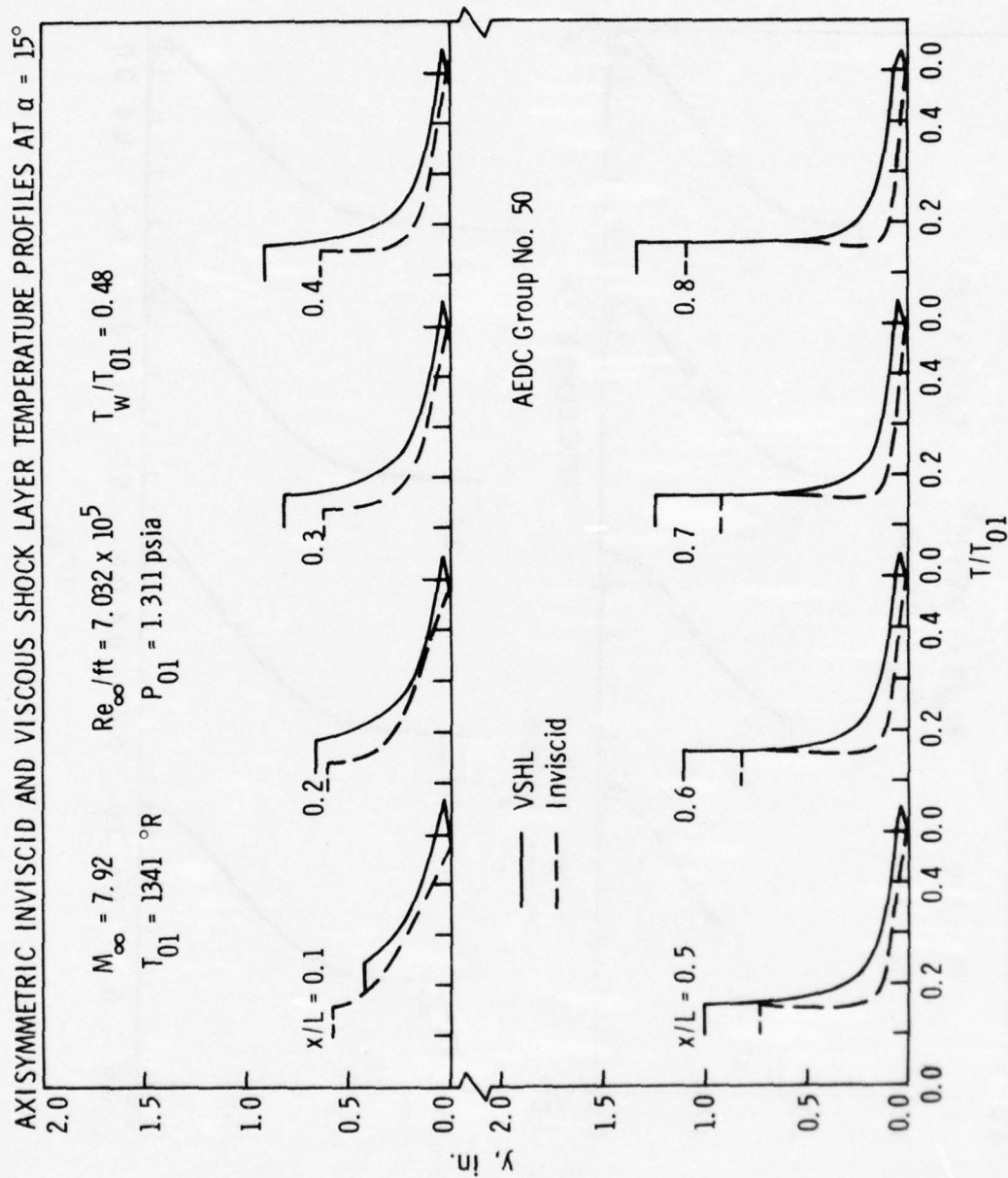
Figure 21: Axisymmetric Static Temperature Profiles at α = 15-deg.
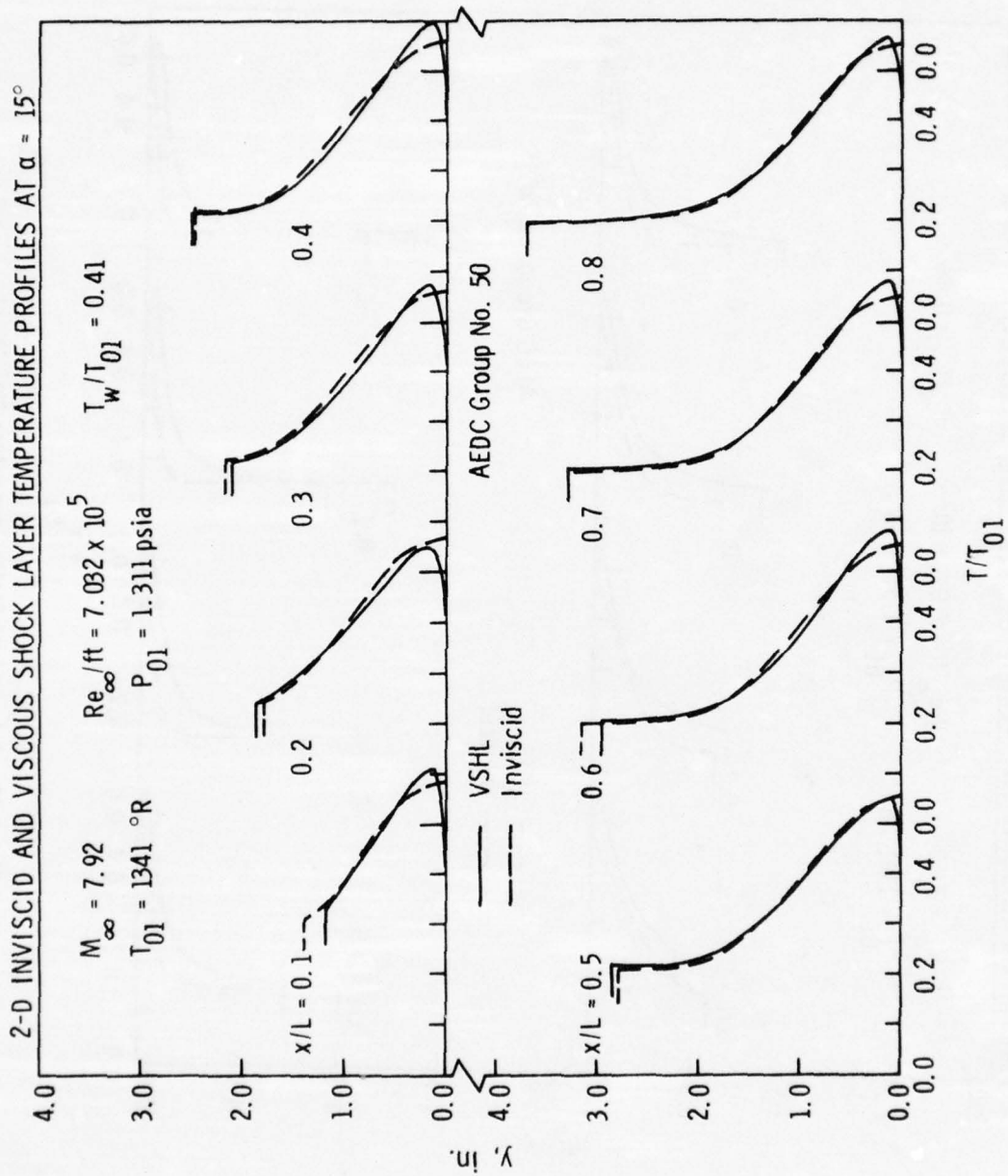
Figure 22: Two-dimensional Static Temperature Profiles at α = 15-deg.

Figure 23: Axisymmetric Tangential Velocity Profiles at α = 15-deg.

2-D INVISCID AND VISCOUS SHOCK LAYER TANGENTIAL VELOCITY PROFILES AT $\alpha = 15°$

$M_\infty = 7.92$ $Re_\infty/ft = 7.032 \times 10^5$ $T_W/T_{01} = 0.41$

$T_{01} = 1341 °R$ $P_{01} = 1.311 psia$ $U_\infty = 3862 ft/sec$

VSHL

Inviscid

AEDC Group No. 50

x/L = 0.1   0.2   0.3   0.4

x/L = 0.5   0.6   0.7   0.8

y, in.

U/U_∞
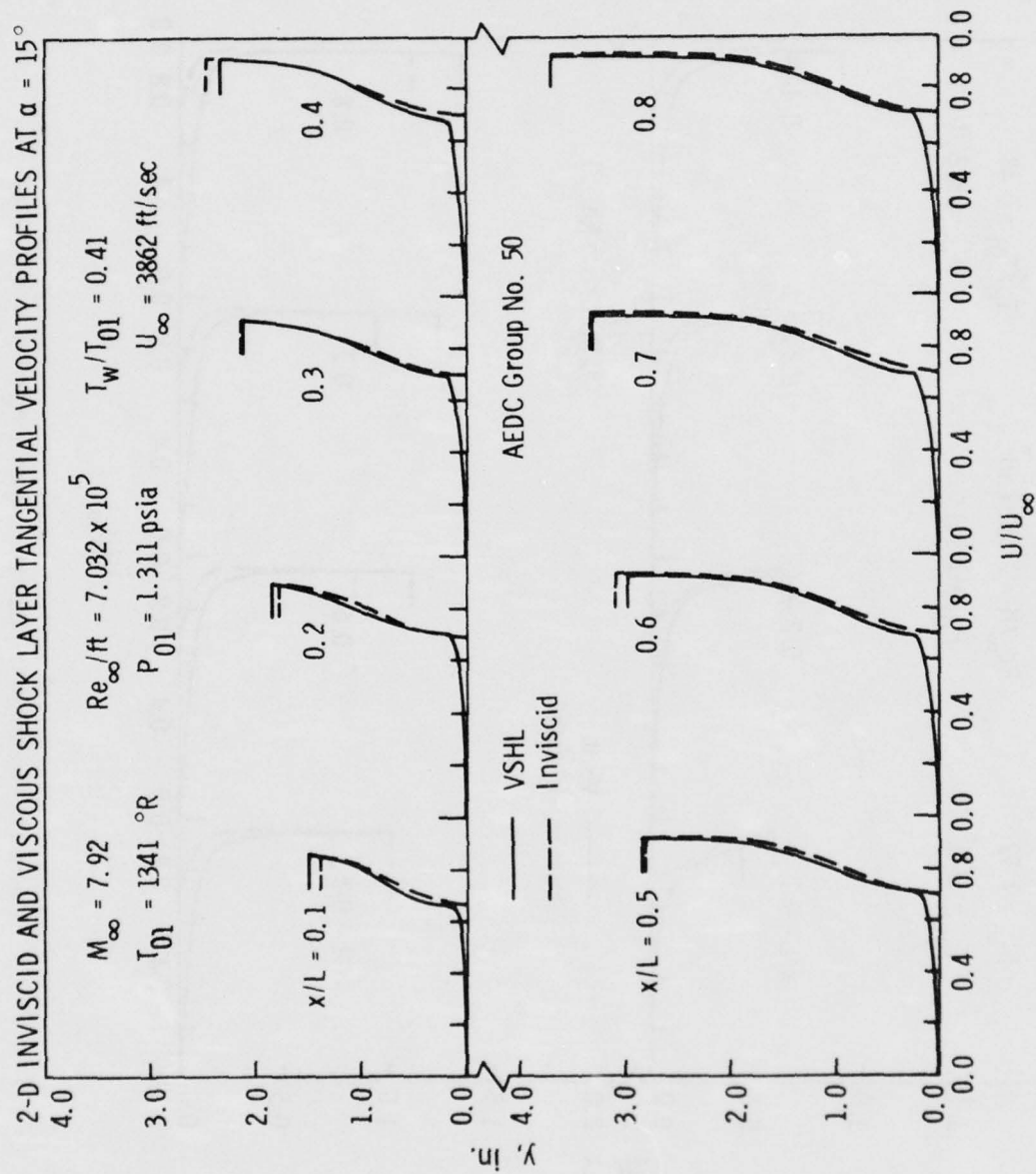
Figure 24: Two-dimensional Tangential Velocity Profiles at α = 15-deg.
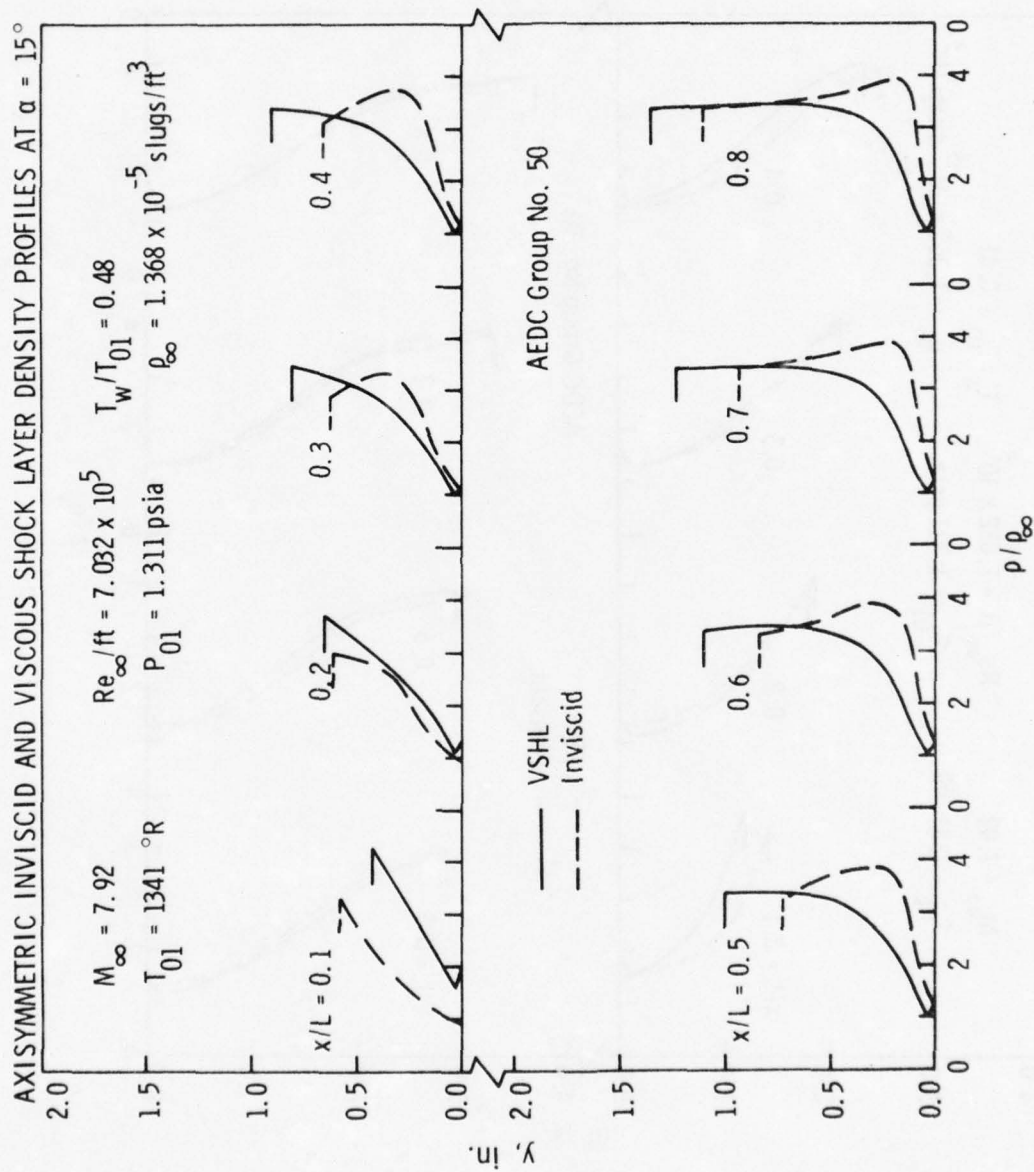
Figure 25: Axisymmetric Density Profiles at α = 15-deg.

58
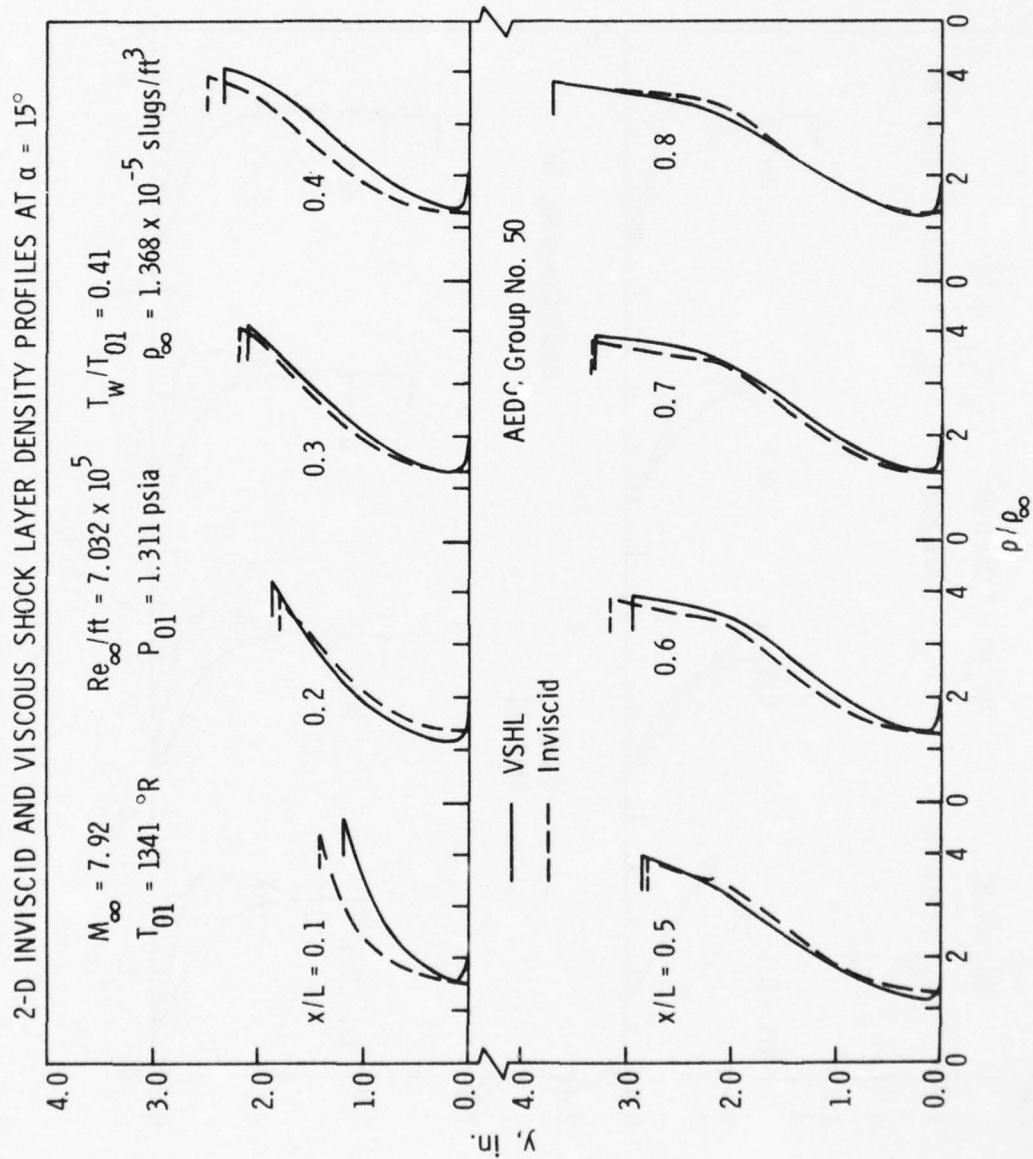
Figure 26: Two-dimensional Density Profiles at α = 15-deg.
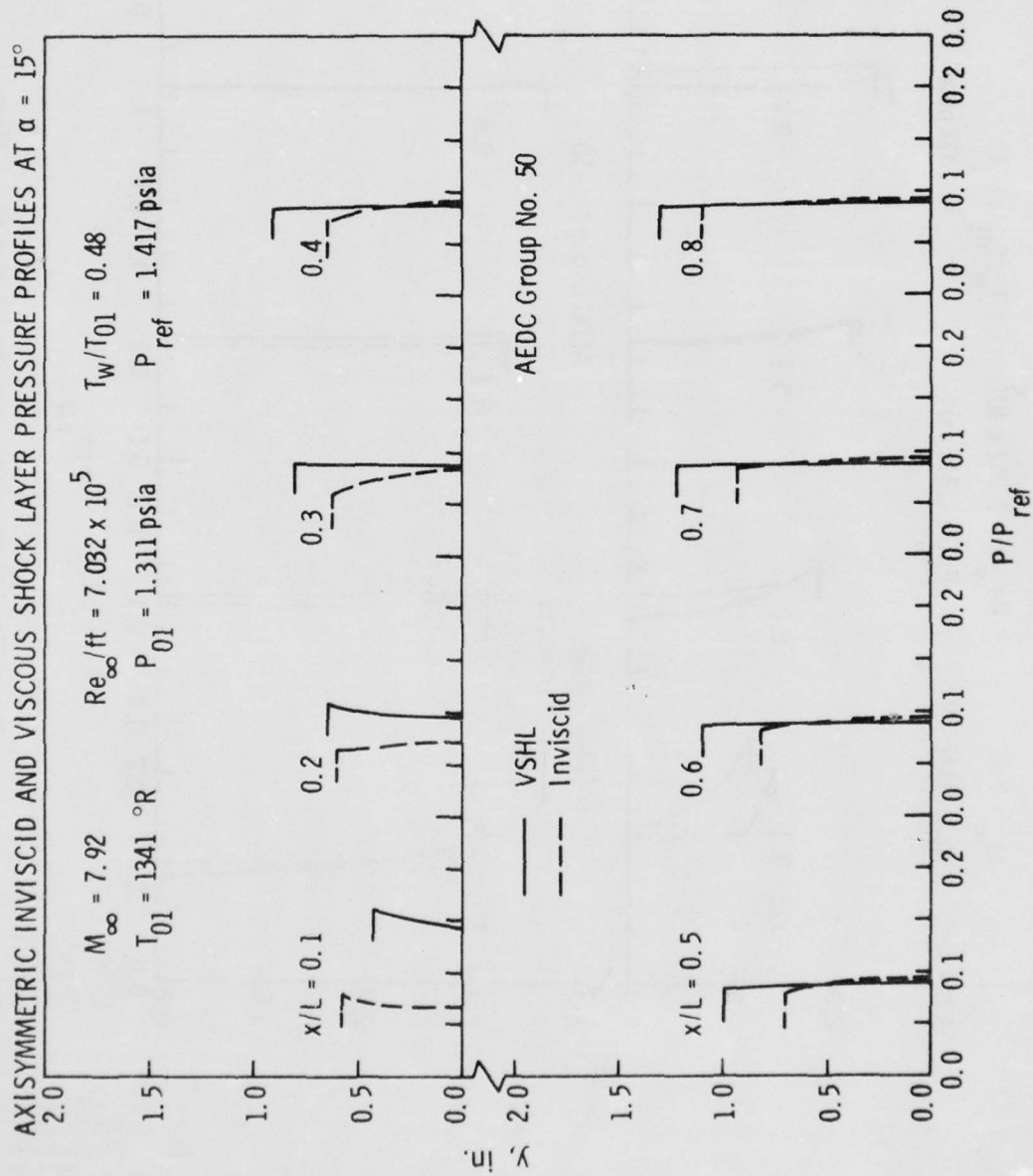
Figure 27: Axisymmetric Pressure Profiles at α = 15 deg.

2-D INVISCID AND VISCOUS SHOCK LAYER PRESSURE PROFILES AT $\alpha = 15°$

$M_\infty = 7.92$ $Re_\infty/ft = 7.032 \times 10^5$ $T_w/T_{01} = 0.41$

$T_{01} = 1341 °R$ $P_{01} = 1.311 psia$ $P_{ref} = 1.417 psia$

AEDC Group No. 50

VSHL ⎯⎯⎯
Inviscid - - - -

$x/L = 0.1$ 0.2   0.3   0.4

$x/L = 0.5$ 0.6   0.7   0.8

y, in.

P/P_{ref}
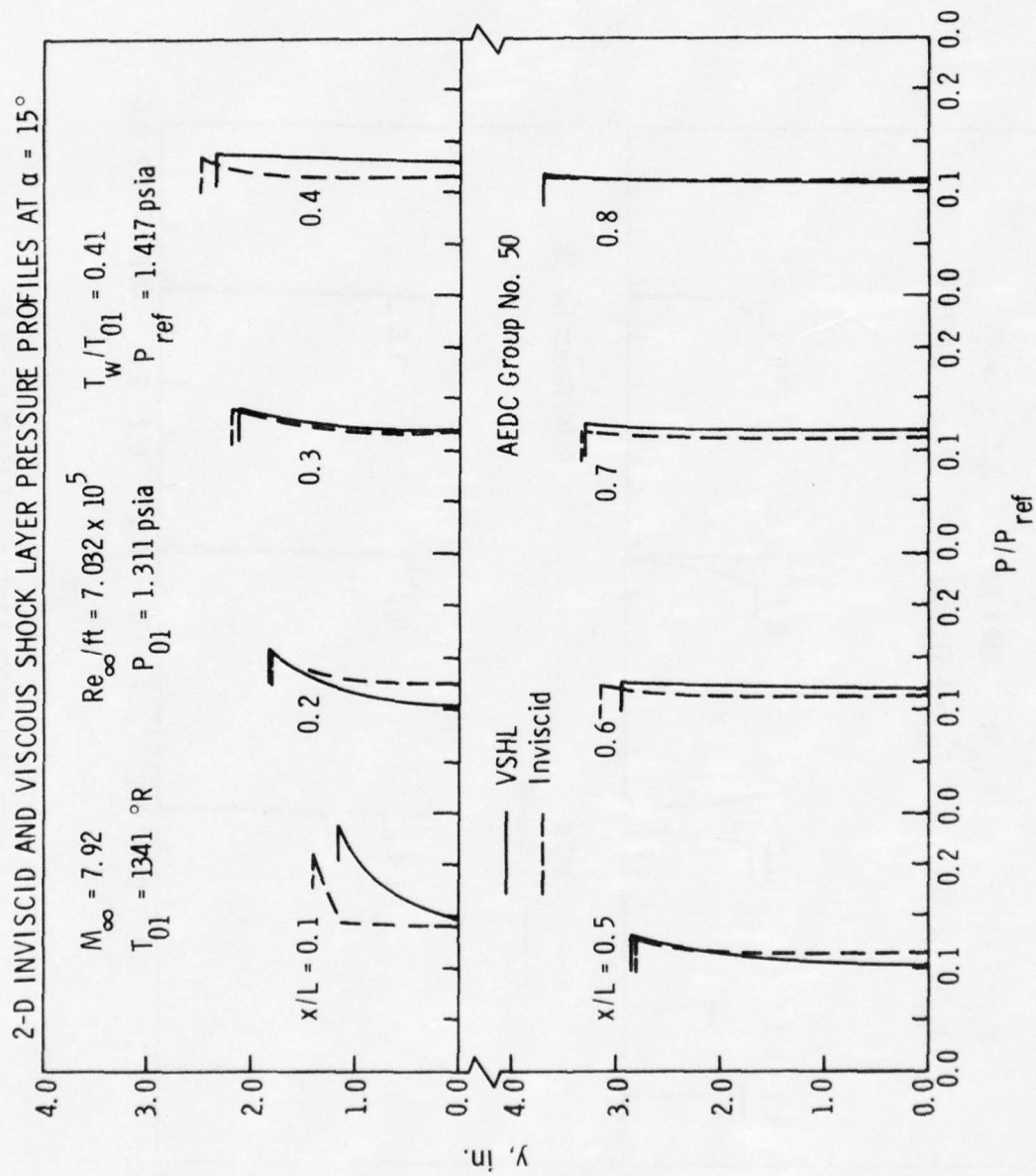
Figure 28: Two-dimensional Pressure Profiles at α = 15-deg.

61
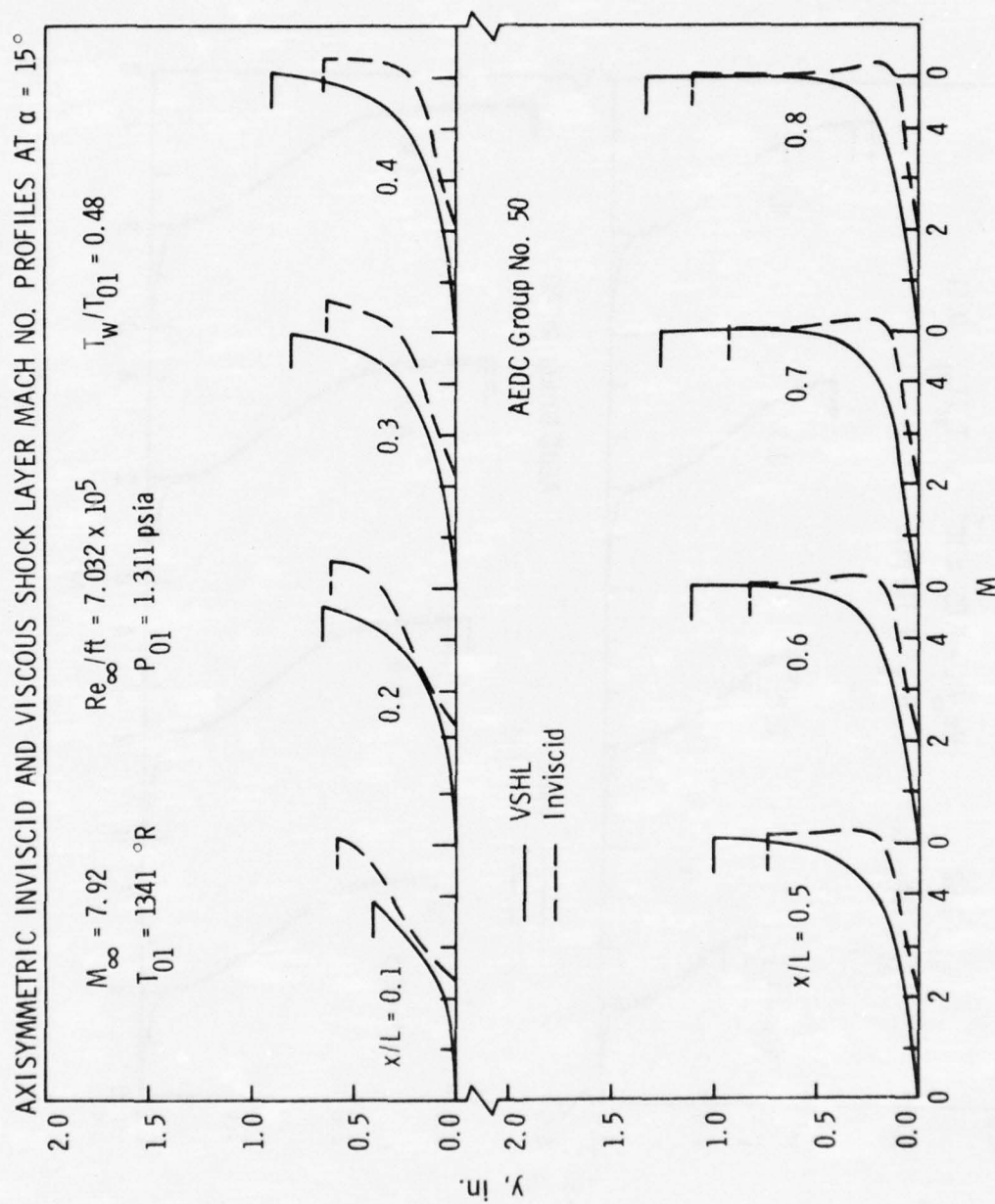
Figure 29: Axisymmetric Mach Number Profiles at α = 15-deg.

62
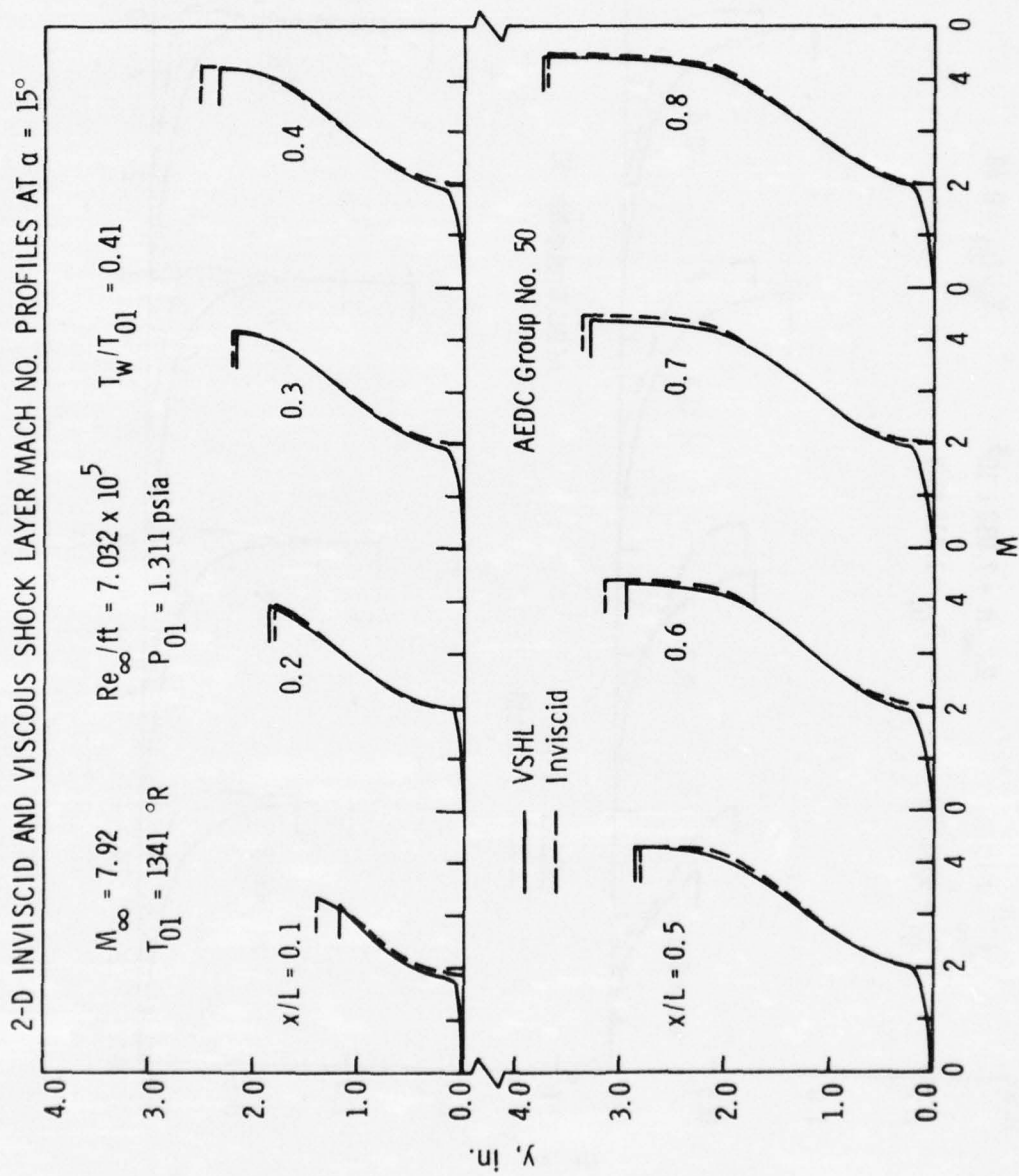
Figure 30: Two-dimensional Mach Number Profiles at α = 15-deg.

AXISYMMETRIC INVISCID AND VISCOUS SHOCK LAYER PITOT PRESSURE PROFILES AT $\alpha = 30°$
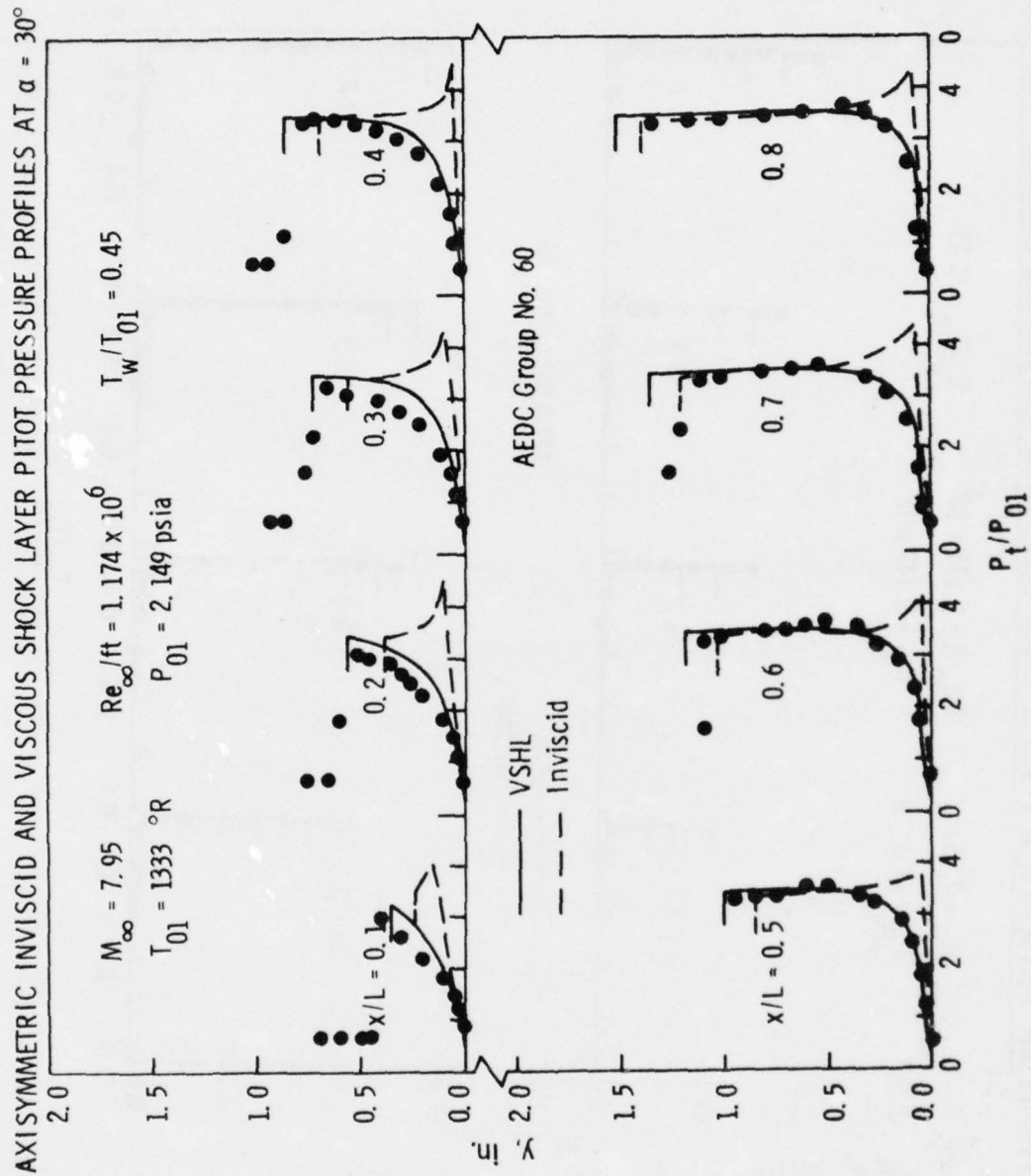
Figure 31: Pitot Pressure Profiles from an Axisymmetric Solution at α = 30-deg.
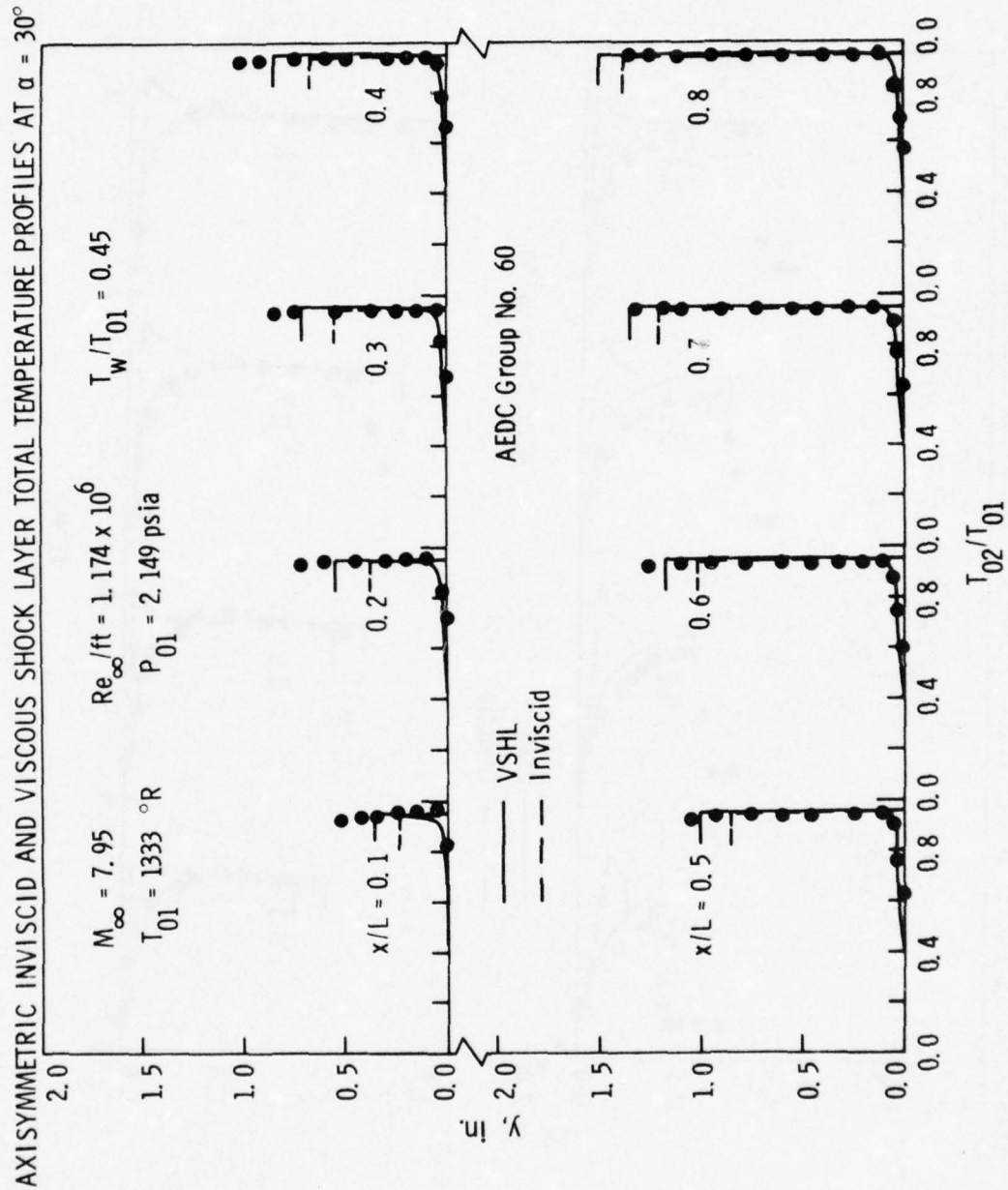
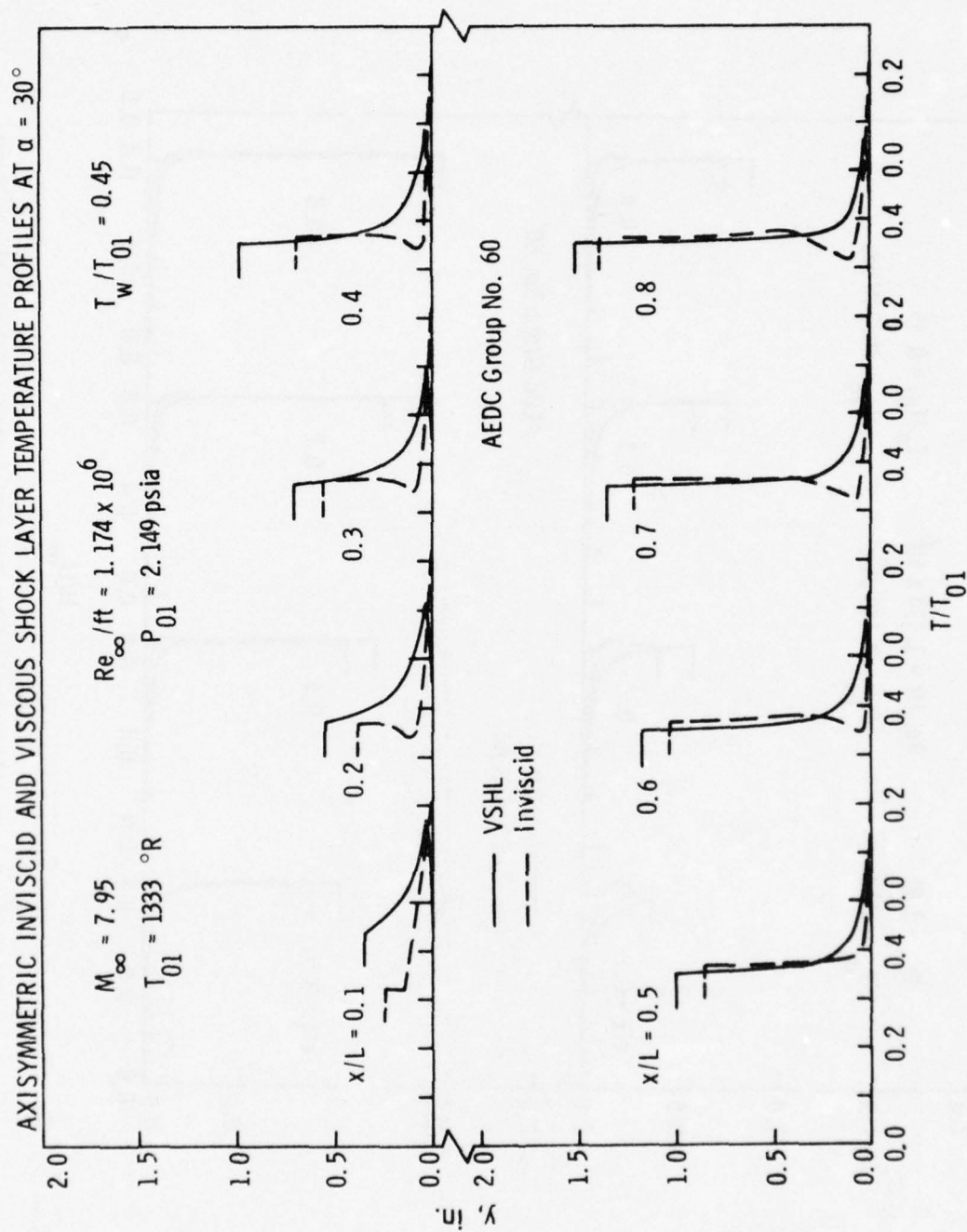Figure 32: Total Temperature Profiles from an Axisymmetric Solution at α = 30-deg.

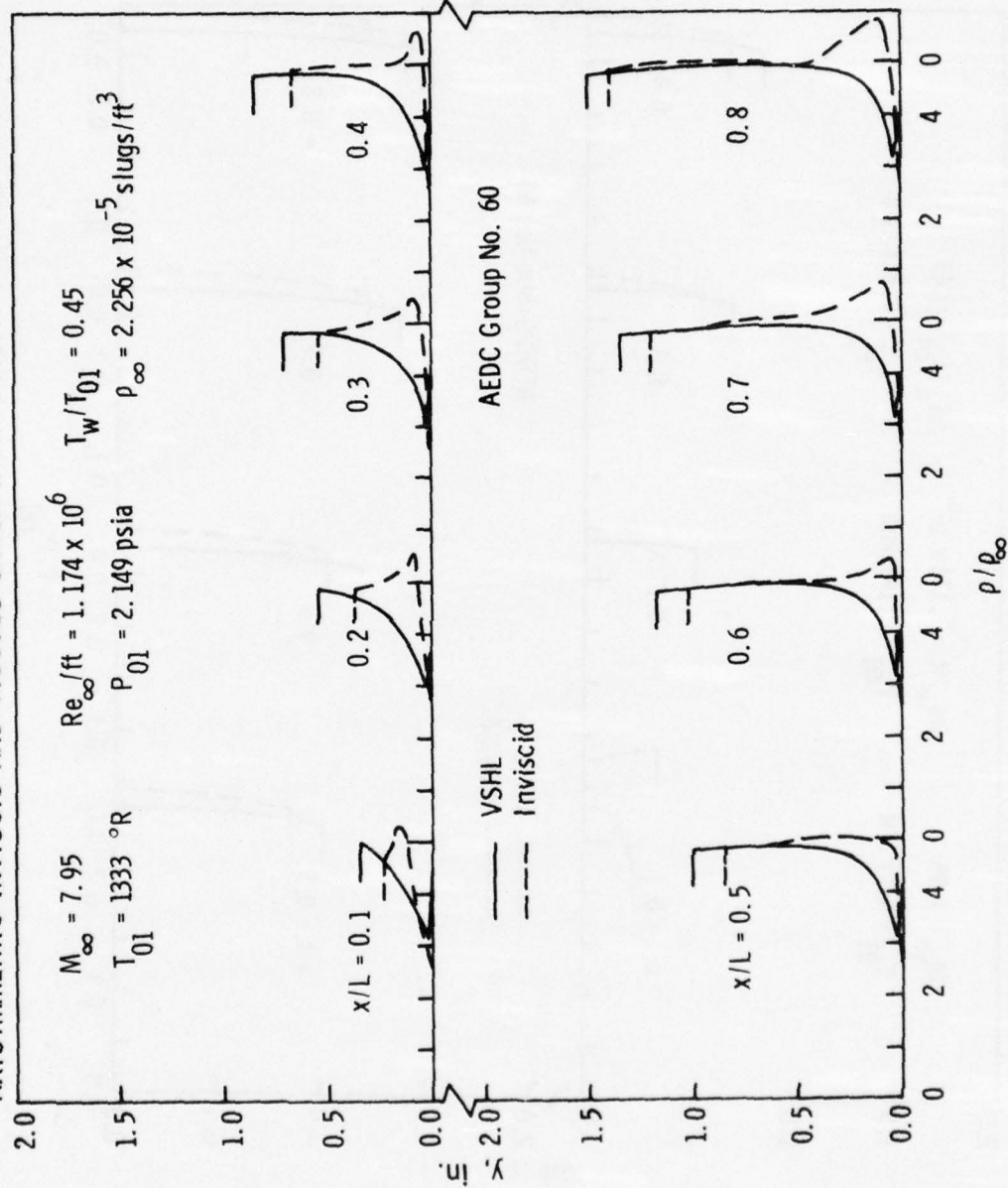AXISYMMETRIC INVISCID AND VISCOUS SHOCK LAYER TEMPERATURE PROFILES AT $\alpha = 30°$

$M_\infty = 7.95$ $Re_\infty/ft = 1.174 \times 10^6$ $T_W/T_{01} = 0.45$

$T_{01} = 1333 °R$ $P_{01} = 2.149$ psia

VSHL

Inviscid

AEDC Group No. 60

x/L = 0.1   0.2   0.3   0.4

x/L = 0.5   0.6   0.7   0.8

y, in.

T/T_{01}

Figure 33: Temperature Profiles from an Axisymmetric Solution at α = 30-deg.

Figure 34: Tangential Velocity Profiles from an Axisymmetric Solution at α = 30-deg.

AXISYMMETRIC INVISCID AND VISCOUS SHOCK LAYER DENSITY PROFILES AT $\alpha = 30°$

$M_\infty = 7.95$ $Re_\infty/ft = 1.174 \times 10^6$ $T_w/T_{01} = 0.45$

$T_{01} = 1333°R$ $P_{01} = 2.149$ psia $\rho_\infty = 2.256 \times 10^{-5}$ slugs/ft^3

AEDC Group No. 60

VSHL
Inviscid

$x/L = 0.1$ 0.2 0.3 0.4

$x/L = 0.5$ 0.6 0.7 0.8

y, in.

ρ/ρ_∞

Figure 35: Density Profiles from an Axisymmetric Solution at α = 30-deg.
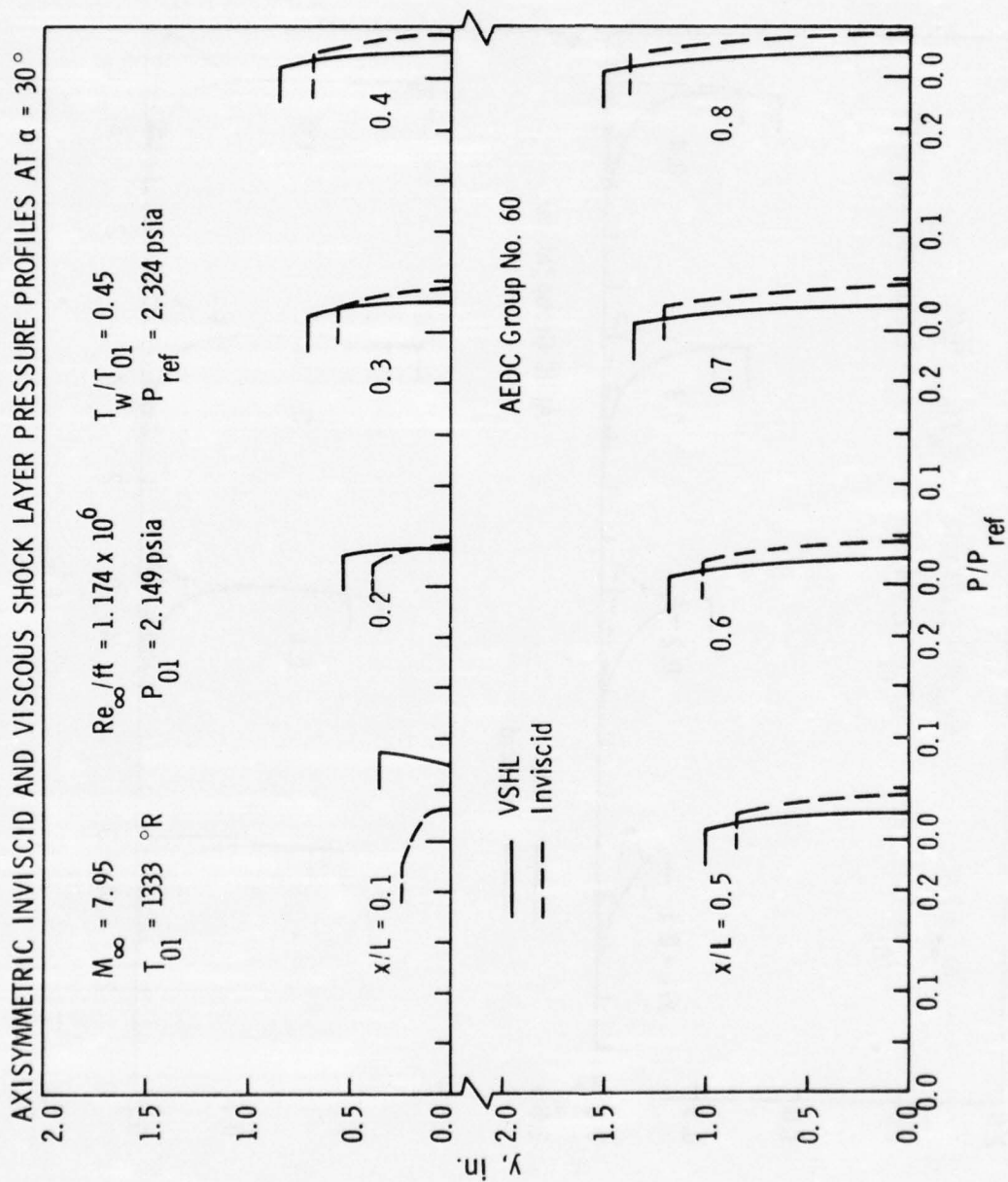
Figure 36: Pressure Profiles from an Axisymmetric Solution at α = 30-deg.
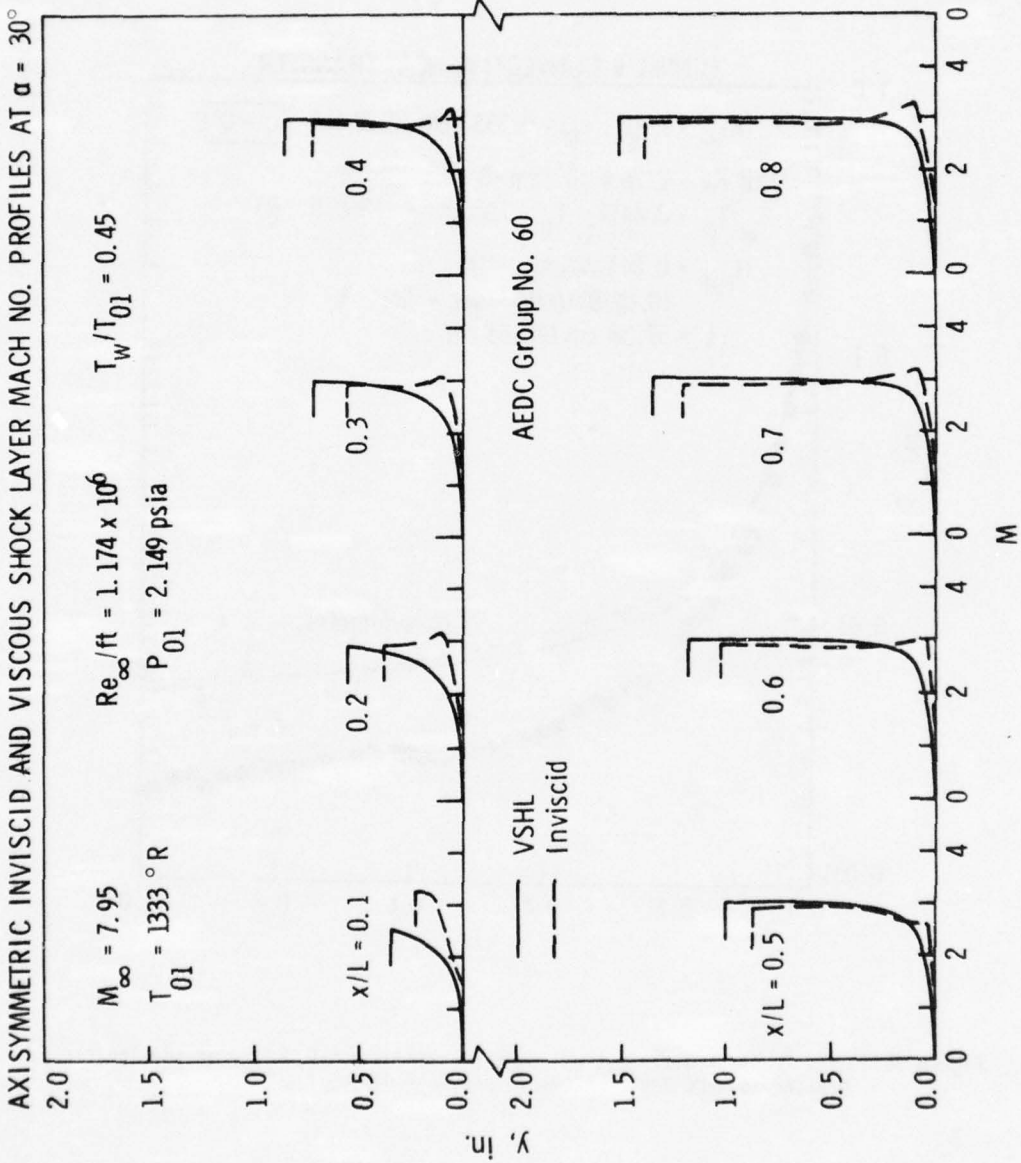
Figure 37: Mach Number Profiles from an Axisymmetric Solution at α = 30-deg.

TUNNEL B CONVECTIVE HEAT TRANSFER
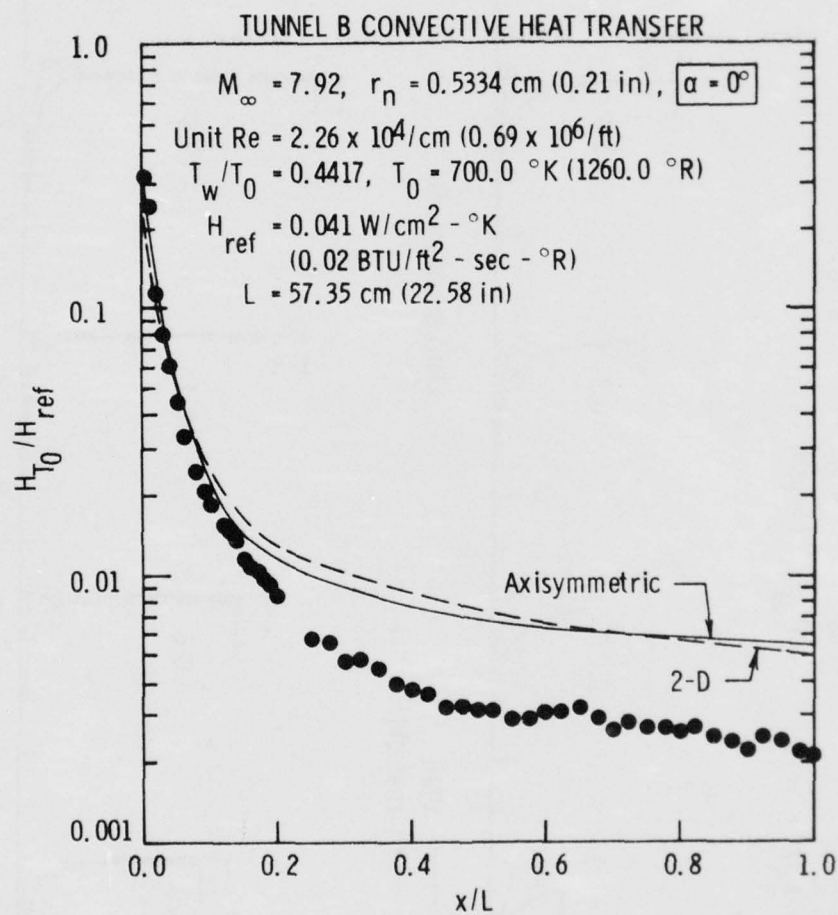
$M_\infty = 7.92$, $r_n = 0.5334$ cm (0.21 in), $\boxed{\alpha = 0°}$

Unit Re $= 2.26 \times 10^4$/cm (0.69×10^6/ft)

$T_w/T_0 = 0.4417$, $T_0 = 700.0$ °K (1260.0 °R)

$H_{ref} = 0.041$ W/cm^2 - °K
(0.02 BTU/ft^2 - sec - °R)

$L = 57.35$ cm (22.58 in)

Axisymmetric

2-D

Figure 38: Heat Transfer Distribution along the Windward Streamline of the Shuttle
Orbiter at AEDC Tunnel B Conditions, $\alpha = 0$-deg.

71
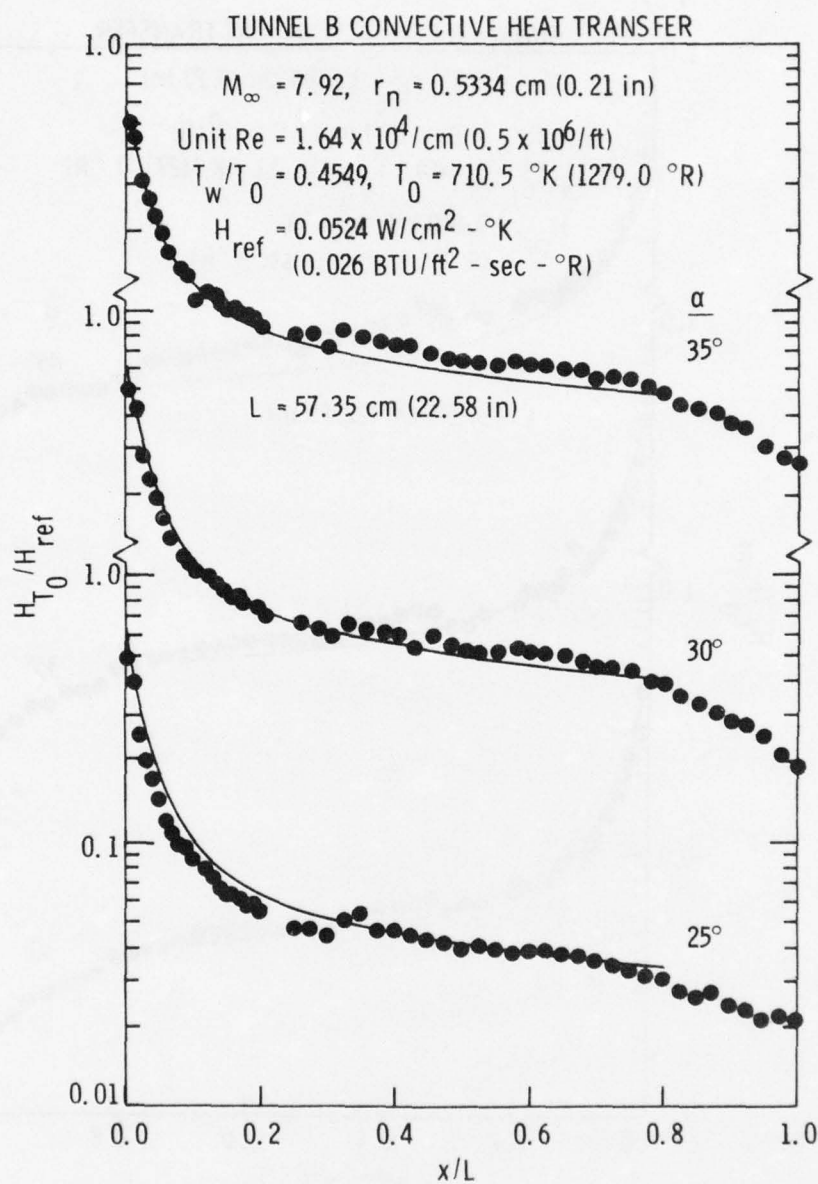
Figure 39: Heat-Transfer Distributions along the Windward Streamline,
Re/cm = 1.64 x 10^4.

72
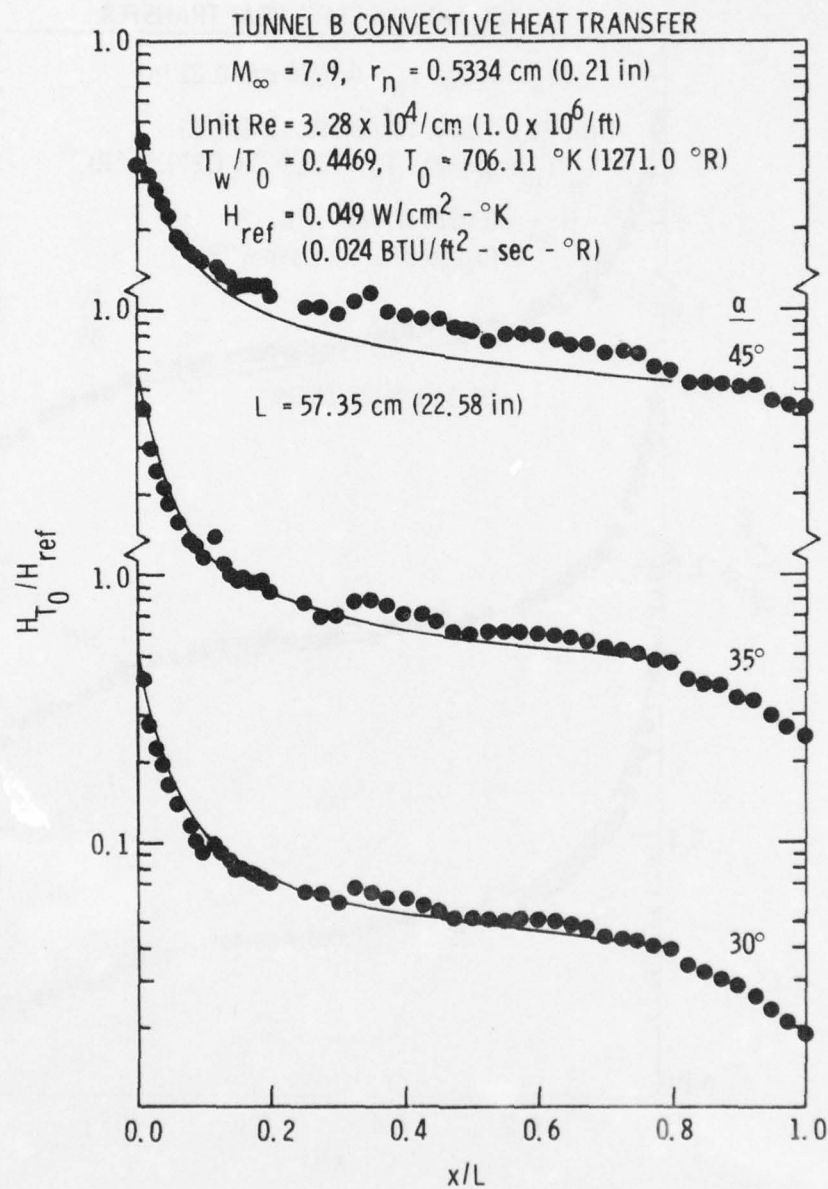
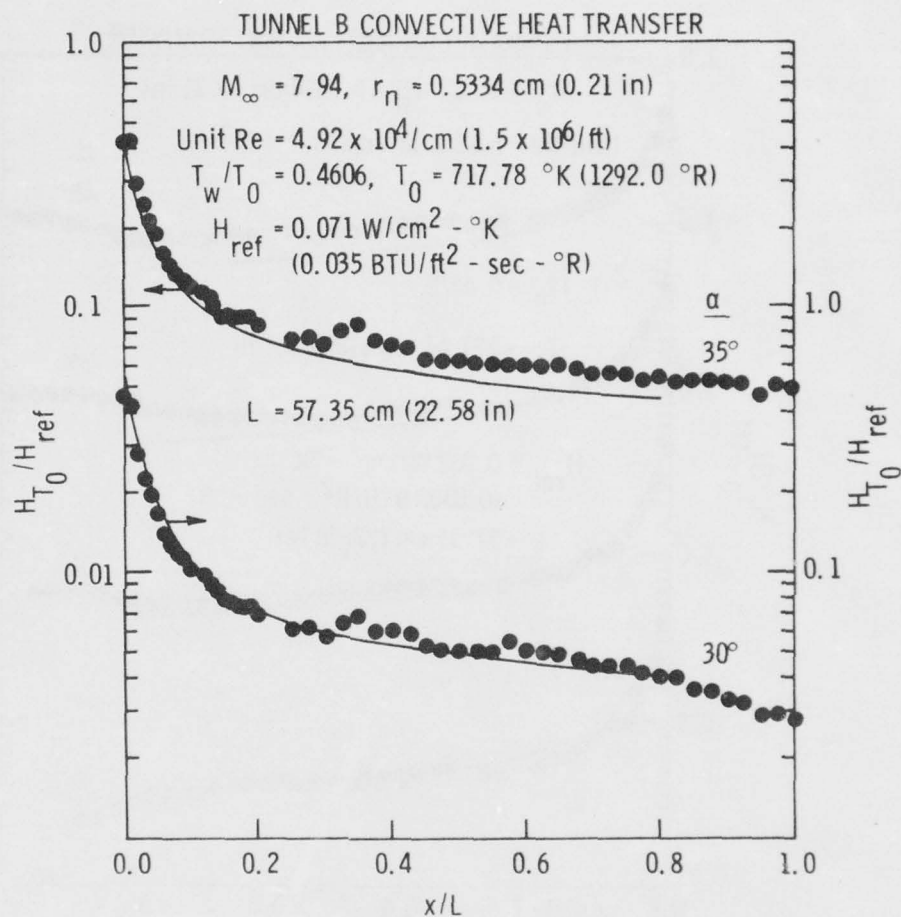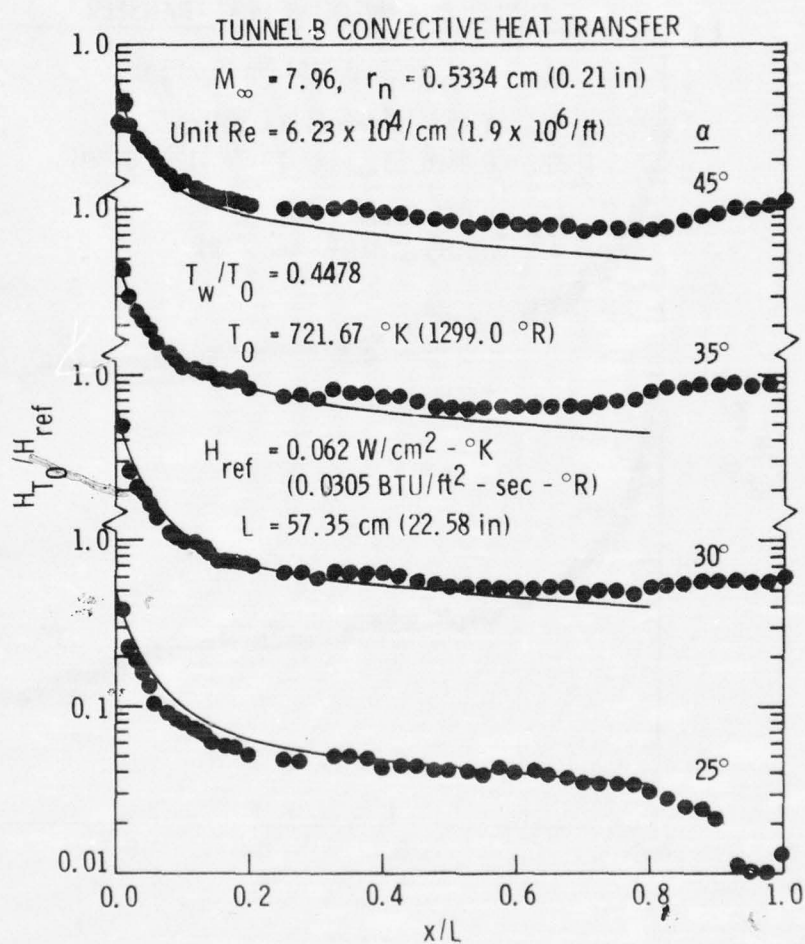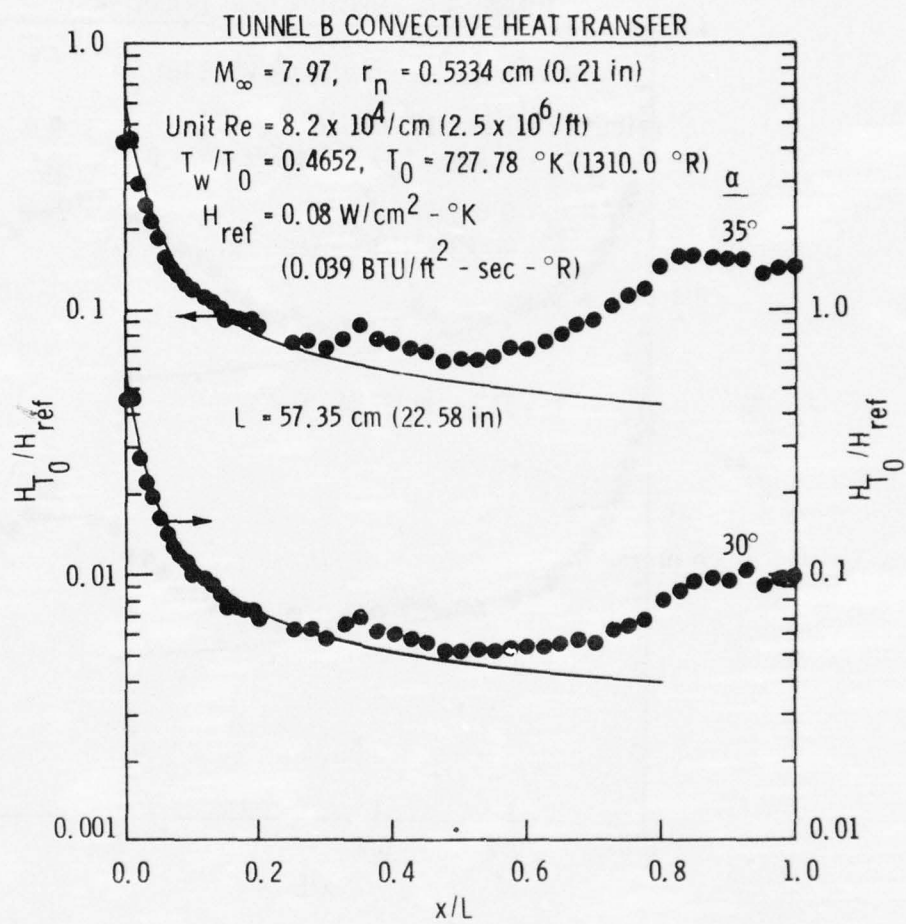Figure 40: Heat-Transfer Distributions along the Windward Streamline, Re/cm = 3.28 x 10^4.

73

TUNNEL B CONVECTIVE HEAT TRANSFER

$M_\infty = 7.94$, $r_n = 0.5334$ cm (0.21 in)

Unit Re = 4.92×10^4/cm (1.5×10^6/ft)

$T_w/T_0 = 0.4606$, $T_0 = 717.78$ °K (1292.0 °R)

$H_{ref} = 0.071$ W/cm^2 - °K

(0.035 BTU/ft^2 - sec - °R)

α

35°

L = 57.35 cm (22.58 in)
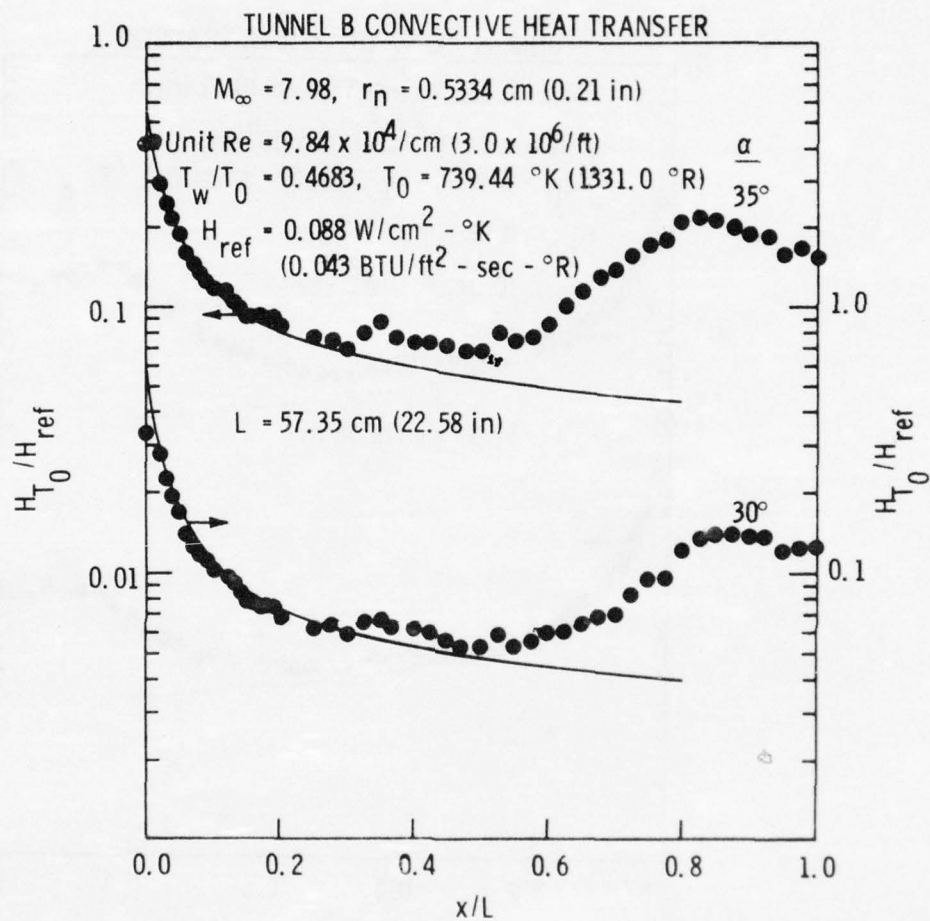
30°

H_{T_0}/H_{ref}

H_{T_0}/H_{ref}

x/L

Figure 41: Heat-Transfer Distributions along the Windward Streamline,
Re/cm = 4.92×10^4.

Figure 42: Heat-Transfer Distributions along the Windward Streamline, Re/cm = 6.23 x 10^4.

Figure 43: Heat-Transfer Distributions along the Windward Streamline, Re/cm = 8.2 x 10⁴.

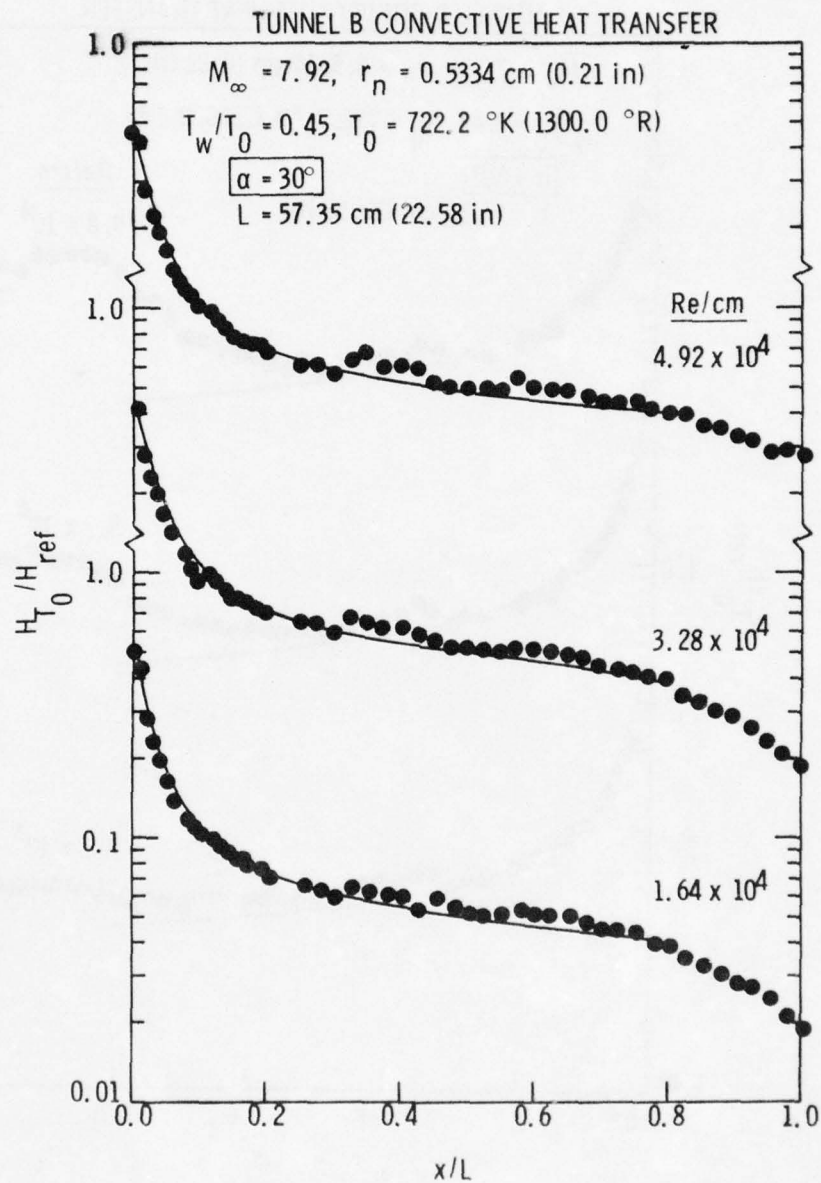Figure 44: Heat-Transfer Distributions along the Windward Streamline, Re/cm = 9.84 x 10⁴.

77

Figure 45: Heat-Transfer Distributions along the Windward Streamline of the Shuttle Orbiter at AEDC Tunnel B Conditions with α = 30-deg and Re/cm ranging from 1.64 x 10⁴ to 9.8 x 10⁴.

78

Figure 45: Continued.
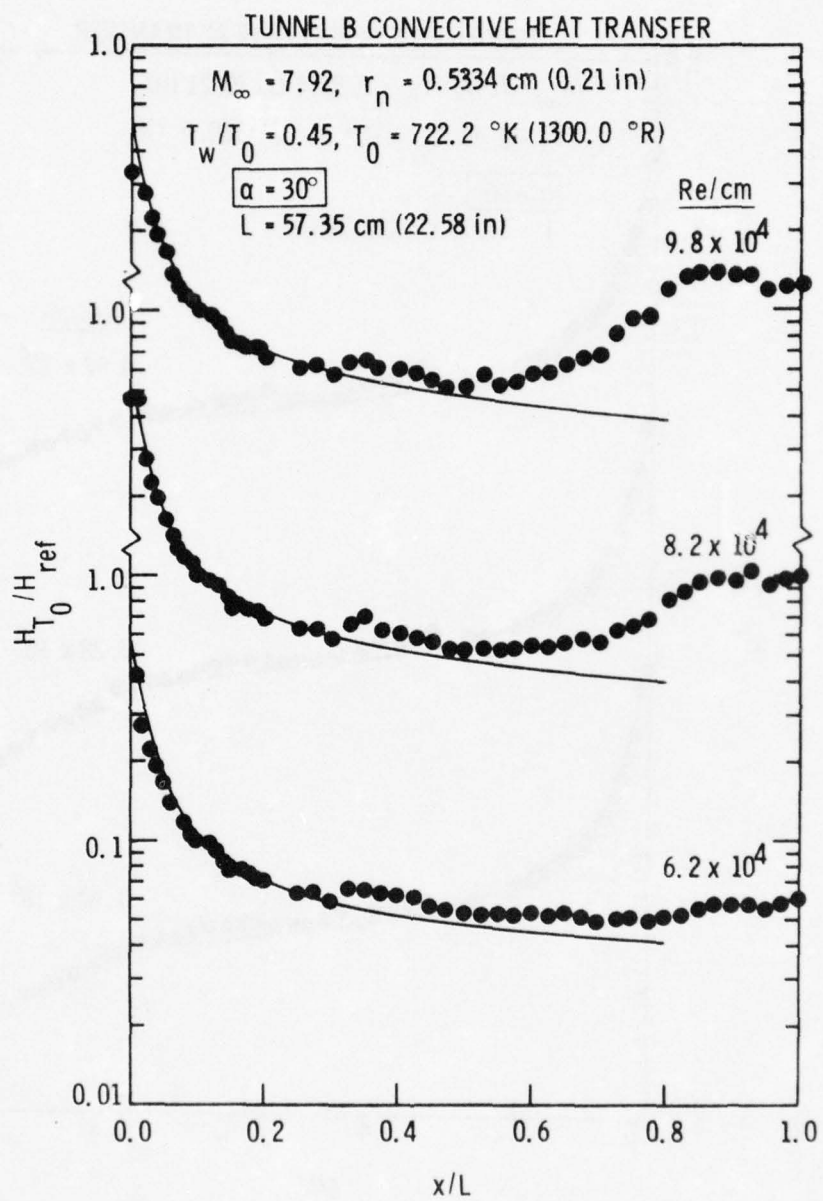
79

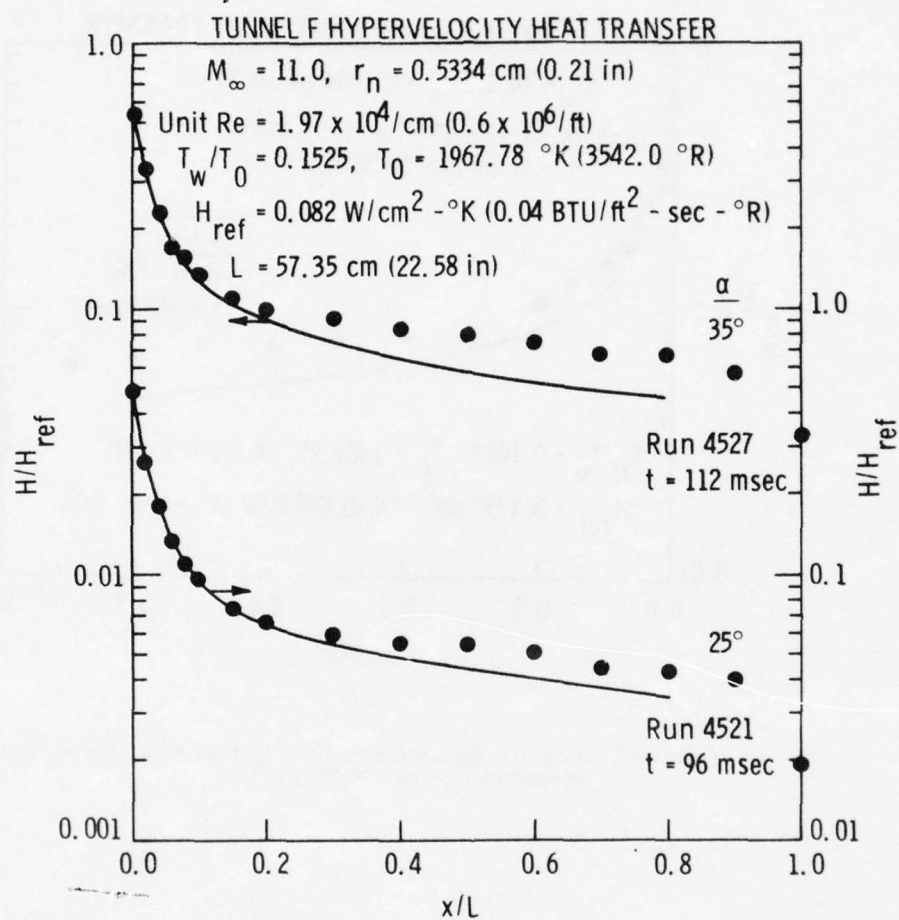TUNNEL F HYPERVELOCITY HEAT TRANSFER

$M_\infty = 11.0$, $r_n = 0.5334$ cm (0.21 in)
Unit Re = 1.97×10^4/cm (0.6×10^6/ft)
$T_w/T_0 = 0.1525$, $T_0 = 1967.78$ °K (3542.0 °R)
$H_{ref} = 0.082$ W/cm^2-°K (0.04 BTU/ft^2-sec-°R)
L = 57.35 cm (22.58 in)

$\dfrac{\alpha}{35°}$

Run 4527
t = 112 msec

25°

Run 4521
t = 96 msec

Figure 46: Tunnel F Heat-Transfer Distributions along the Windward
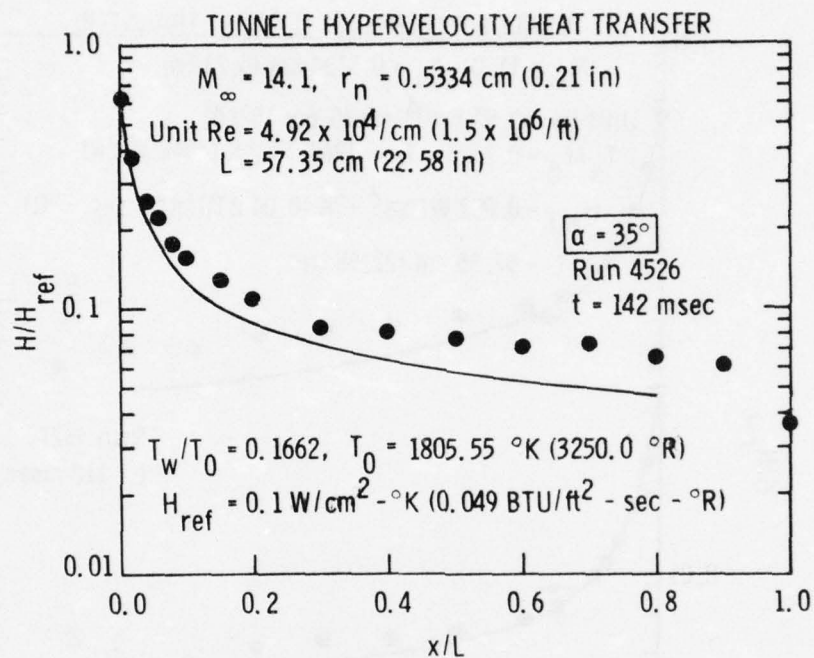Streamline of the Shuttle Orbiter at Re/cm = 1.97×10^4.

80

Figure 47: Tunnel F Heat-Transfer Distribution along the Windward Streamline, Re/cm = 4.92 x 10⁴.

81

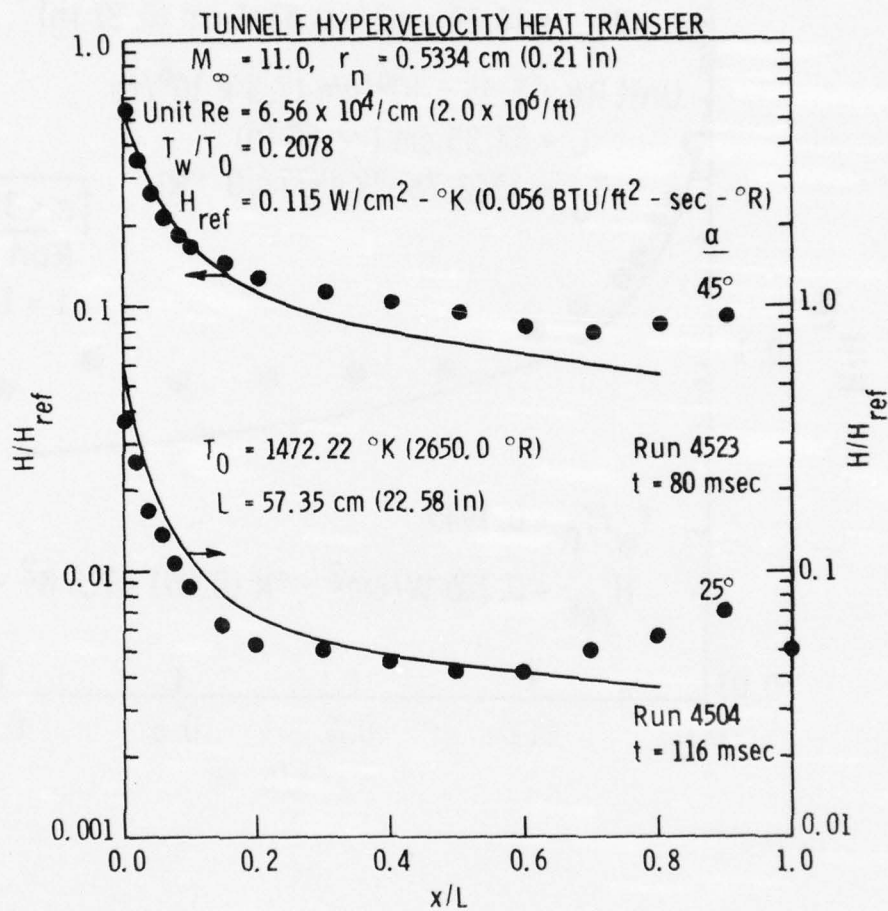TUNNEL F HYPERVELOCITY HEAT TRANSFER

$M_\infty = 11.0$, $r_n = 0.5334$ cm (0.21 in)

Unit Re = 6.56×10^4/cm (2.0×10^6/ft)

$T_w/T_0 = 0.2078$

$H_{ref} = 0.115$ W/cm^2 - °K (0.056 BTU/ft^2 - sec - °R)

α

45°

$T_0 = 1472.22$ °K (2650.0 °R)   Run 4523

$L = 57.35$ cm (22.58 in)   t = 80 msec

25°

Run 4504

t = 116 msec

x/L

Figure 48: Tunnel F Heat-Transfer Distributions along the Windward
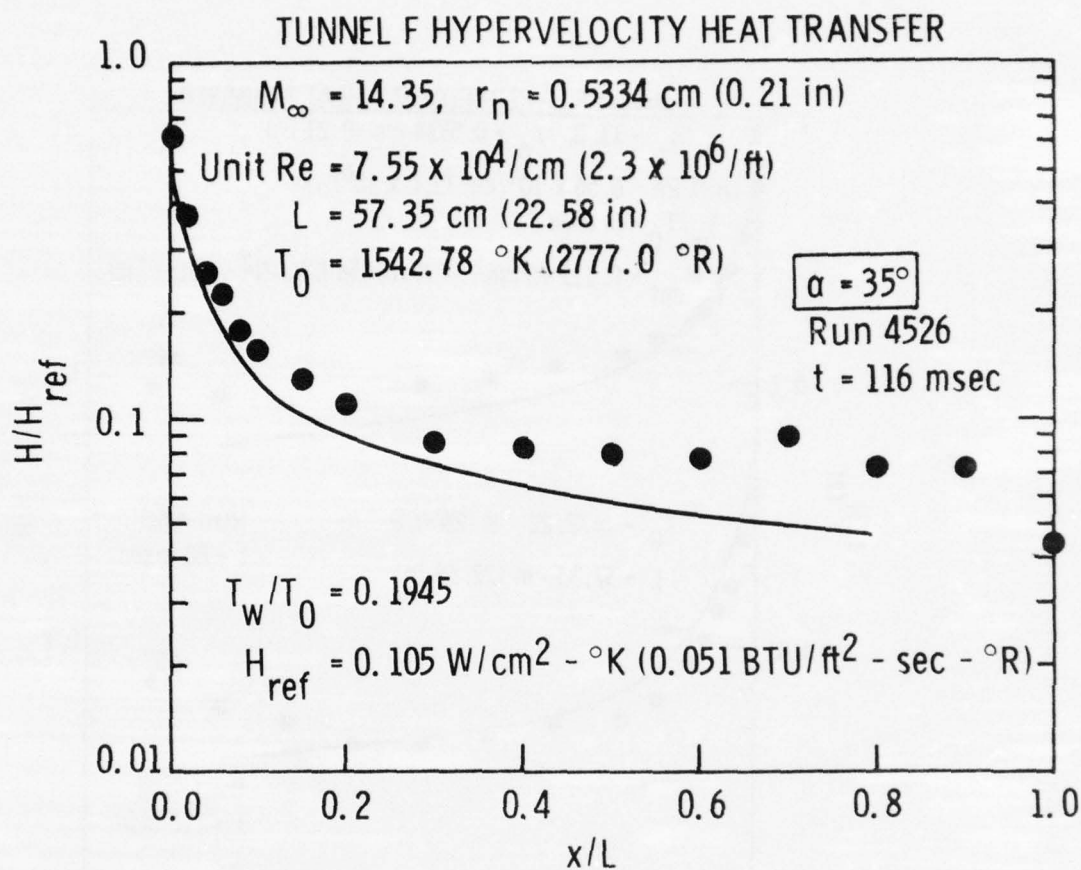Streamline, Re/cm = 6.56×10^4.

82

Figure 49: Tunnel F Heat-Transfer Distribution along the Windward Streamline, Re/cm = 7.55 x 10⁴.
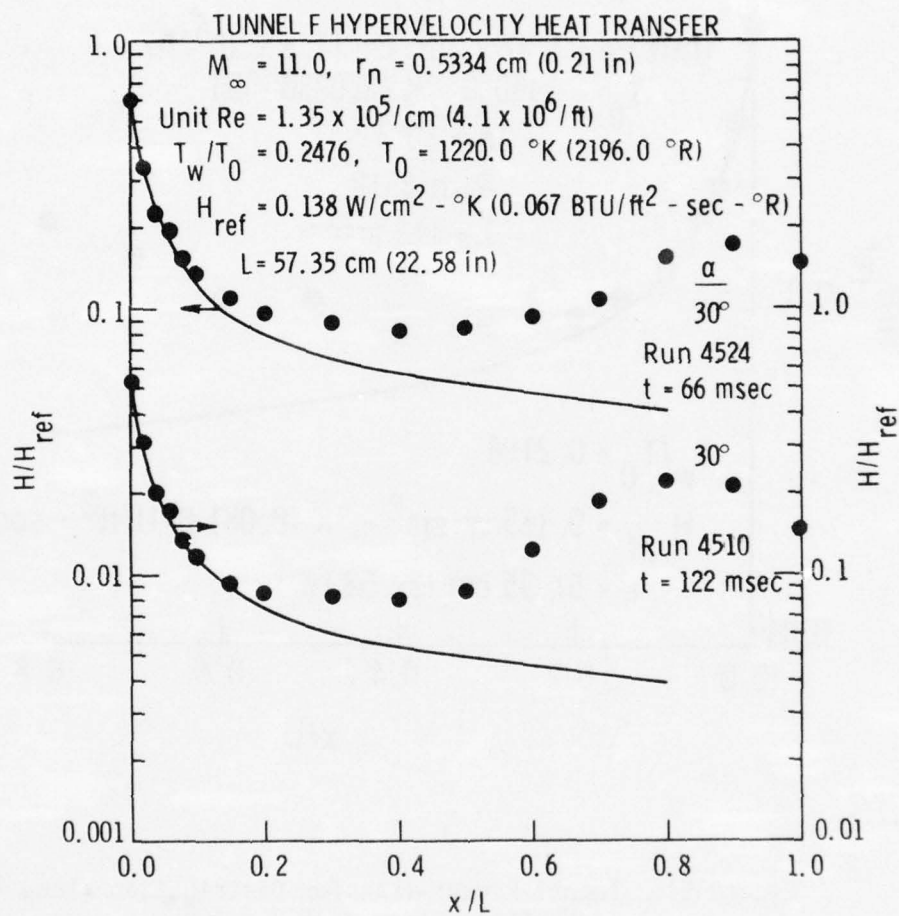
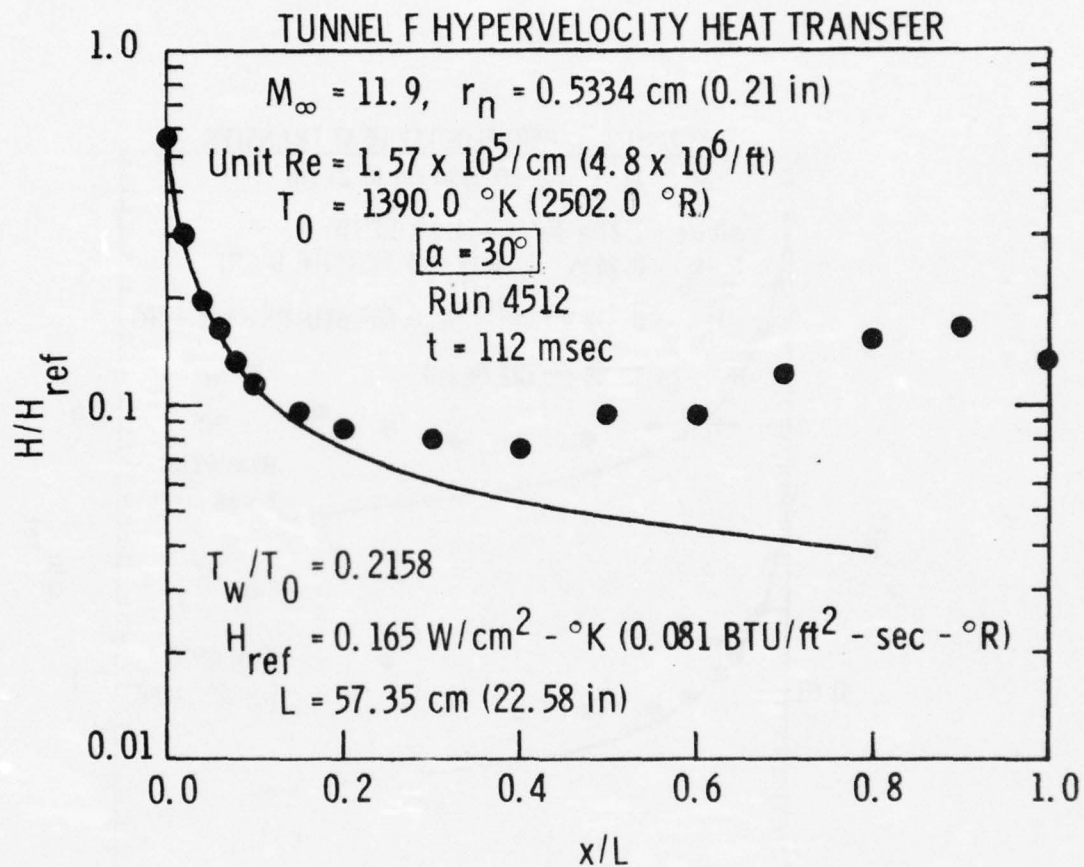Figure 50: Tunnel F Heat-Transfer Distributions along the Windward Streamline, Re/cm = 13.5×10^4.

84

Figure 51:   Tunnel F Heat-Transfer Distribution along the Windward Streamline, Re/cm = 15.7 x 10⁴.